

HU ISSN 1586–2070

JOURNAL OF COMPUTATIONAL AND APPLIED MECHANICS

A Publication of the University of Miskolc

VOLUME 8, NUMBER 2 (2007)



MISKOLC UNIVERSITY PRESS

HU ISSN 1586–2070

JOURNAL OF COMPUTATIONAL AND APPLIED MECHANICS

A Publication of the University of Miskolc

VOLUME 8, NUMBER 2 (2007)



MISKOLC UNIVERSITY PRESS

EDITORIAL BOARD

- István PÁCZELT, Editor in Chief, Department of Mechanics, University of Miskolc, 3515 MISKOLC, Hungary, mechpacz@uni-miskolc.hu
- László BARANYI, Department of Fluid and Heat Engineering, University of Miskolc, 3515 MISKOLC, Hungary, aramb1@uni-miskolc.hu
- Edgár BERTÓTI, Department of Mechanics, University of Miskolc, 3515 MISKOLC, Hungary, mechber@uni-miskolc.hu
- Tibor CZIBERE, Department of Fluid and Heat Engineering, University of Miskolc, 3515 MISKOLC, Hungary, aramct@uni-miskolc.hu
- István ECSEDI, Department of Mechanics, University of Miskolc, 3515 MISKOLC, Hungary, mechecs@uni-miskolc.hu
- Wolfram FRANK, Institut für Fluid- und Thermodynamik, Universität Siegen, Paul-Bonatz-Strasse 9-11, 57076 SIEGEN, Germany, frank@ift.mb.uni-siegen.de
- Ulrich GABBERT, Institut für Mechanik, Otto-von-Guericke-Universität Magdeburg, Universitätsplatz 2, 39106 MAGDEBURG, Germany, ulrich.gabbert@mb.uni-magdeburg.de
- Zolt GÁSPÁR, Department of Structural Mechanics, Budapest University of Technology and Economics, Műegyetem rkp. 3, 1111 BUDAPEST, Hungary, gaspar@ep-mech.me.bme.hu
- Robert HABER, Department of Theoretical and Applied Mechanics, University of Illinois at Urbana-Champaign, 216 Talbot Lab., 104 S. Wright Str., URBANA, IL 61801, USA, r-haber@uiuc.edu
- Gábor HALÁSZ, Department of Hydraulic Machines, Budapest University of Technology and Economics, Műegyetem rkp. 3, 1111 BUDAPEST, Hungary, HALASZ@vizgep.bme.hu
- Ji Huan HE, Department of Mathematics, College of Basic Science, Shanghai Donghua University, No. 1882 Yan'anxilu Road, 200051 SHANGHAI, China, jhhe@dhu.edu.cn
- Károly JÁRMAI, Department of Materials Handling and Logistics, University of Miskolc, 3515 MISKOLC, Hungary, altjar@gold.uni-miskolc.hu
- László KOLLÁR, Department of Strength of Materials and Structures, Budapest University of Technology and Economics, Műegyetem rkpt. 1-3. K.II.42., 1521 BUDAPEST, Hungary, lkollar@goliat.eik.bme.hu
- Vladimir KOMPIŠ, Department of Mechanics, University of Žilina, ŽILINA, Slovakia, Vladimir_Kompis@kmpp.utc.sk
- Imre KOZÁK, Department of Mechanics, University of Miskolc, 3515 MISKOLC, Hungary, mechkoz@uni-miskolc.hu
- József KÖVECSÉS, Department of Mechanical Engineering, McGill University, 817 Sherbrooke Street West, MD163, Montreal, Quebec H3A 2K6, jozsef.kovecses@mcgill.ca
- Márta KURUTZ, Department of Structural Mechanics, Budapest University of Technology and Economics, Műegyetem rkp. 3, 1111 BUDAPEST, Hungary, kurutzm@eik.bme.hu
- R. Ivan LEWIS, Room 2-16 Bruce Building, Newcastle University, NEWCASTLE UPON TYNE, NE1 7RU, UK, R.I.Lewis@NCL.AC.UK
- Gennadij LVOV, Department of Mechanics, Kharkov Polytechnical Institute, 2 Frunze Str., 310002 KHARKOV, Ukraine, lvovgi@kpi.kharkov.ua
- Herbert MANG, Institute for Strength of Materials, University of Technology, Karlsplatz 13, 1040 VIENNA, Austria, Herbert.Mang@tuwien.ac.at
- Zenon MROZ, Polish Academy of Sciences, Institute of Fundamental Technological Research, Swietokrzyska 21, WARSAW, Poland, zmroz@ippt.gov.pl
- Tibor NAGY, Department of Physics, University of Miskolc, 3515 MISKOLC, Hungary, fiznagyt@uni-miskolc.hu
- Gyula PATKÓ, Department of Machine Tools, University of Miskolc, 3515 MISKOLC, Hungary, mechpgy@uni-miskolc.hu
- Jan SLADEK, Ústav stavbenictva a architektúry, Slovenskej akadémie vied, Dubróvska cesta 9, 842 20 BRATISLAVA, Slovakia, usarslad@savba.sk
- Gábor STÉPÁN, Department of Mechanics, Budapest University of Technology and Economics, Műegyetem rkp. 3, 1111 BUDAPEST, Hungary, stepan@mm.bme.hu
- Barna SZABÓ, Center for Computational Mechanics, Washington University, Campus Box 1129, St. LOUIS, MO63130, USA, szabo@ccm.wustl.edu
- Szilárd SZABÓ, Department of Fluid and Heat Engineering, University of Miskolc, 3515 MISKOLC, Hungary, aram2xsz@uni-miskolc.hu
- György SZEIDL, Department of Mechanics, University of Miskolc, 3515 MISKOLC, Hungary, Gyorgy.SZEIDL@uni-miskolc.hu

LOCAL EDITORIAL COUNCIL

T. CZIBERE, I. KOZÁK, I. PÁCZELT, G. PATKÓ, G. SZEIDL

APPLICATION OF A CROSS FLOW FAN AS WIND TURBINE

TONI KLEMM, MARTIN GABI, JEAN-NICOLAS HERAUD
Department of Fluid-Machinery, University Karlsruhe
76128 Karlsruhe, Germany
toni.klemm@ism.uka.de

[Received: January 3, 2007]

Abstract. Investigations of the flow structure in a cross flow wind turbine are presented. To determine the flow field, CFD simulations and PIV measurements were carried out. These results are the starting point to develop efficient casings for cross flow wind turbines.

Keywords: cross flow fan, wind turbine, wind power, *CFD*, *PIV*

Nomenclature

c	[m/s]	absolute velocity
D	[m]	diameter
L	[m]	length
M	[Nm]	torque
n	[rpm]	rotational speed
p	[Pa]	number of time steps
Q	[m^3/s]	volume flow rate
\mathcal{R}	[-]	degree of reaktion
S	[m]	chord length
t	[s]	time
u	[m/s]	circumferential velocity
w	[m/s]	relative velocity
x	[η]	efficiency

Subscripts and superscripts

n	normalized
u	peripheral direction
st	static
tot	total
1	inner diameter
2	outer diameter

1. Introduction

Cross Flow Turbines are widely used in small hydroelectric power plants. The design of these turbines is based on Banki-type turbine (Figure 1). The turbine is partial loaded to avoid churning losses. The water supply is realized at the top of impeller with a control device. The water jet leaves the blade channels at the inner rotor diameter and after crossing the space inside the second blade row, it passes to outside direction. The rotational speed is limited as the jet should not touch the shaft of the rotor. Advantages of this type are the smaller size and costs, as well as the performance at operating conditions with low head, compared to turbinetypes like Francis and Kaplan-types. This is a result of the high power density. To apply these favourable properties on a wind turbine, investigations have to be carried out. This is

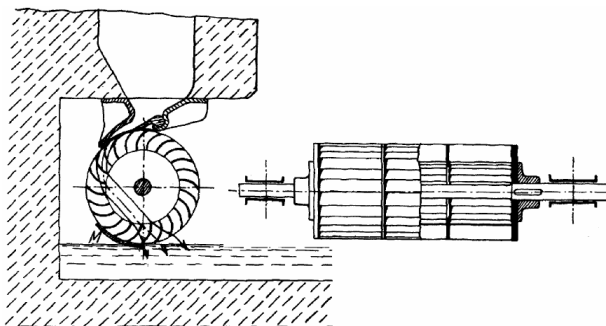


Figure 1. Banki-type turbine [1]

necessary, as the modification of the fluid results in different flow conditions. In the water turbine blades, are partially loaded with energy transforming fluid in contrast to the wind turbine. This leads to a highly complex flow structure inside and outside of the rotor and in the blade channels with inducing flow losses.

Cross flow wind turbines can be established to use wide but flat fluid flows. These flows occur for instance at mountain sides and valleys, due to thermic effects. Applications span furthermore the use of buoyancy flows at warmed facades on buildings and flows in tunnel systems. The capacity taken from the mechanical energy of the wind can be used for example in combination with a photovoltaic solar power plant to charge an accumulator at days with poor light and at night. Considerations about reasonable applications in economical and energetic point of view are not accomplished yet.

2. Objectives of investigations

Due to the similarities of flow inside a cross flow fan and a Banki-type turbine, casing and rotor design of a typical cross flow fan are used. The data of rotor and casing are shown in Figure 2 and Table 1.

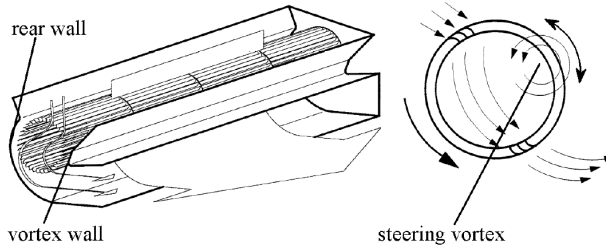


Figure 3. Funktionalität of a cross flow fan

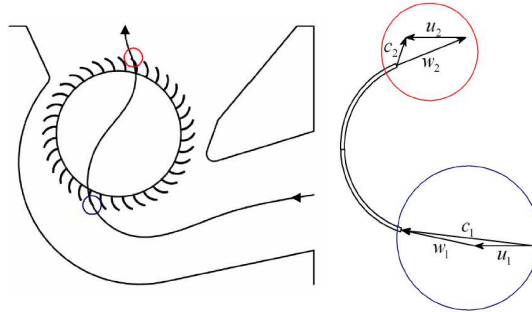


Figure 4. Principle of a cross flow turbine

inside the rotor, near the so called vortex wall. This causes a transient flow in the blade channels and a relative low efficiency rate of about $\eta_{max} = 0.5$. To realize a wind turbine, the flow direction is inverted (Figure 4). In a wind turbine the static pressure between inlet and outlet is equal. That means, that a wind turbine is of the type action turbine. With consideration of a cross flow fan, it can be seen, that the degree of reaction is about zero (equation 2.2). Therefore an inversely passed cross flow fan is adequate to use as wind turbine.

$$\mathcal{R} = \frac{\Delta p_{st}}{\Delta p_{tot}} \quad (2.2)$$

The turbine is investigated at operating conditions, when the torque, delivered to the shaft, is zero ($M = 0 \text{ Nm}$).

To visualize the flow, numerical and experimental investigations are carried out. The numerical calculations are necessary for the visualization of the flow inside the rotor. To validate the flow in the casing, *PIV*-measurements were carried out.

3. Experimental and numerical setup

The experimental test rig is a suction side cross flow fan test section with applied *PIV*-metrology (Figure 5). In contrast to the cross flow fan the mounting position

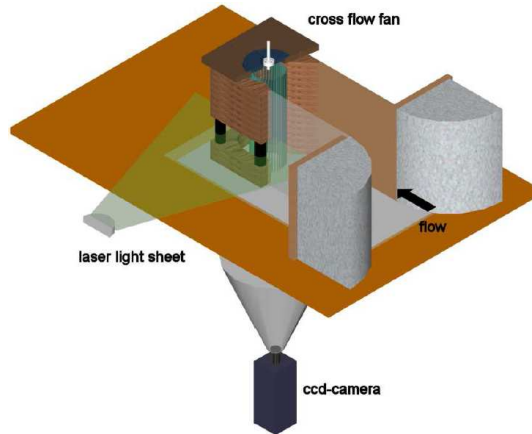


Figure 5. *PIV*-measurement test section for cross flow fans

of the wind turbine is rotated by 90° . To apply laser metrology, it is necessary to ensure optical access inside the casing. For this reason the rear wall is formed in a small area with thin acrylic glass. The optical access in the outlet channel is also realized by acrylic glass. The nozzle at the inlet area should guarantee an inflow into the turbine, which is free of separation. The auxiliary fan of the test rig is used to generate the flow. Zero-torque condition at the shaft is realized by an electric motor, which offsets friction losses of the bearing. Therefore a torque measurement axle is integrated in the power train. The rotating speed of the rotor is $n = 1000 \text{ rpm}$. The *PIV*-measurements are accomplished in plane to the mean flow direction (Figure 5). For performance data logging of the fan, a computer aided measurement system is used. The applied *PIV*-system consists of 2 ND-YAG lasers, a digital CCD-camera, a synchronizer to synchronize laser and camera and a PC to gather and evaluate the measurement data. To measure the velocity of the flow, very small particles in the flow are necessary. The seeding particles are generated by vaporizing olive oil and are supplied into the inlet of the test rig.

For the prediction of the flow through the cross flow turbine, the commercial CFD package STAR-CD is used. The advantage of this package is the combination of flow solver, pre- and post processing. The numerical computation is reduced to a 2-dimensional, incompressible description of the flow field to reduce calculation time. This restriction is possible as the flow in a cross flow turbine is nearly 2-dimensional. For discretization and approximation of the velocity components, the MARS-scheme is used [3]. The calculation is unsteady, because of the highly transient flow in the blade channels. The time discretization is implicit with a time step of $\Delta t = 10^{-4} \text{ s}$. The pressure correction is realized with the PISO-algorithm.

Figure 6 shows the computational domain and the boundary conditions. The computational domain is divided into four subdomains: The inflow area, the casing of the cross flow turbine, the outlet area and the moving blade area. The connection

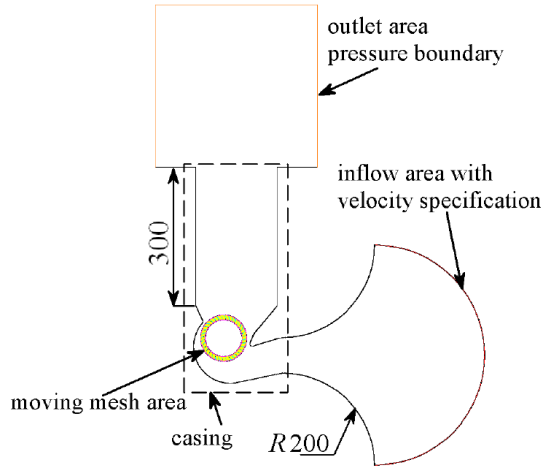


Figure 6. Computational domain and boundary conditions

between the rotating and static mesh is realized with an "arbitrary sliding interface method" (ASI), which is implemented in STAR-CD. At the walls, including the blade surfaces, turbulent flow wall boundary conditions are implemented, using a cubic low-Re $k - \epsilon$ turbulence model. As inlet condition, a constant velocity field is assumed. The volume flow rate follows from a variation of the inlet velocity, in that way that the torque at the blades is equal to zero. At the outlet a constant static pressure is presumed. The numerical grid has about 100,000 nodes. The numerical discretization is validated by the number of nodes [4].

4. Results and discussion

Due to the type of investigation, the most important criterion for evaluating the simulation results, is the required volume flow rate to rotate the rotor with a rotational speed of $n = 1000 \text{ rpm}$ and $M = 0 \text{ Nm}$. Table 2 shows the different volume flow rates for the experiment and the simulation. There is a big difference between the calculated

Table 2. Comparison of the volume flow rates

		simulation	experiment
Q	$\frac{\text{m}^3}{\text{s}}$	0.1	0.18

and the measured volume flow rate. To analyse these differences, flow patterns of the numerical results and the PIV-measurements are compared. For comparing the flow patterns with the same contour legend, the absolute velocity is normalized with respect to the mean flow velocity in the blade channels (equation 4.1). The mean flow

velocity is estimated with the cross section of the rotor diameter.

$$c_n = \frac{cLD}{Q} \quad (4.1)$$

Due to the design of the casing and the rotor, optical access in all areas could not be realized. These areas are blanked. The depiction of the velocity distribution inside the turbine shows unfavourable flow behaviour (Figure 7). This mainly results from gap losses between rotor and casing. Another problem is the large vortex inside the rotor, which reduces the energy transfer from the flow to mechanical power due to obstruction of the blade channels. On that reason two zones with high velocity

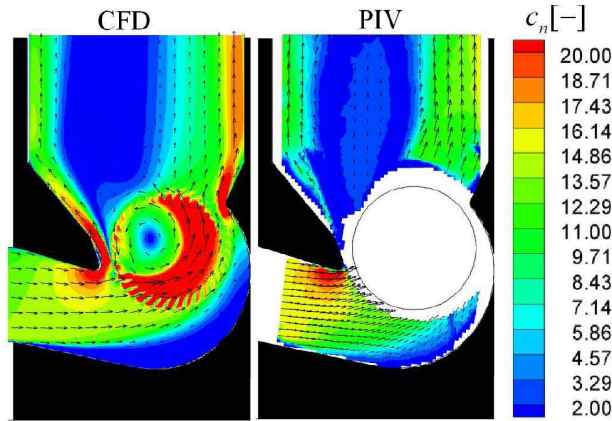


Figure 7. Comparison of numerical and experimental flow pattern

components and a back flow in the middle of the outlet channel are generated. The back flow in the experiment is more developed. This requires a higher amount of energy to rotate the impeller which results in a higher volume flow rate. Due to enlarged velocity components, friction losses rise as well as the required energy. That is the main reason of the differences between the volume flow rates of the numerical calculation and the experimental measurements. Another difference between the simulation and the experiment occurs at the bottom side in the inflow channel. The separation in the simulation obviously begins earlier than in the experiment. This is an influence due to the 2-d assumption of the flow. The turbulent quantities thereby are much lower than under experimental conditions, where the radial limitation of the side walls of the channel produce more turbulence.

The investigation shows the capability of the numerical method to simulate the flow field in a cross flow turbine qualitatively. Thereby it is possible to start a numerical optimization process to design a suitable casing of a cross flow turbine. The casing has to be characterized by an optimal energy transfer from the fluid to mechanical power. To accomplish this, gap flow and vortex size have to be reduced. Figure 8 shows a possible arrangement of the casing components around the impeller. If a practicable application is possible further investigations have to be carried out.

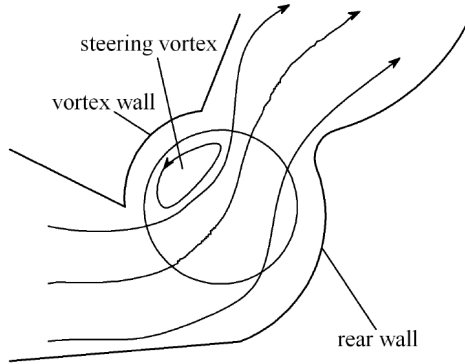


Figure 8. Concept of a cross flow wind turbine with possible improved energy transfer

5. Optimization

To realize this concept further numerical investigations are carried out. The geometry and the numerical model of an improved cross flow turbine are shown in Figure 9.

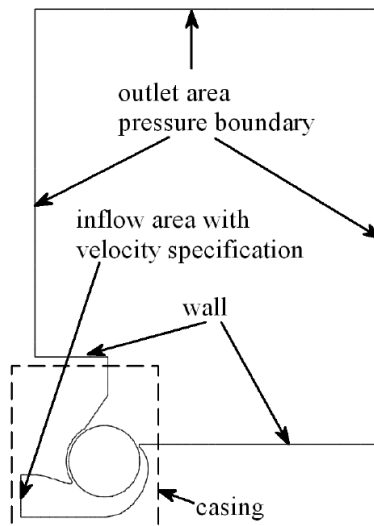


Figure 9. New geometry (numerical model)

The calculation result shows a significant improvement in the volume flow rate, required to rotate the impeller with $n = 1000 \text{ rpm}$ (Table 3).

The volume flow rate is reduced almost by half of the value of the cross flow turbine with the casing of a cross flow fan. This is mainly the result of the new vortex wall

Table 3. Volume flow rate of the new geometry (simulation data)

		new geometry
Q	$\frac{m^3}{s}$	0.056

design. Due to the long, small gap at the vortex wall, the flow structure inside the gap is very complex (Figure 10).

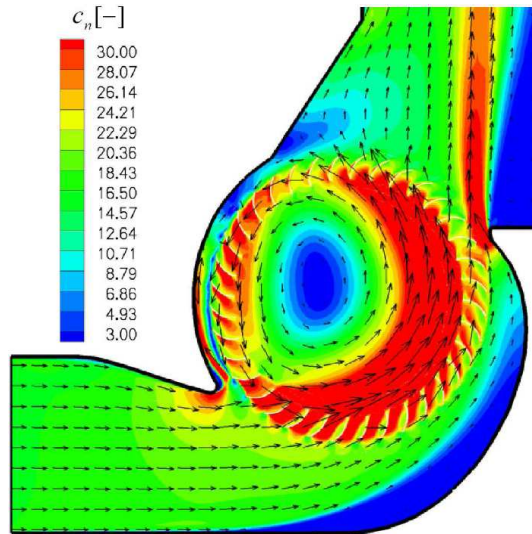


Figure 10. New geometry (numerical model)

It is a combination of gap flow in mean flow direction and backflow against the mean flow direction. This leads to a high flow resistance with the effect of a reduced gap flow. The energy of the flow dissipates inside the gap. Furthermore, due to the large vortex wall, the back flow in the outlet channel could be avoided. But the flow structure shows, that further improvements seem possible. The new casing design couldn't reduce the steering vortex significantly. Another point is the high gap flow at the rear wall. For improvements of the energy transfer from the fluid to mechanical power, the flow inside the blade channels has to be considered. For a high efficiency of the wind turbine, a blade-congruent and a uniform distribution of the energy transfer along the circumference of the rotor are necessary. But due to the working principle, this could not completely be realized. Especially along the vortex wall, a transfer of the energy of the fluid to mechanical power is impossible, because the flow in the blade channels is completely in circumferential direction. In Figure 11 and 12 a satisfactory energy transfer can be seen only in a small part of the second blade row. Figure 11 shows the distribution of circumferential value of the absolute velocity. According to equation 2.1, only in the second blade row, significant changes of c_u can be seen. This

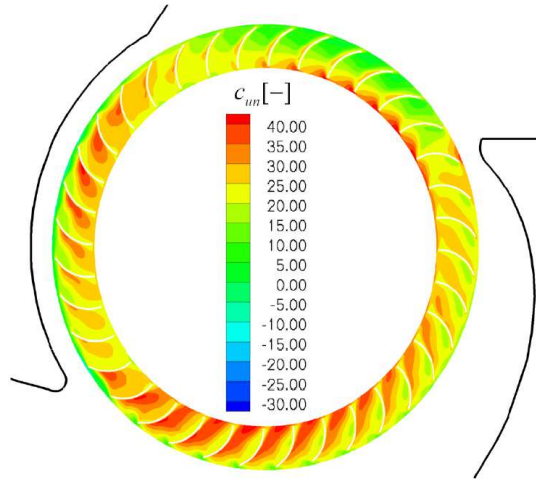


Figure 11. New geometry: distribution of normalized, circumferential component of the absolute velocity c_{un}

also concerns the pressure distribution in the blade channels (Figure 12). Only in the

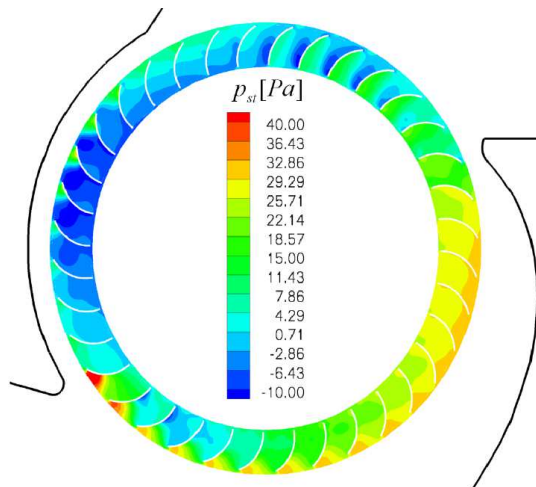


Figure 12. New geometry: distribution of static pressure p_{st} inside the blade channels

second blade row a developed pressure and suction side of the blades is recognizable. At the first blade row pressure peaks at the first part of the blade could be seen. This results due to the drive of the impeller, to realize a torque of $M = 0 \text{ Nm}$ at the shaft. The resulting resistance against the rotating direction of the impeller should be avoided. To raise efficiency and energy transfer, the flow in the blade channels

has to be improved. Especially at the first blade row the flow is highly separated and swirled (Figure 13). That means for the further process in developing casings for

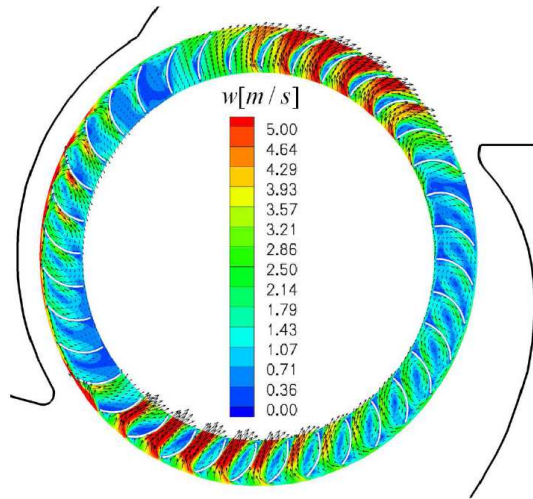


Figure 13. New geometry: distribution of relative velocity w

cross flow turbines, that guided vanes in front of the first blade row have to be taken into account.

6. Conclusion

The accomplished investigations show the potential of an application of a cross flow fan as wind turbine. However, the flow structure and the performance are not satisfactory. On that reason an optimization process of the casing was started. The presented new geometry of the casing shows a significant improvement of the performance. Potential for further improvements of the casing can be derived from the analysis of the flow structure. To ensure the quality in the numerical developing process, CFD results have to be verified with further experimental measurements.

References

1. SONNECK, E.: Durchströmturbine, Springer Verlag, Germany, (1923).
2. TANINO, T., NAKAO, S. AND UEBAYASHI, G.: Improving Ambient Wind Enviof a Cross Flow Wind Turbine near a Structure by Using an Inlet Guide Structure and a Flow Deflector, Proceed. of the 7th Intern. Symp. on Exp. and Comp. Aerodynamics of Internal Flows, Tokyo, (2005), 225-230.
3. CD ADAPCO GROUP.: Methodology, London, England, (2004).
4. KLEMM, T.: Numerische und experimentelle Untersuchungen an Ventilatoren hoher Leistungsdichte, Dissertation, University Karlsruhe (TH), Germany, (2005).

INFLUENCE OF A CRUCIFORM ARRANGEMENT DOWNSTREAM STRIP-PLATE ON CROSSFLOW VIBRATION OF A SQUARE CYLINDER

MIZUYASU KOIDE, NAOTO KATO, SHUICHI YAMADA, YUSUKE KAWABATA,
TSUTOMU TAKAHASHI, MASATAKA SHIRAKASHI
Live Engineering Research Center, Niigata Sangyo University
4730 Karuigawa, Kashiwazaki, 945-1393, Japan
mkoid@ind.nsu.ac.jp

[Received: January 15, 2007]

Abstract. In earlier works, the present authors found that the Kármán vortex excitation of a circular cylinder is effectively suppressed by setting another cylinder in cruciform arrangement downstream with a gap-to-diameter ratio s/d less than 0.5, and that new vortex excitations are induced by two types of longitudinal vortices shedding periodically near the cross in higher velocity ranges. In this work, influence of a strip-plate set downstream in cruciform arrangement on the vibration of a square cylinder is investigated by wind tunnel experiment. The Kármán vortex excitation is well suppressed by the strip-plate with a width w equal to the side of square d when $s/d < 2$. The galloping is also completely suppressed by the plate when $s/d < 4$, except the range of $1 < s/d < 2$. In the latter range of s/d , a new vibration occurs and its maximum amplitude at s/d around 1.3 is double the original galloping. Flow visualization by tuft grid and velocity measurement show that this vibration is caused by the longitudinal vortex shedding periodically near the cross which synchronizes with the cylinder motion, similar to the case of a two-circular-cylinder system.

Keywords: flow induced vibration, galloping, longitudinal vortex, vibration control, vortex excitation

Nomenclature

d	side-length of square cylinder = 26 mm
f_n	system natural frequency
f_v	vortex shedding frequency
f_{v0}	vortex shedding frequency for fixed systems
f_z	vibration frequency
Re	Reynolds number ($= Ud/\nu$)
s	gap between bodies
St	Strouhal number ($= f_v d/U$)
St_0	Strouhal number for fixed systems ($= f_{v0} d/U$)
S_u	spectrum of velocity u
U	free stream velocity

u	velocity component in the x -direction
w	width of downstream strip-plate
Z	z -displacement of upstream cylinder
Z_{rms}	root-mean-square value of Z
Z_{rms}^*	Z_{rms} normalized by Z_{rms} of single cylinder
δ	logarithmic damping factor
ν	kinematic viscosity of fluid

1. Introduction

Since vibrations of cylindrical bodies in fluid flow have caused many serious accidents in mechanical and structure engineering, various methods for controlling of flow-induced vibration of a cylindrical body have been proposed so far, such as suction holes on the surface of the body, tripping wires near separation points, a splitter plate in the wake, and so on [1]. The innumerable number of such techniques shows the practical importance of the phenomenon.

Tomita et al. [2] reported that the acoustic noise from a circular cylinder can be suppressed by setting another cylinder downstream in cruciform arrangement with a certain gap between them as shown in Figure 1. Inspired by Tomita's work, the present authors investigated effect of the downstream cylinder on the Kármán vortex excitation of the upstream cylinder, and found that the vibration is effectively suppressed when the gap-to-diameter ratio s/d is less than around 0.5. However, it was also found that two types of longitudinal vortices, i.e. trailing vortex (Figure 1(a)) or necklace vortex (Figure 1(b)), shed periodically depending on the gap-to-diameter ratio and that these longitudinal vortices induce resonant excitation similar to the Kármán vortex excitation over respective velocity regions, several times higher than that of the latter [3, 4].

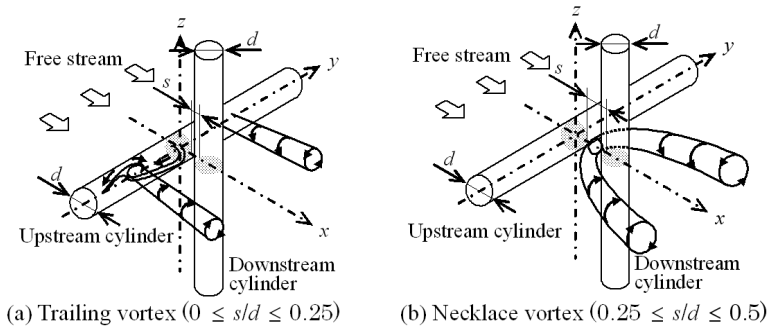


Figure 1. Longitudinal vortices from a cruciform two circular cylinder system

In the case of a square cylinder, it is well known that another crossflow vibration called a "galloping" occurs at velocities higher than the Kármán vortex excitation caused by flow-elastic instability [1].

Recently, the present authors found that a cruciform arrangement downstream strip-plate with a width w equal to the side of the square d can suppress both the Kármán vortex excitation and the galloping, and induce a longitudinal vortex excitation [5]. The specific aim of this work is to investigate the effects of a cruciform downstream strip-plate on the crossflow vibration behaviour of a square cylinder in detail by using strip-plates with variable width in wind tunnel experiment.

2. Experimental apparatus and measurement

Arrangement of the experimental apparatus and the coordinate system used in this paper are shown in Figure 2. A blow down type wind tunnel with a test section of 0.32 m square cross-section (the upper and lower walls of the test section are not drawn in Figure 2) and a 1 m length is used. The turbulence level at the center of the test section is less than 0.6 % at $U = 2$ m/s.

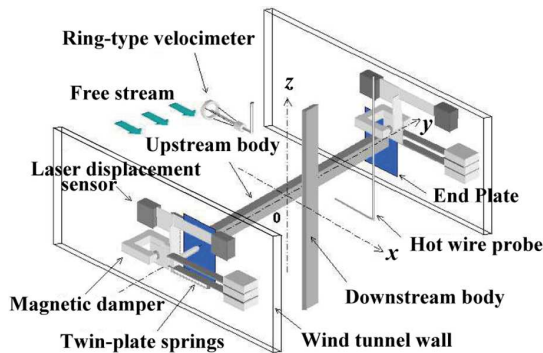


Figure 2. Arrangement of the experimental apparatus and the coordinate system

A rigid rod passes through slots on the side walls of the measuring section and is fixed rigidly or supported elastically at both ends outside the measuring section. In the latter setup, two twin-plate-springs are used as shown in Figure 2 so as to make its motion pure crossflow mode [6]. A square cross section cylinder with side-length $d = 26$ mm and spanwise length $l_e = 318$ mm is fixed to the rod. End plates are attached to the cylinder to remove influence of flow through the slots [7].

A strip-plate is mounted rigidly on a traversing table set beneath the measuring section, which enables to adjust the gap s within a preciseness of 0.05 mm. The downstream strip-plate is spanned over the whole height of the measuring section. The width of the downstream strip-plate w is varied from 10 mm to 26 mm, while its thickness is fixed at 5 mm. Preliminary experiments have shown that the influence of the plate thickness is insignificant.

The natural frequency f_n and logarithmic damping factor δ are obtained by free damping oscillation in air otherwise at rest. The effective mass m_e is calculated

from f_n thus determined and the spring constant k measured separately. The free flow velocity U is measured by the ring-type velocimeter [8]. The vortex shedding frequency f_v is determined from a spectrum S_u of x -component velocity u , measured by using a hot-wire probe placed at an appropriate location to detect the periodic shedding of vortices.

The vertical displacement of the square cylinder, Z , is defined as the average of values measured by laser displacement sensors at the both ends of the supporting rod outside the measuring section (Figure 2). The tuft grid method is applied to observe the cross section of the longitudinal vortex in the wind tunnel.

3. Kármán vortex excitation and galloping of an isolated square cylinder

Vibration of the isolated square cylinder (i.e. without downstream strip-plate) and the vortex shedding frequency were measured with an increasing and then decreasing flow velocity.

Variation of spectra of velocity and displacement for the former case is shown in Figure 3.

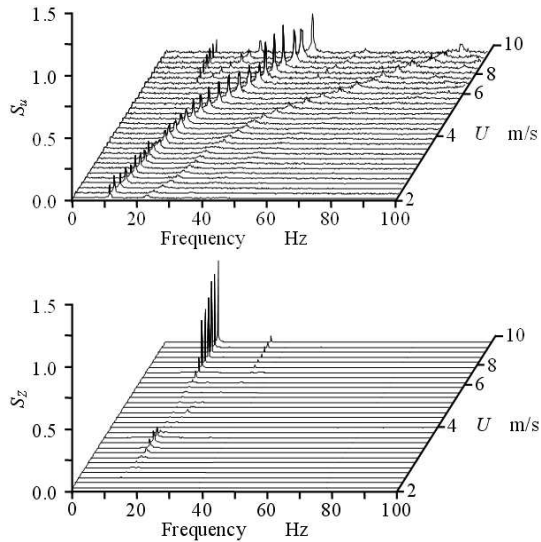


Figure 3. Variation of spectra of velocity and displacement with increasing U for isolated square cylinder ($f_n = 16.41 \text{ Hz}$, $\delta = 0.038$. Hot-wire probe position: $x/d = 1.5$, $y/d = 0$, $z/d = 0.4$)

As seen in this figure, the cylinder oscillates essentially at its natural frequency irrespective of flow velocity U over all the range of measurement. While, the velocity spectra have a sharp peak at a frequency almost proportional with U , showing the periodic Kármán vortex shedding.

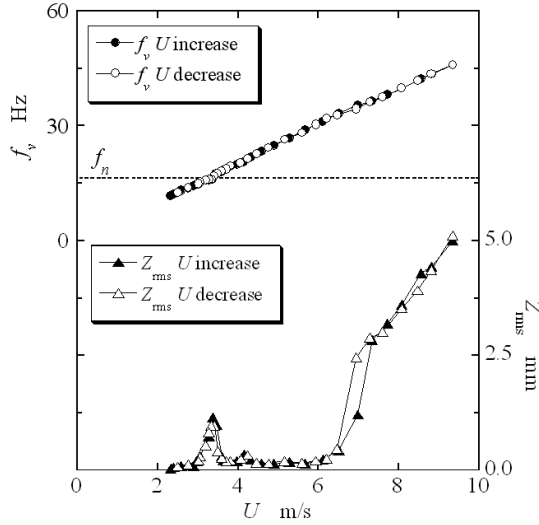


Figure 4. Vibration behaviour of an isolated square cylinder ($f_n = 16.41$ Hz, $\delta = 0.038$. Hot-wire probe position: $x/d = 1.5$, $y/d = 0$, $z/d = 0.4$)

In Figure 4, the oscillation amplitude expressed by the RMS value of z -displacement, Z_{rms} , and the vortex shedding frequency f_v , which is the dominant frequency of the spectrum in Figure 3, are plotted against the flow velocity U . As well known for the case of a single square cylinder, the Kármán vortex excitation and the galloping are clearly observed in separated velocity regions in the figure. The former is observed over a certain range of U around 3.4 m/s as seen in Figure 3, where the spectra of displacement Z and velocity u have a sharp peak at the frequency f_n , showing occurrence of the lock-in phenomenon. While, the latter vibration increases with velocity and f_v is much higher than f_n . It should be noted here that the vibration frequency f_z is fixed at f_n over the whole velocity range of galloping, being much lower than the Kármán vortex shedding frequency f_v (see Figure 3). This fact, together with the fact that the frequency f_z of the Karman vortex excitation coincides with the structure frequency obtained in fluid otherwise at rest, is the common nature of flow induced vibration of a system with a low damping factor in a low density fluid such as in air flow [1, 9].

4. Suppression of Kármán vortex excitation

Vibration of the isolated square cylinder (i.e. without downstream strip-plate) and the vortex shedding frequency were measured with an increasing and then decreasing flow velocity.

The results thus obtained are plotted against s/d in Figure 5 for five strip-plates with different widths, together with the vortex shedding frequency. By approaching

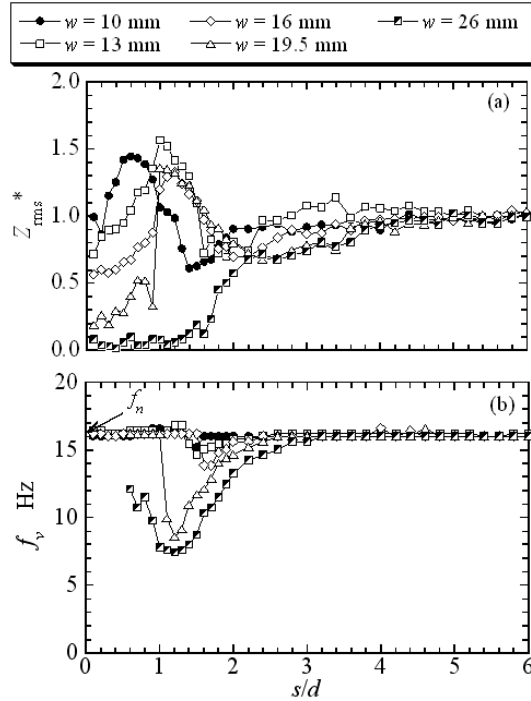


Figure 5. Effect of downstream strip-plate on the Kármán vortex excitation ($U = 3.4$ m/s). (a) Vibration amplitude normalized by its value of isolated cylinder, (b) Vortex shedding frequency (Hot-wire probe position: $x/d = 1.5$, $y/d = 1.25$, $z/d = 0.4$)

the $w = 26$ mm plate ($w/d = 1$), the vibration begins to decrease when $s/d = 4$ and almost completely suppressed when $s/d < 1.5$. However, this effect becomes weaker for narrower plates and it is paradoxical that the vibration amplitude becomes considerably larger than the original Kármán vortex excitation by the plates with $w \leq 19.5$ mm over a certain region of $s/d < 1.5$. The vortex shedding frequency f_v in Figure 5(b) is seen to be considerably lower than f_n or to vanish, when the vibration is small.

In Figure 6, the suppression of Kármán vortex excitation is compared for the cases of three different configuration cruciform systems with $w/d = 1$, i.e. System I : two circular cylinders, System II : circular cylinder and strip-plate, and, System III : square cylinder and strip-plate (the present setting but supported by single plate springs) [10]. In this figure, Z_{rms}^* begins to decrease around $s/d = 2 - 3$ for all the systems. Compared with the other two systems, i.e. System I and System II, the effect is strongest for the System III in the sense that the maximum value of s/d to suppress the vibration is largest among the three.

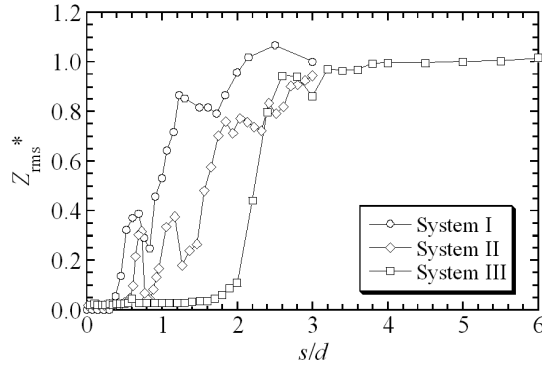


Figure 6. Suppression of Kármán vortex excitation for three systems. System I: Two circular cylinders ($U = 3.0 \text{ m/s}$, $f_n = 24.0 \text{ Hz}$, $\delta = 0.0166$), System II: Circular cylinder and strip-plate ($U = 2.6 \text{ m/s}$, $f_n = 16.7 \text{ Hz}$, $\delta = 0.0078$, $w/d = 1$), System III: Square cylinder and strip-plate ($U = 3.8 \text{ m/s}$, $f_n = 17.0 \text{ Hz}$, $\delta = 0.0690$, $w/d = 1$)

5. Suppression of galloping

The suppression effect of the strip-plate on the galloping was observed in the same way as for the Kármán vortex excitation described above. The velocity was set constant at 7.6 m/s selected as the representative value (see Figure 4) and the results are presented in Figure 7. Compared with the case of Kármán vortex excitation in Figure 5, the effect is more remarkable in that the vibration is completely suppressed with s/d as large as around four when $w/d = 1$. The maximum value of s/d where the vibration begins to become lower is smaller with the smaller width strip-plates. However, there appears again a large vibration when s/d is made still smaller, in the cases of $w = 10 \text{ mm}$, 13 mm and 26 mm . This second vibration peak is indefinite for the plates with intermediate width plates ($w = 16 \text{ mm}$ and 19.5 mm). In the case of the $w = 26 \text{ mm}$ plate, the peak value of the second vibration in the range of $s/d = 1.2 - 1.5$ is larger than double the original galloping. The vortex shedding frequency f_v in this range of s/d is equal to f_n for the $w = 26 \text{ mm}$ plate, while f_v for the second vibration peak is a slightly higher than the value of single cylinder for the $w = 10 \text{ mm}$ and 13 mm plates. Note that the vibration frequency f_z is fixed at f_n for all the measurements shown in Figure 7.

The results shown in Figure 7 infer that the origin of the second vibration peak for the $w = 26 \text{ mm}$ plate is the longitudinal vortex similar to those observed in the two circular cylinder system as shown in Figure 1. In contrast, the second vibration of the $w = 10 \text{ mm}$ and 13 mm plates are not attributed to the longitudinal vortex but may be to the galloping.

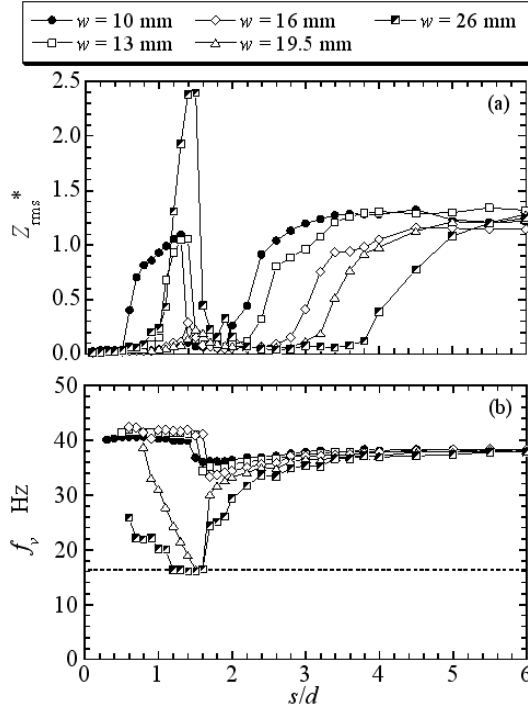


Figure 7. Effect of downstream strip-plate on galloping ($U = 7.6 \text{ m/s}$). (a) Vibration amplitude normalized by its value of isolated cylinder, (b) Vortex shedding frequency (Hot-wire probe position: $x/d = 1.5$, $y/d = 1.25$, $z/d = 0.4$)

6. Longitudinal vortex excitation

The vibration and the vortex shedding frequency of the square cylinder with the $w = 26 \text{ mm}$ plate set at $s/d = 1.2$, the gap at which the second vibration is clearly observed in Figure 7, were measured with an increasing and then decreasing flow velocity U .

Variation of spectra of velocity and displacement for the increasing U is shown in Figure 8. Compared with the isolated square cylinder (Figure 3), spectrum peaks in S_Z around $U = 3.5 \text{ m/s}$ which correspond to Kármán vortex excitation disappear. Instead, sharp spectrum peaks appear in S_Z when $6.5 \text{ m/s} < U < 8 \text{ m/s}$.

Dominant frequencies of the spectra S_u in Figure 8 are plotted against the flow velocity U as a vortex shedding frequency f_v in Figure 9, together with the oscillation amplitude expressed by the RMS value of z -displacement, Z_{rms} . As seen in Figure 9, both the Kármán vortex excitation and the galloping in Figure 4 disappear and a

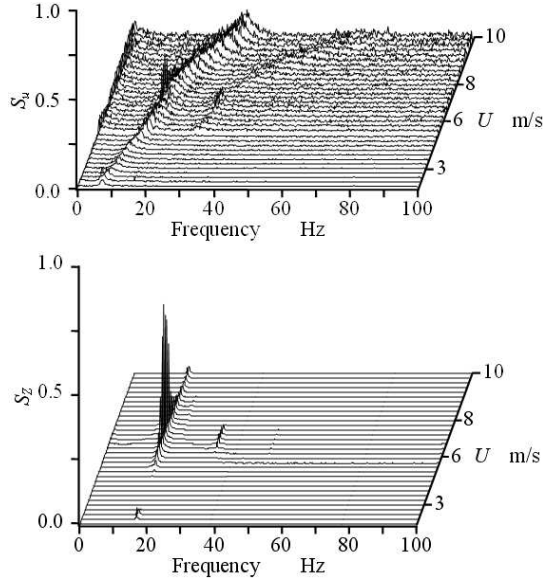


Figure 8. Variation of spectra of velocity and displacement with increasing U for the square cylinder with a strip-plate ($f_n = 16.41$ Hz, $\delta = 0.038$, $w/d = 1$, $s/d = 1.2$, Hot-wire probe position: $x/d = 1.5$, $y/d = 1.25$, $z/d = 0.4$)

new vibration is induced instead over a velocity range of $U = 6.5 - 8$ m/s, where the peak frequency f_v in velocity spectrum remains fixed on $f_z = f_n$.

Except this range of U , f_v increases proportionally with U and is much lower than that of the isolated cylinder. Therefore, the new vibration is inferred to be caused by the longitudinal vortices.

To assure it, the flow downstream the cross of the vibrating square cylinder was visualized by tuft-grid method as shown in Figure 10. There, the cross section of longitudinal vortex is clearly observed at the two anti-phase instants, (a) and (b), in a period of cylinder displacement Z . It is clearly seen that the pattern is symmetric about the $x - z$ plane both in photos (a) and (b), and that the vortex pattern is observed only one side of positive or negative z region. However, it cannot be discerned whether the longitudinal vortex in Figure 10 is the necklace or the trailing vortex shown in Figure 1.

7. Characteristics of longitudinal vortex from fixed system

The square cylinder in the same setting as in Figure 10 was fixed rigidly and the hot-wire probe was traversed towards the side wall parallel to the y -axis. Figure 11 shows velocity spectra for various spanwise positions thus obtained. A sharp peak

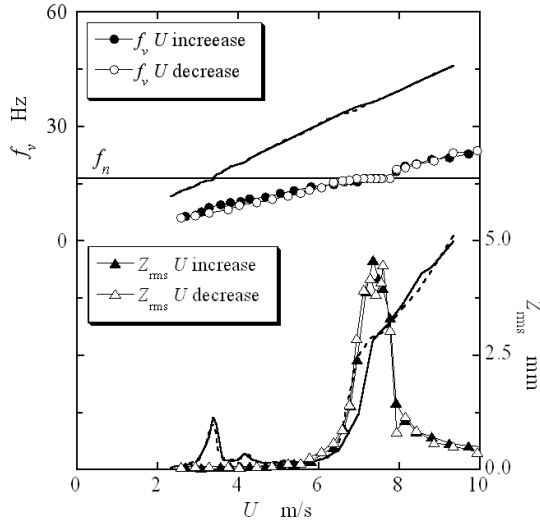


Figure 9. f_v and Z_{rms} versus U for the square cylinder with a strip-plate. $f_n = 16.41 \text{ Hz}$, $\delta = 0.038$, $w/d = 1$, $s/d = 1.2$, Hot-wire probe position: $x/d = 1.5$, $y/d = 1.25$, $z/d = 0.4$, solid line: isolated square cylinder (U increase), broken line: isolated square cylinder (U decrease)

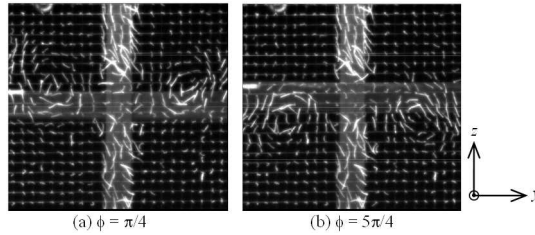


Figure 10. Longitudinal vortices synchronizing with square cylinder oscillation in wind tunnel, viewed from downstream ($w/d = 1$, $s/d = 1.2$, $\delta = 0.069$, single-plate-springs, $Re = 13200$, Grid position: $x/d = 2.7$)

appears in S_u when $y/d < 3$ and no peak is observed beyond this position, showing that the Kármán vortex shedding is removed by the downstream plate.

The hot-wire probe was set at the position where the peak in spectrum S_u is most clearly observed in Figure 11, and the gap s was varied while the velocity U was set constant. The spectra and the peak frequency f_{v0} thus obtained are shown in Figure 12, the latter being normalized by its isolated cylinder value $f_{v0\infty}$ and compared with the results by Fox [11] on a two-square-cylinder system. The peak in S_u in the

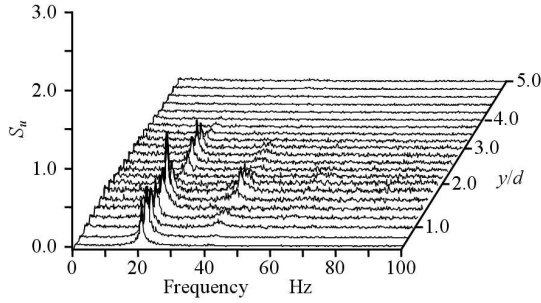


Figure 11. Velocity spectra for various spanwise position ($w/d = 1$, $s/d = 1.2$, $U = 7.6 \text{ m/s}$, Probe position: $x/d = 1.5$, $y/d = 0.8 \sim 5.0$, $z/d = 0.4$)

region $s/d > 5$ is caused by the Kármán vortex with a frequency essentially equal to that of the isolated cylinder. The continuous nature of the changes in the shape and peak frequency of S_u in the region $2 < s/d < 6$ infers that the Kármán vortex sheds there and that its frequency and regularity become lower by the interference of the downstream plate.

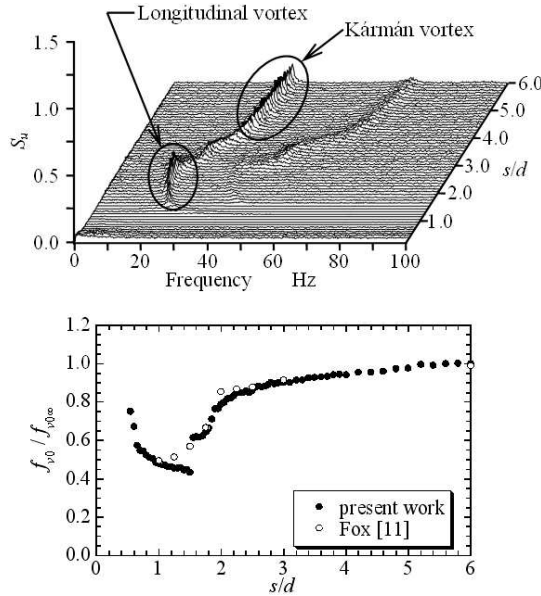


Figure 12. Variation of velocity spectrum and its peak frequency against gap for fixed system ($w = 26 \text{ mm}$, $U = 7.6 \text{ m/s}$, Probe position: $x/d = 1.5$, $y/d = 1.25$, $z/d = 0.4$)

The abrupt changes in S_u and f_{v0} at around $s/d = 1.7$ show that the vortex structure becomes different from that of Kármán vortex when s/d is smaller than this value. The observation of flow as seen in Figure 10, and also by Fox [11], may suggest that the low frequency vortex in the region $s/d < 1.7$ is the necklace vortex as shown in Figure 1 (b). The peak frequency f_{v0} in S_u near the cross of the fixed system is reduced to the Strouhal number S_{t0} and plotted against the Reynolds number Re as shown in Figure 13, together with results for the other two configuration systems. Figures 11 - 13 verify that the periodic shedding of the longitudinal vortex is inherent to this boundary condition but not induced by the cylinder vibration, and show that the Strouhal number of the longitudinal vortex is 0.05–0.06, while that of the Kármán vortex is around 0.13.

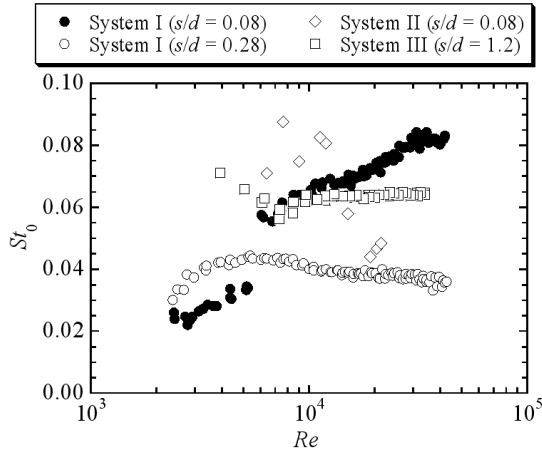


Figure 13. Strouhal number of longitudinal vortices versus Reynolds number for fixed system. System I: Two circular cylinders [5], System II: Circular cylinder and strip-plate [5], System III: Square cylinder and strip-plate (present system)

8. Conclusions

Wind tunnel experiment was carried out to investigate interference effect of a strip-plate set downstream in cruciform arrangement on the crossflow vibration behavior of a square cylinder in uniform flow. The results are compared with different configuration systems, i.e. cruciform two-circular-cylinder and circular-cylinder/strip-plate systems. The conclusions are summarized as follows.

1. Both the Kármán vortex excitation and the galloping of the square cylinder are effectively suppressed by the downstream strip-plate in spite of the fact that the mechanisms of the two vibrations are absolutely different.

2. A longitudinal vortex excitation similar to that observed for the two-circular-cylinder system is induced by the downstream strip-plate over a range of non-dimensional gap s/d considerably larger compared with the latter.

Generally speaking, effect of a cruciform downstream strip-plate is stronger in the square-cylinder/strip-plate configuration in the sense that the range of s/d to influence the vibration is much larger than in the other two cases. Most remarkable effect is that the galloping is completely suppressed by the $w/d = 1$ strip-plate even when the gap is as large as four times the side length of square.

However, the above effects of the downstream plate are largely different when the width of the plate is smaller. Since the flow around the cross is of highly three dimensional nature accompanied with periodic vortex shedding of longitudinal vortices superimposed by turbulence, mechanisms to cause the influences on vibration are left for further investigations.

Acknowledgement. The authors would like to thank Mr. Ohta, M. for his experimental supports.

References

1. BLEVINS, R.D.: *Flow-Induced Vibration*. 2nd Ed., Van Nostrand, 1990.
2. TOMITA, Y., INAGAKI, S., SUZUKI, S. AND MURAMATSU, H.: Acoustic characteristics of two circular cylinders forming a cross in uniform flow. *JSME International Journal*, **30**, (1987), 1069-1079.
3. SHIRAKASHI, M., BAE, H.M., SANO, M., AND TAKAHASHI, T.: Characteristics of periodic vortex shedding from two cylinders in cruciform arrangement. *Journal of Fluids and Structures*, **8**, (1994), 239-256.
4. TAKAHASHI, T., BARANYI, L., AND SHIRAKASHI, M.: Configuration and frequency of longitudinal vortices shedding from two cylinders in cruciform arrangement. *Journal of the Visualization Society of Japan*, **19**(75), (1999), 328-336.
5. KATO, N., KOIDE, M., TAKAHASHI, T. AND SHIRAKASHI, M.: Influence of cross-sectional configuration on the longitudinal vortex excitation of the upstream cylinder in cruciform two-cylinder system. *Journal of Fluid Science and Technology*, **1**(2), (2006), 126-137.
6. KAMIMURA, Y., KOIDE, M., TAKAHASHI, T. AND SHIRAKASHI, M.: Effect of slenderness on cross-flow oscillation of a rectangular cylinder supported by cantilever in uniform flow, Proceedings of CMFF'03, The 12th International Conference on Fluid Flow Technologies, (2001), pp. 399-406.
7. SHIRAKASHI, M., ISHIDA, Y. AND WAKIYA, S.: Higher velocity Resonance of Circular Cylinder in Crossflow. *Journal of Fluids Engineering*, **108**, (1986), 392-396.
8. KOIDE, M., TAKAHASHI, T. AND SHIRAKASHI, M.: Development of a Ring-Type Vortex Anemometer for Low-Velocity Wind Tunnel Experiments. *Bulletin of Japan Society of Mechanical Engineers*, (in Japanese), **67**, 657, B, (2001), 1105-1111.
9. SARPKAYA, T.: A critical review of the intrinsic nature of vortex-induced vibrations. *Journal of Fluid and Structures*, **19**, (2004), 389-447.

10. KATO, N., KOIDE, M., TAKAHASHI, T. AND SHIRAKASHI, M.: Interference of downstream body on the oscillation behavior of a circular and a square cylinder in uniform flow, Proceedings of PVP (2005), PVP2005-71517, July 17-21, Denver, Colorado USA.
11. FOX, T.A.: Interference in the wake of two square-section cylinders arranged perpendicular to each other. *Journal of Wind Engineering and Industrial Aerodynamics*, **40**(1), (1992), 75-92.

VORTEX CLOUD FLOW MODELLING OF CYLINDERS IN ORBITAL MOTION AT LOW REYNOLDS NUMBERS AND COMPARISONS WITH SOME PUBLISHED GRID-BASED CFD PREDICTIONS

R.IVAN LEWIS

2-16 Bruce Building, Newcastle University
Newcastle upon Tyne, NE1 7RU, U.K.

`r.i.lewis@ncl.ac.uk`

[Received: January 11, 2007]

Abstract. Cylinders in elliptical orbital motion at low Reynolds numbers (Re) have been fairly extensively researched by grid-based Computational Fluid Dynamic (*CFD*) methods, revealing discontinuous behaviour of the root mean square (*rms*) lift coefficient from positive to negative values for low transverse amplitudes and orbital periodicity close to the Strouhal number for the fixed cylinder. Following published grid-based analyses, this paper studies a few flows for Re values of 130, 160 and 180 with orbital periodicity set at 85 % of the Strouhal frequency. The orbital amplitude in the mainstream flow direction A_x is fixed at 0.3 of the cylinder diameter, while the transverse amplitude is varied over the range $0 < A_y < 0.3$. A brief outline of the vortex cloud analysis is first given followed by a presentation of predicted lift and drag coefficients for this range of flow conditions plus selected flow patterns for regions of main interest. While the detailed predicted C_{Lmean} results are not identical to the published grid-based analysis, similar proneness to this switching phenomenon is found to occur. The flow mechanism underlying this is shown to be that of vortex pair formation in the downstream wake and is illustrated by predicted vortex-cloud patterns.

Keywords: vortex cloud modelling, cylinder wake flows, cylinder orbital motion

1. Introduction

Formation of vortex streets behind bluff bodies has fascinated large numbers of researchers since the early experiments of Strouhal [1] in 1878 concerning the generation of ‘Aeolian tones’ and the famous 1911 paper by Theodore von Kármán [2] bequeathing his name to the ‘von Kármán vortex street’. Vortex streets are created as the outcome of periodic shedding of vorticity created initially at the surface and subsequently diffused and convected within the body boundary layer. The consequent fluctuations result in large periodic variation of the lift and drag forces and their associated lift and drag coefficients C_L and C_D defined as follows for a cylinder of

diameter d in a uniform stream U_∞

$$C_L = \frac{L}{\frac{1}{2}\rho U_\infty^2 d}, \quad C_D = \frac{D}{\frac{1}{2}\rho U_\infty^2 d}. \quad (1.1)$$

Shedding frequency f_v is categorised by the dimensionless Strouhal number S_t defined

$$S_t = \frac{f_v d}{U_\infty}. \quad (1.2)$$

As discussed elsewhere [3-5], the onset of regular vortex street shedding occurs above $Re \approx 47$ and remains two-dimensional in character until $Re \approx 190$, above which, as convective processes gain ascendancy over viscous diffusion, three-dimensional instabilities begin to occur as proven theoretically by Barkley and Henderson [6] and Posdziech and Grundmann [7] and experimentally by Williamson [8]. The present studies using two-dimensional modelling are thus restricted to this range but towards the upper end for the three values $Re = 130, 160$ and 180 for which convective processes begin to dominate.

Because of vortex wake periodicity, flexibly mounted bodies such as struts, heat exchanger tubes, chimney stacks etc. may deflect and oscillate in response to these forces, possibly in linear or orbital motion. In such cases the vortex shedding properties will change resulting in quite different lift and drag variations with time. The main aim of this paper is to simulate these conditions for a cylinder in elliptical orbital motion at low Reynolds numbers. Studies of this type were previously undertaken by Baranyi [3, 4] employing a very precise grid-based Eulerian type method of *CFD* for solving the two-dimensional Navier Stokes equations. Vortex cloud modelling provides a quite different *CFD* method based on Lagrangian modelling of the same situation and the second aim of this paper is to compare results obtained by these two techniques of fluid-flow simulation. Such comparisons of the now well established *CFD* codes for classical datum cases are crucial at this stage of increasingly wide engineering design/analysis application and one such paper has already been published by Baranyi and Lewis [5] for low Re flow past a stationary cylinder. The present paper extends these cross-checks to cylinders in orbital motion.

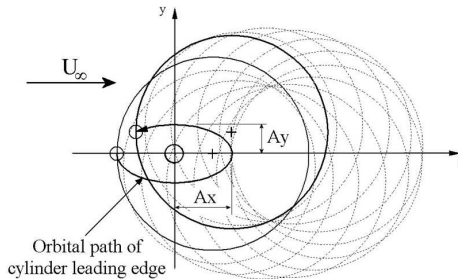


Figure 1. Elliptical path for a cylinder in orbital motion

The main advantage of the vortex cloud model is its ability to keep account of all the vorticity in the downstream wake without the restriction of any reference grid and the consequent ease for obtaining simulated wake patterns. A full account of the fundamentals of vortex cloud analysis has been given by Lewis [9] and of its application to moving bodies and cascades [10, 11]. Thus only a brief summary of the underlying theory will be given here in section (2) followed in section (3) by comparisons of predicted lift and drag coefficients and presentation of selected wake patterns. Before proceeding with this we begin with a presentation of the underlying geometrical definitions of the proposed orbital motion as illustrated in Figure 1.

As shown here the cylinder is located in a uniform stream U_∞ but subjected to an orbital motion following an elliptical path with semi-major and minor axes A_x , A_y where the cylinder leading edge point O is taken here to define this path. In practice oscillations might occur with different frequencies f_x and f_y parallel to the x and y axes. For elliptical motion however we will impose equal values $f = f_x = f_y$ and adopt anticlockwise motion beginning in the downstream direction for which the cylinder displacements at time t are given by

$$x_0 = -A_x \cos(2\pi ft), \quad y_0 = -A_y \sin(2\pi ft) \quad (1.3)$$

and its velocity components u_0 and v_0 are thus

$$u_0 = 2\pi f A_x \sin(2\pi ft), \quad v_0 = 2\pi f A_y \cos(2\pi ft). \quad (1.4)$$

2. The vortex cloud flow simulation method

The flow model for vortex cloud analysis is illustrated in Figure 2. At any instant the flow past the cylinder generates a surface vorticity sheet of local strength $\gamma(s) = v_s$ equal in magnitude to the surface slip-velocity v_s . If the cylinder is represented by M surface elements, the vorticity at element n is assumed to be shed as a discrete vortex element of strength $\Delta\Gamma_n = \gamma(s_n)\Delta s_n$. Although only 12 elements are shown in Fig. 2, typically fifty surface elements would be adopted for acceptable resolution as in the present project. For further accuracy sub-elements may be used as illustrated in Fig. 2(b), where the line vortex element $\gamma(s_n)\Delta s_n$ has been modelled by three sub-elements of strength $\Delta\Gamma_n = \frac{1}{3}\gamma(s_n)\Delta s_n$.

The governing integral equation is then given by [9]

$$\begin{aligned} \frac{1}{2}\gamma(s_m) + \oint k(s_m, s_n) \gamma(s_n) ds_n + (U_\infty - u_0) \cos \beta_m + (V_\infty - v_0) \sin \beta_m + \\ + \sum_{j=1}^Z \Delta\Gamma_j (U_{mj} \cos \beta_m + V_{mj} \sin \beta_m) = 0 \end{aligned} \quad (2.1)$$

which states that the velocity on and parallel to the body surface of point m is zero. This equation may be represented numerically by the following set of M linear

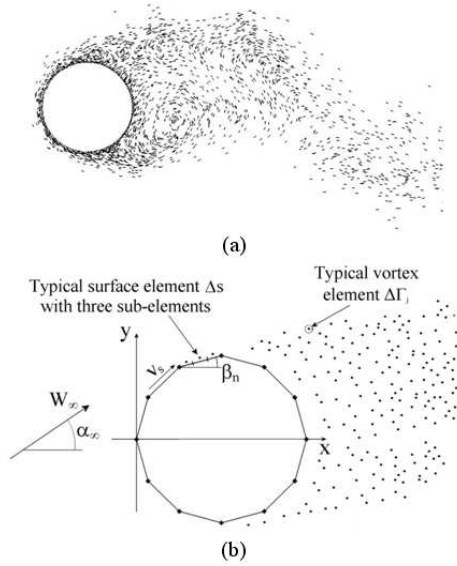


Figure 2. Numerical model for vortex cloud analysis. (a) Vortex cloud wake flow simulation, (b) Numerical model

equations,

$$\sum_{n=1}^M K(s_m, s_n) \gamma(s_n) = -(U_\infty - u_0) \cos \beta_m - (V_\infty - v_0) \sin \beta_m - \sum_{j=1}^Z \Delta \Gamma_j (U_{mj} \cos \beta_m + V_{mj} \sin \beta_m) \quad (2.2)$$

where the cylinder is located in the uniform stream W_∞ and Z discrete vortex elements $\Delta \Gamma_j$ have been shed into the fluid since initiation of the motion.

The vortex cloud computations are undertaken in a time-stepping sequence, in the present case for 3000 steps of size $\Delta t = 0.05$, with a uniform stream $W_\infty = U_\infty = 1.0$ and a cylinder diameter $d = 1.0$. A summary of the computations undertaken for each time step is as follows:

Vortex Cloud analysis time-stepping procedure

1. Potential flow analysis by equation (2.2), to calculate the body surface slip flow and the newly created surface vorticity $\gamma(s_j)$.
2. The shedding of discrete vortices $\Delta \Gamma_j = \gamma(s_j) \Delta s_j$ from each surface element, thus creating a cloud of vortex elements.
3. Use of the random walk procedure [9] for each discrete vortex $\Delta \Gamma_j$ to simulate viscous diffusion over the time step Δt .
4. Mutual convection of all members of the vortex cloud for this time step.

5. Recombination of any vortices that become excessively close due to the random walk. This has the beneficial side effect of reducing the total volume of the vortex cloud.

6. Deletion of any discrete vortices which stray inside the body profile during diffusion and imposition of the circulation theorem to ensure that the equivalent loss is restored during the subsequent potential flow analysis (step 1 above) in order to ensure overall conservation of vorticity.

Output data of importance to categorise the resulting motions are the predicted vortex wake motions and the lift and drag coefficients C_L , C_D . In view of the oscillatory nature of the latter, helpful practice is to evaluate their average values and their rms fluctuations, defined as follows.

$$C_{Lmean} = \frac{1}{t_2 - t_1} \int_{t_1}^{t_2} C_L dt$$

$$C_{Lrms} = \sqrt{\frac{1}{t_2 - t_1} \int_{t_1}^{t_2} [C_L - C_{Lmean}]^2 dt} \quad (2.3)$$

and similarly for C_{Dmean} and C_{Drms} , where the interval t_1 to t_2 includes a large number of completed oscillations.

3. Predicted results for three test cases

Baranyi [3] published results predicted by his grid-based *CFD* method for the three configurations given in Table 1, which will be the focus of the present studies. The orbital semi-major axis A_x is fixed at 0.3 for all cases and the semi-minor axis is varied over the range $0.0 \leq A_y \leq 0.3$. For each Re value the orbital frequency f is set at 85 % of the Strouhal number for the fixed cylinder.

Table 1. Parameters for test cases

Case	Re	f	A_x	A_y range
1	130	0.1521	0.3	0.0 to 0.3
2	160	0.1598	0.3	0.0 to 0.3
3	180	0.165665	0.3	0.0 to 0.3

Vortex cloud calculations were undertaken for these three test cases for a cylinder modelled by 50 elements, with two sub-elements. Further to this, to reduce the "numerical noise" inherent in the random walk model for viscous diffusion, it was also decided to undertake the viscous diffusion in three sub-steps of value $\frac{1}{3}\Delta t$. Vortex cloud predictions will now be presented for these three cases in comparison with Baranyi [3].

3.1. **Case 1:** $Re = 130$, $f = 0.1521$. The mean and rms lift and drag coefficients are compared in Figure 3, where, of particular interest, are the predicted C_{Lmean} values. As previously predicted by Baranyi, Fig. 3(a), these resolve into two distinct envelopes that show a major discontinuity in the lower range of A_y values. His results shift discontinuously from the upper envelope to the lower one at $A_y \approx 0.02$ and revert to the upper at $A_y \approx 0.07$.

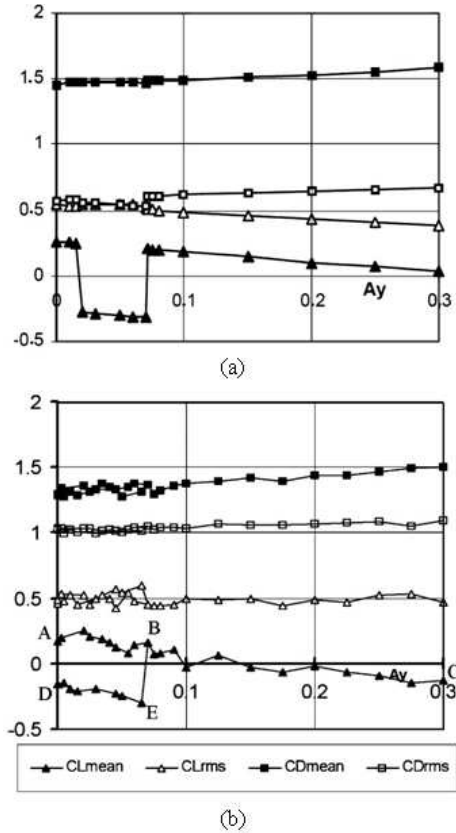


Figure 3. Comparison of predicted force coefficients for $Re = 130$, $f = 0.1521$, $A_x = 0.3$. (a) Baranyi [3] – Grid based method, (b) Lewis – Vortex cloud method

The present vortex dynamics predictions, Fig. 3(b), show good general agreement of C_{Lmean} with Baranyi's results but with some very interesting variations in the lower range $A_y < 0.07$ for which results fell on either the upper envelope ABC or the lower one DEB . The immediate deduction to be drawn from this is the likelihood of some major instability between two possible stable vortex wake regimes and we will return to this later. Good agreement was also obtained between the two methods

for the predicted values of C_{Lrms} and C_{Lmean} but less so for C_{Lrms} for which vortex cloud modelling shows much higher values.

Next we will take a look at the actual variations of C_L and C_D with time, see Figure 4 below.

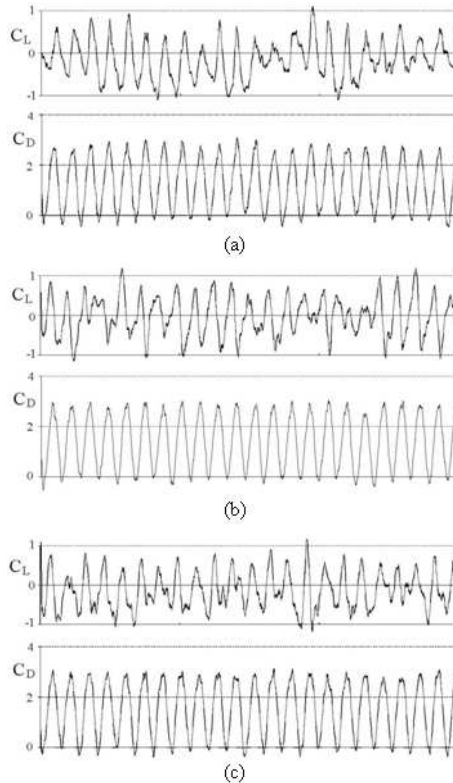


Figure 4. Predicted lift and drag coefficients for $Re = 130$, $f = 0.1521$. (a) $A_x = 0.3$, $A_y = 0.0$, (b) $A_x = 0.3$, $A_y = 0.15$, (c) $A_x = 0.3$, $A_y = 0.3$

The predicted variations with time of C_L and C_D are shown in Fig. 4 for $A_x = 0.3$ for three values of A_y spanning the orbital range from purely horizontal motion $A_y = 0.0$, on to elliptical motion $A_y = 0.15$ and finally for circular motion $A_y = 0.3$. The C_D curves are remarkably similar which explains the fairly constant values for C_{Dmean} and C_{Drms} in Fig. 3 and it is of some interest to note that this wide variation in orbital motion should have such little impact on the magnitude and character of the drag coefficient. On the other hand much more variation can be observed in the predicted lift coefficient C_L . There are fluctuations in the amplitude and variations in the predicted wave pattern for all three cases but increasingly so as the vertical

orbital displacement A_y is increased. The most regular of these is for horizontal motion $A_y = 0.0$, Fig. 4(a), particularly over the first half of the time sequence. Attention should be drawn to the general wave shape which has sharp maxima and more rounded minima, a characteristic discovered by Baranyi [3]. This same feature is conspicuous in Fig. 4(c) for circular motion, $A_y = 0.3$, if less conspicuously so for the elliptical orbit, Fig. 4(b).

For further insight into some of these characteristics we will now focus attention on predicted wake patterns for these three orbital cases, Figure 5.

Figure 5 portrays the predicted wake patterns for these three cases in comparison with that for the motionless cylinder with its typical von Kármán vortex street, Fig. 5(a). Here the cylinder in practice sheds vortices of alternate sign and equal magnitude into the wake at regular intervals, namely the Strouhal frequency St , as borne out here by vortex cloud simulation. The predicted flow pattern for purely horizontal motion, Fig. 5(b), is quite similar to this but with some evidence of vortex pairing of the two +ve and -ve vortices shed during each orbit. For the cylinder in orbital motion however, Figs. 5(c) and 5(d), much more development of this phenomenon is observed, namely the formation in the wake of very distinct vortex pairs. Thus in Fig. 5(c), attention is drawn to the pairing of a clockwise +ve vortex shed from the upper surface with an anticlockwise -ve vortex shed slightly previously from the lower surface and we observe also a new vortex pair being shed just downstream of the cylinder as it completes its upstream orbiting motion. These +/- vortex pairs have a natural self-convection effect in the downwards direction resulting in a general net downward drift of the cylinder wake. The same phenomenon can be observed in Fig. 5(d) for the circular orbit. Once again the vortex pairing is of +/- type as for the elliptical orbit, Fig. 5(c). It is of particular interest to observe however that the opposite +/- vortex pairing occurred for the case of purely horizontal motion $A_y = 0.0$ shown here in Fig. 5(b). In this case, Fig. 3(b), the related C_{Lmean} value was at point *D* located on the lower envelope whereas the C_{Lmean} values for the elliptical and circular orbiting cases $A_y = 0.15$ and 0.3 actually lie on the upper envelope. There thus seems to be a direct connection between the sign of vortex pairing and the particular envelope on which the C_{Lmean} results lie.

3.2. Case 2: $Re = 160$, $f = 0.1598$. Results for the higher Reynolds number of $Re = 160$ are shown in Figure 6 where the behavioural trends of C_{Lmean} are again similar for the two *CFD* methods, with good agreement for the wider orbiting range $0.15 < A_y < 0.3$. As before Baranyi discovered the switching of C_{Lmean} between upper and lower envelopes, in this case for $A_y > 0.07$. However it is of considerable interest to note that his predicted C_{Lmean} curve is an inversion of that for $Re = 130$, Fig. 5(a). Vortex cloud predictions here suggest a more progressive switch over the range $0.09 < A_y < 0.15$ and many more points were obtained on the lower envelope than the upper for $A_y < 0.08$. The reason for the greater stability of the C_{Lmean} curves for the higher A_y values is probably due to the stronger stirring effect of the wider elliptical orbit shedding large amounts of clockwise vorticity. This leads here

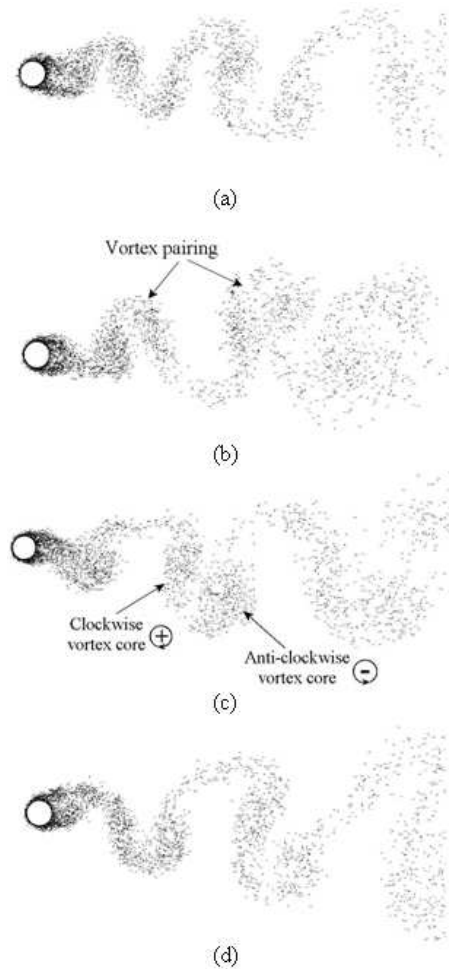


Figure 5. Predicted wake flow for $Re = 130$ for various orbits. (a) Motionless cylinder with zero orbital motion, $f = A_x = A_y = 0.0$, (b) Cylinder in orbital (horizontal) motion with $f = 0.1521$, $A_x = 0.3$, $A_y = 0.0$, (c) Cylinder in orbital (elliptical) motion with $f = 0.1521$, $A_x = 0.3$, $A_y = 0.15$, (d) Cylinder in orbital (circular) motion with $f = 0.1521$, $A_x = 0.3$, $A_y = 0.3$

to anticlockwise bound vorticity and large negative lift. However one stray point A was found for $A_y = 0.21$ seeming to lie on the extended upper envelope, Fig. 6(b).

A re-run of this situation resulted in the C_{Lmean} value B lying on the lower envelope having the normal vortex pairing, as can be seen from Figure 7 below.

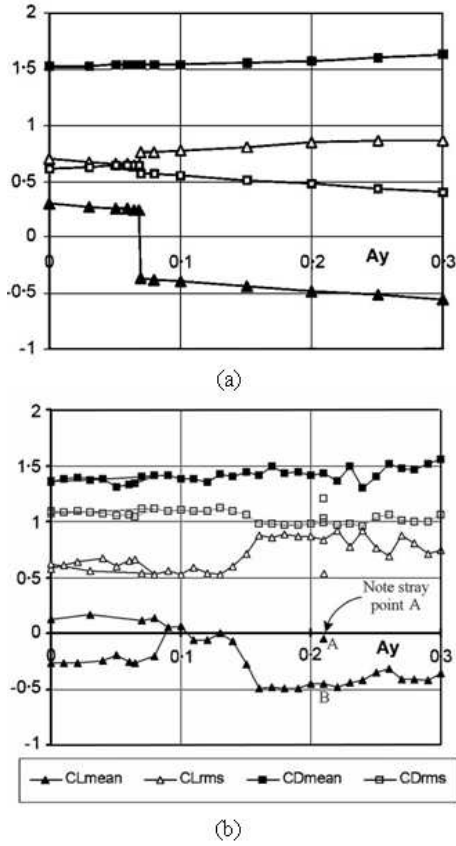


Figure 6. Comparison of predicted force coefficients for $Re = 160$, $f_x = f_y = 0.1598$, $A_x = 0.3$. (a) Baranyi - Grid based method, (b) Lewis - Vortex cloud method

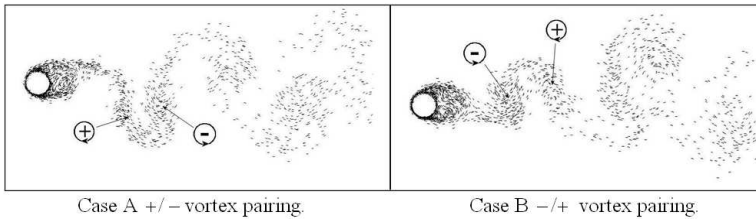


Figure 7. Opposite vortex pairing of points A and B in Fig. 6

As can be seen from Figure 7 the stray point A has +/- vortex pairing which is opposite to the normal more stable -/+ pairing of Case B. What is of particular

importance to note here however is that at the higher Re of 160 the vortex pairing for the wider y orbital range of $0.07 < A_y < 0.3$ of stable vortex motion is of Case $B -/+$ type which is quite contrary to that exhibited for $Re = 130$ orbital motion where the stable vortex pairings were of $+/-$ type, a remarkable switch of behaviour for such a small Reynolds number rise. Comparing Baranyi's results for these two Reynolds numbers, Figs. 5(a) and 6(a), the same shift of vortex pairing between the $+/-$ and $-/+$ types was in all probability also occurring, judging by the shift from the upper envelope to the lower for $A_y > 0.07$. We now consider results for a further increase to $Re = 180$ for the same orbital motions.

3.3. Case 3: $Re = 180$, $f = 0.165665$. Predicted results for the third case at the highest Reynolds number $Re = 180$ with orbital frequency $f = 0.165665$ are shown in Figure 8. As before Baranyi [3], Fig. 8a, found there to be two envelopes, with a fairly similar distribution of C_{Lmean} . Thus all C_{Lmean} values for $A_y > 0.1$ are lying on the lower envelope following the same trend as the $Re = 160$ results. For $A_y < 0.1$ on the other hand his predicted values lay mainly on the upper envelope with deviations from this in the very low y amplitude range $A_y \approx 0.004$ to 0.02.

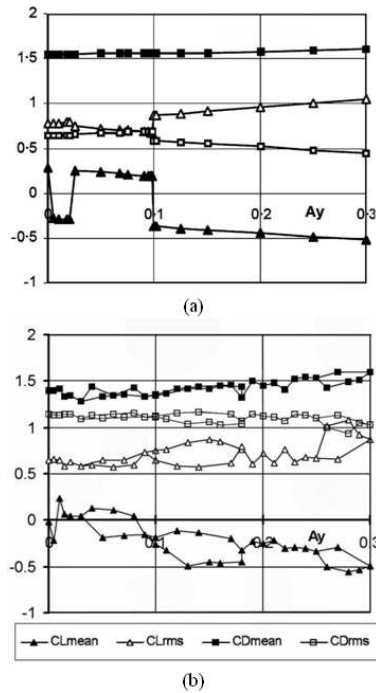


Figure 8. Comparison of predicted force coefficients for $Re = 180$, $f_x = f_y = 0.165665$, $A_x = 0.3$. (a) Baranyi - Grid based method, (b) Lewis - Vortex cloud method

Predicted results for the third case at the highest Reynolds number $Re = 180$ with orbital frequency $f = 0.165665$ are shown in Figure 8. As before Baranyi [3], Fig. 8a, found there to be two envelopes, with a fairly similar distribution of C_{Lmean} . Thus all C_{Lmean} values for $A_y > 0.1$ are lying on the lower envelope following the same trend as the $Re = 160$ results. For $A_y < 0.1$ on the other hand his predicted values lay mainly on the upper envelope with deviations from this in the very low y amplitude range $A_y \approx 0.004$ to 0.02 .

Vortex cloud analysis predicted similar overall trends for the lower envelope for $A_y > 0.1$ but also, surprisingly, the presence of an upper envelope over most of this wider orbiting range. The strategy adopted here on the evidence of section 3.2 was to plot points with $+/-$ vortex pairing on the upper envelope and $-/+$ pairs on the lower one. Within the small range $0.18 < A_y < 0.25$ however no points were found on the lower envelope. It is difficult to escape the conclusion, comparing Figs. 3, 6 and 8, that these developments of the upper envelope for the range $A_y > 0.1$ at the increasing Reynolds number are caused by the progressive dominance of convection over viscous diffusion. At the lower orbital range of $A_y < 0.1$ the same indeterminacy of vortex pairing type is present and the upper envelope is in good agreement between the two *CFD* methods. A couple of points were however still found on the lower envelope by vortex cloud modelling.

Another feature of test runs for $Re = 180$ was the tendency so switch occasionally between the $+/-$ and $-/+$ vortex pairing modes for some of the A_y values. Similar switching occurred to a very limited extent at $Re = 160$ in the lower A_y range. At these lower Re values of 130 and 160 however stable locking of the vortex pairs generally occurred as the norm for each test run.

4. Conclusions

The following conclusions may be drawn from this study:

1. Reasonable agreement has been obtained between a high resolution grid based *CFD* method and vortex cloud modelling of cylinders in orbital motion within the low Re range 130 to 180, with special focus on the time averaged lift coefficient C_{Lmean} . Best agreement was obtained at the lower Reynolds number $Re = 130$.
2. Although vortex shedding is dependent ultimately upon boundary layer formation and separation, which is more rigorously modelled in the grid-based method of Baranyi, for bluff body flows periodic vortex shedding is also strongly dominated by the upstream influence of vortex formation and convective patterns within the downstream wake for which both *CFD* methods are well adapted.
3. Both methods revealed the presence of upper and lower envelopes of the C_{Lmean} curves. For $Re = 130$ results for the larger y orbits over the range $0.1 < A_y < 0.3$ lay on the upper envelope. For $Re = 160$ and 180 however C_{Lmean} values predicted by Baranyi lay on the lower envelope over this range.
4. For the higher Reynolds number $Re = 180$ however, the present method predicted the presence of C_{Lmean} values lying on both upper and lower envelopes

over almost the entire y orbiting range $0.023 < A_y < 0.3$ which has been attributed to the greater influence of convective motions as one approaches the upper limit of $Re \approx 190$ below which the flow locks into two-dimensional motion and above which three-dimensional instabilities begin to set in.

5. The present studies have revealed that the orbital motion results in regular vortex pairing in the downstream wake. These are shown to be of the two possible types, namely $+/-$ and $-/+$. Points on the upper envelope are found to be of $+/-$ type and those on the lower envelope are of $-/+$ type.

6. Wake patterns at the higher $Re = 180$ were sometimes found to switch between $+/-$ and $-/+$ type, whereas at the lower Reynolds numbers much more stable locking of the vortex pairs was occurring as the norm.

References

1. STROUHAL, V.: Über eine besondere Art der Tonerregung. *Ann. Phys. und Chemie. Nav. Series* **5**, (1878), 216-251.
2. KÁRMÁN T. VON.: Über ein Mechanismus des Widerstandes, den ein bewegter Körper in einer Flüssigkeit erfährt. *Göttingen Nachrichten Maths, -Phys.*, (1911), KI., 509-517.
3. BARANYI, L.: Numerical simulation of flow past a cylinder in orbital motion. *Journal of Computational and Applied Mechanics* **5**(2), (2004), 209-222.
4. BARANYI, L.: Lift and drag evaluation in translating and rotating non-inertial systems. *Journal of Fluids and Structures*, **20**, (2005), 25-34.
5. BARANYI, L. AND LEWIS, R.I.: Comparison of a grid-based CFD method and vortex dynamics predictions of low Reynolds number cylinder flows. *The Aeronautical Journal*, **110**(1103), (2006), 63-71.
6. BARKLEY, D. AND HENDERSON, R.D.: Three-dimensional Floquet stability analysis of the wake of a circular cylinder. *Journal of Fluid Mechanics*, **332**, (1996), 215-241.
7. POSDZIECH, O. AND GRUNDMANN, R.: Numerical simulation of the flow around an infinitely long circular cylinder in the transition regime. *Theoretical and Computational Fluid Dynamics*, **15**, (2001), 121-141.
8. WILLIAMSON, C.H.K.: Vortex dynamics in the cylinder wake. *Annual Review of Fluid Mechanics*, **28**, (1996), 477-539.
9. LEWIS, R.I.: *Vortex Element Methods for Fluid Dynamic Analysis of Engineering Systems*. Cambridge University Press, Cambridge, 1991.
10. SLEWIS, R.I.: Development of Vortex Dynamics for Simulation of Turbomachine Cascades and Blade Rows. *J. Comp. App. Mech.*, **2**(1), (2001), 73-85.
11. LEWIS, R.I.: Study of blade to blade flows and circumferential stall propagation in radial diffusers and radial fans by vortex cloud analysis. *Journal of Computational and Applied Mechanics*, **5**(2), (2004), 323-335.

REDUCING THE ATHLETE'S AERODYNAMICAL RESISTANCE

LUCA OGGIANO, LARS SAETRAN, SVEINUNG LOSET, RONNY WINTHER
Faculty of Engineering Science and Technology, Norwegian University of Science and
Technology
N-7491 Trondheim, Norway
luca.oggiano@ntnu.no

[Received: January 15, 2007]

Abstract. This paper presents an experimental investigation on the effect of surface roughness on athletes legs and arms. Because of their cylindrical shape, arms and legs of an athlete can be approximately studied as flow over circular bodies. The variation of roughness has been obtained using three different textiles and changing the diameter of the cylinder. To evaluate the results, three more textiles have been tested on the 20cm diameter cylinder. Two of them are utilized in two alpine suits used by the Norwegian alpine ski team and one is from a ski suit produced by Eschler. All the results have been compared with a cylinder with a smooth surface. The critical Reynolds number for a significant drop in the drag coefficient decreases by increasing surface roughness.

Keywords: aerodynamic, bluff bodies, cylinder, drag, roughness, sport.

1. Introduction

In many sports the aerodynamical resistance (*drag* – D) is of primary importance for the athlete's performance - e.g. in speed-skating where D is about 80 % of the physical forces acting against the athlete's speed; and in a ski-jumper's in-run where the velocity at take-off is determined by 60 % for the ski/snow friction and 40 % by D .

Estimates using these figures show that a speed-skater will reduce his lap-time by one tenth of a second per % reduced D , and that a ski-jumper can increase significantly the velocity at take-off by a modest reduction in D .

D can be defined as:

$$D = \frac{1}{2}c_dAV^2 \quad (1.1)$$

The drag D is proportional to the square of the velocity V , where c_dA is the product of the Drag coefficient and a characteristic cross sectional area - and is an important parameter to evaluate and work on to minimize.

One can work on this parameter by either 1) reducing and 'streamlining' the body, and/or 2) by manipulating the flow close to the body such that flow separation from the body is delayed - producing a smaller wake zone and thereby less drag force.

The athletes themselves normally have no quantitative feedback on how effective their body posture and equipment is minimizing D . The wind tunnel equipped with instrumentation for measurement of physical forces represents an efficient way of quantitatively optimizing body posture and develop aerodynamically clothing and equipment for the athletes.

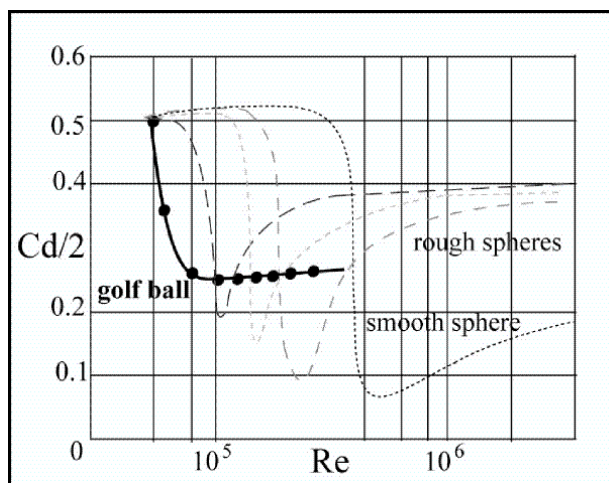


Figure 1. Variation of c_d with Reynolds number for smooth and rough sphere and golf ball. [5]

For a speed-skater the leg, from the skate and up to the knee, represents about 1/3 of the skater's total air resistance. By tripping the airflow boundary layer on the leg, using certain material textures, separation can be delayed and the leg's D significantly reduced.

Working on body postures for ski-jumpers (in-run) resulted in an increased speed of 1 km/h at take-off for the Norwegian national team (in average). In the experiments carried out it has been chosen to focus the attention on the reduction of drag in legs and arms using different textiles with different surface roughness (or dimples).

Using the approximation that legs and arms are cylindrically shaped the textiles has been tested on cylinders with different diameters.

For smooth cylinders in a cross flow the critical Reynolds number (when transition occurs and the drag coefficient fall) is around $3 \cdot 10^5$. The introduction of surface roughness on the cylinder surface can shift the transition to lower Reynolds number.

Increasing the roughness parameter induce a reduction in the value of the critical Reynolds number but also a lower the fall in c_d . That has been shown by Achenbach

[2] for spheres and by Bearman and Harvey [5] for cylinders. From Achenbach's experiments [2], for the post-critical regime, to increase the roughness on a sphere means increasing the drag coefficient if it is compared with a smooth surface sphere (see Figure 1).

Flows around spheres and cylinders are very similar so it can be expected that the results carried on from the experiments done will be close to the results of what Achenbach [2] and Bearman-Harvey found [3, 5]. The target is to obtain the same drag reduction for a cylinder as obtained for a golf ball (Figure 1) by covering the cylinder surface with clothing of different textures thereby varying the roughness coefficient.

This will permit the estimation of the drag reduction in the cylindrical parts of the athlete's body.

2. Effect of transition and separation

The total drag can be split in two different parts. A part of drag is due to skin friction

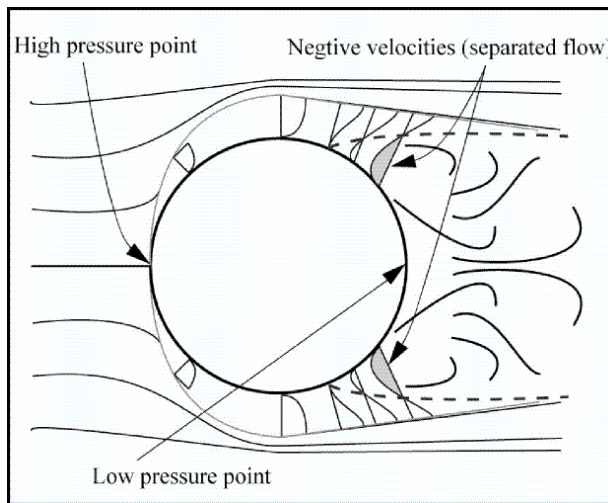


Figure 2. Flow around cylinder

and is called friction drag and another part is due to the difference between the high pressure in the front part of the body (close to the stagnation point) and the low pressure on the rear region (separated region) and is called pressure drag.

$$c_{dTOT} = c_{dFRICITION} + c_{dPRESSURE} \quad (2.1)$$

The relative contribution of friction and pressure drag depends on the body shape, especially its thickness. The cylinder is a bluff body and most of the drag, even with a rough surface, will be contributed by the pressure drag.

For cylinders (and in general for bluff bodies) the transition from laminar to turbulent increases the skin friction because of the Reynolds stress but, on the other hand, the pressure drag decreases by a large margin by moving the separation point to the back of the cylinder and diminishing the width of the wake.

3. Experimental setup

3.1. Wind tunnel. For the experiments, the wind tunnel of NTNU (Norwegian University of Science and Technology) in Trondheim has been used. (Figure 3). The

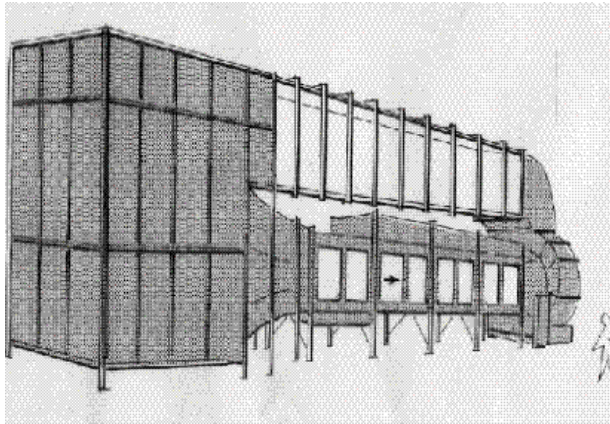


Figure 3. Wind tunnel

contraction ratio is 1 : 4.23, and the test section of the wind tunnel is 12.5 m long, 1.8 m high, and 2.7 m wide. The wind tunnel is equipped with a 220 KW fan that can produce a variation of speed between 0 – 30 m/s.

3.2. Cylinder position in the wind tunnel. The cylinder is mounted as shown in Figure 4 and it is connected to a balance positioned under the wind tunnel floor. The cylinder is mounted in the wind tunnel on a support and two dummy cylinders are connected to the wall but not to the balance to reduce the finite cylinder length effect.

This solution permits a comparison of the results with an infinitely long cylinder. The cylinder length is 120 cm (for all the 3 cases: 11 cm, 20 cm, 31 cm diameter.)

3.3. Six components balance. The balance (Carl Schenck AG) used is a six components balance capable of measuring the three forces and the three momentums around the three axes. Variations of forces and momentum are measured using strain gauges glued to the balance body.

The voltage outputs are measured by a LabVIEW based PC program.

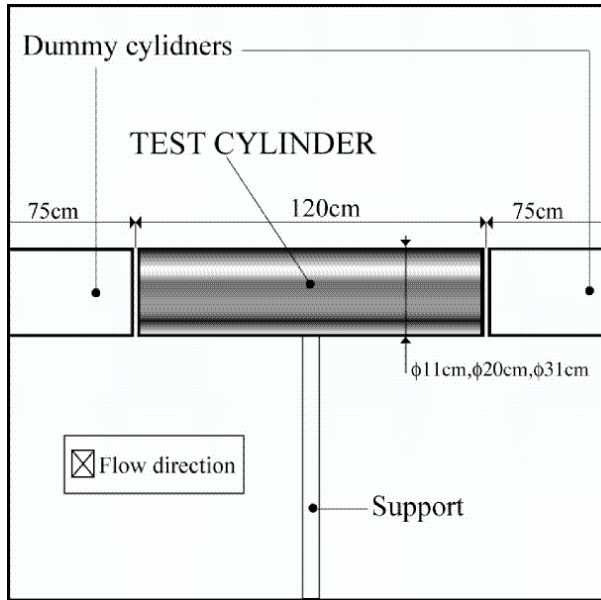


Figure 4. Cylinder in the wind tunnel

3.4. Textiles. The following chapter shows the different textiles used to change the surface roughness on the cylinders. The five textiles have all different surface roughness (Table 1).

Different roughness has been obtained by manufacturing each textile in a different way and with a different pattern. (See Table 1).

The roughness factor for each textile was found using an electronic microscope with a magnification factor of 20X. Based on structure width and depth a surface parameter can be defined as:

$$k_{surface} = \sqrt{w \cdot d} \quad (3.1)$$

Only for the black textile it has been chosen to use a different surface because of the different structure of this textile. The black textile presents in fact an inner-seam and an outer-seam. The roughness calculated is the average between inner and outer roughness.

$$k_{surfaceTOT} = \frac{k_{inner} + k_{outer}}{2} \quad (3.2)$$

Figure 5 represents five pictures of the textiles. The first three (1), (2), (3), are obtained using a magnification factor of 4X.

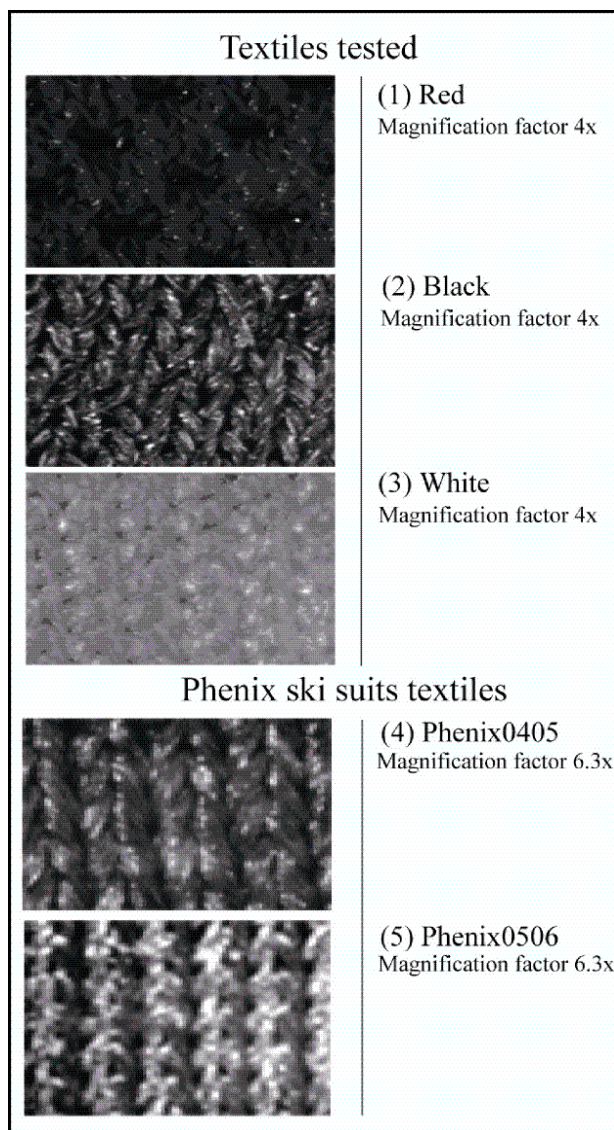


Figure 5. The five different textiles used

The red textile is the roughest and some dimples are present on the structure. The black structure presents a roughness parameter k between the red and the white textile. Some dimples are present also in the black textile structure but it is not possible to localize them in the picture shown.

Table 1. Roughness parameters of the different textiles used

		k	r
11 <i>cm</i> Red	(1)	642	$5.84E - 03$
11 <i>cm</i> Black	(2)	386	$3.51E - 03$
20 <i>cm</i> Red	(1)	642	$3.21E - 03$
20 <i>cm</i> Black	(2)	386	$1.93E - 03$
31 <i>cm</i> Red	(1)	642	$2.07E - 03$
31 <i>cm</i> Black	(2)	386	$1.25E - 03$
11 <i>cm</i> White	(3)	108	$9.82E - 04$
20 <i>cm</i> White	(3)	108	$5.40E - 04$
31 <i>cm</i> White	(3)	108	$3.48E - 04$
20 <i>cm</i> 0405	(4)	273	$1.37E - 03$
20 <i>cm</i> 0506	(5)	335	$1.68E - 03$

Figures 5(4) and 5(5) show the pictures obtained with a magnification factor of 6.3 of the two textiles used in the alpine suits.

The roughness parameter k is a surface length scale that will influence the flow close to the cylinder surface.

The surface curvature (given by the cylinder diameter) determines the pressure gradient that influences on the flow separation conditions. Then combining these two parameters in a dimensionless roughness coefficient r :

$$r = \frac{k}{Diam}. \quad (3.3)$$

4. Results

4.1. $c_d - Re$ curves. The four curves in Figure 6 represent the $c_d - Re$ curves for the 11 *cm* diameter cylinder. The transition for the black ($r = 3.51 \cdot 10^{-3}$) and the red ($r = 5.84 \cdot 10^{-3}$) textile occurs at lower Reynolds number than for the smooth cylinder and for the white ($r = 9.82 \cdot 10^{-4}$) material.

The results are in accordance with the literature: increasing the roughness, the transition to turbulence occurs at a lower Reynolds numbers which means that it is possible to reduce the drag of about 40 %. Over a certain Reynolds number range the white textile has a $c_d - Re$ curve similar to the $c_d - Re$ curve for the smooth cylinder.

Choosing the correct material for the correct speed enables a drag coefficient reduction of about 40 – 45 %.

Comparing the 20 *cm* diameter cylinder results (Figure 7) with the same graph for the 11 *cm* diameter (Figure 6) it is easy to recognize the same trend (increase roughness means shift the transition to lower Reynolds number).

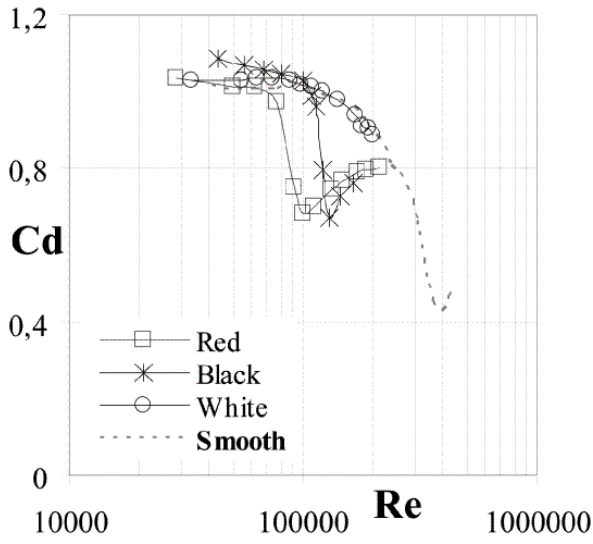


Figure 6. 11 cm cylinder

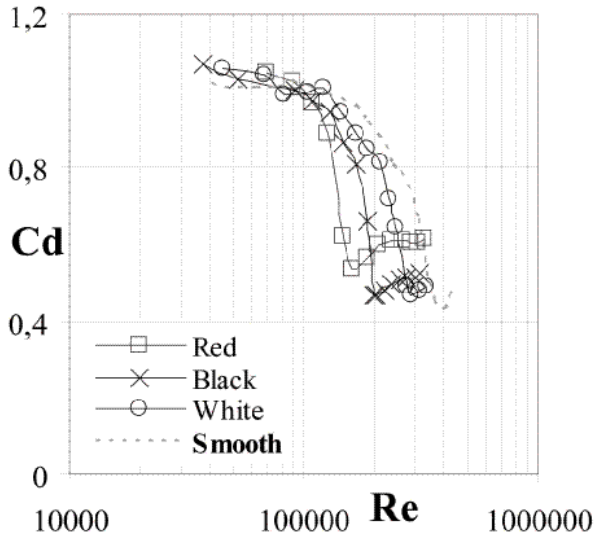


Figure 7. 20 cm cylinder

Until a certain Reynolds number ($Re = 1.75 \cdot 10^5$) the red textile ($r = 3.21 \cdot 10^{-3}$) minimizes the drag coefficient most. Between $Re = 1.85 \cdot 10^5$ and $Re = 2.7 \cdot 10^5$ the black ($r = 1.93 \cdot 10^{-3}$) and for a $Re > 2.7 \cdot 10^5$ the white textile ($r = 5.4 \cdot 10^{-4}$) produce the lowest drag coefficient.

Increasing the Reynolds number ($Re > 3.2 \cdot 10^5$), the cylinder with the red textile has a c_d higher than the c_d measured for the smooth cylinder.

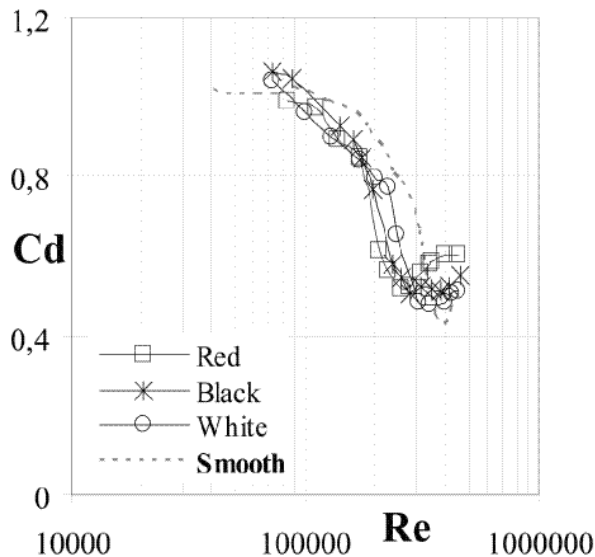


Figure 8. 31 cm cylinder

The $c_d - Re$ curves trend for the 31 cm diameter cylinder is comparable to the tendency shown in Figure 6 and Figure 7 for the 11 cm and 20 cm diameter cylinders.

For the lower Reynolds number region the cylinder dressed with the red textile ($r = 2.07 \cdot 10^{-3}$) is the one with the lowest c_d , for the middle region the black textile ($r = 1.25 \cdot 10^{-3}$) minimizes the drag coefficient and for high Reynolds number the material that minimizes the drag coefficient more than the others is the white textile ($r = 3.48 \cdot 10^{-4}$).

It is also easy to see, that now the drag coefficient reduction is about 20 – 30 % which is less than the 40 – 45 % found for the other cylinders (11 cm and 20 cm diameter).

4.2. Roughness coefficient correlation. The correlation between the roughness parameter r and the trend of the $c_d - Re$ curves has been analyzed defining a specific Reynolds number Re_{trans} .

This specific Reynolds number has been chosen to give an approximate description of where transition occurs.

Defining Re_{trans} as the Reynolds number where the c_d curve has gone through half its drop, Re_{trans} can be correlated with the roughness coefficient r (Figure 9), and the results can be expressed by the correlation

$$r = A + B \ln(Re_{trans}), \quad (4.1)$$

where the best fit for our limited data base is for $A = 0.0594$, $B = -0.0048$.

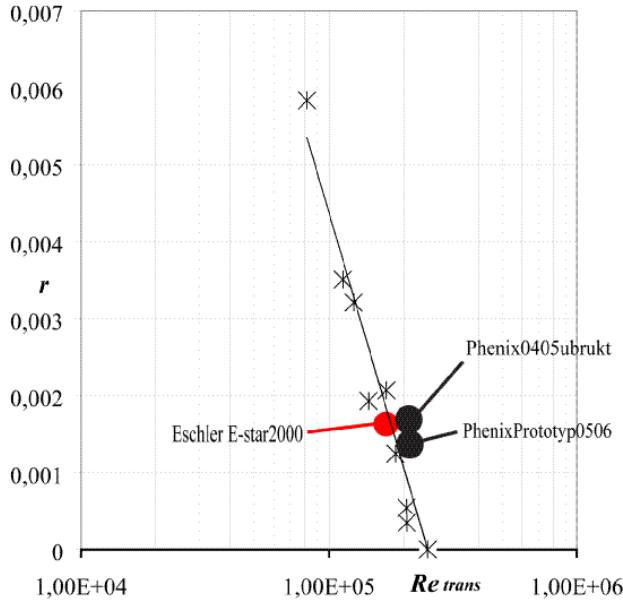


Figure 9. Correlation between r and Re_{trans} . The 3 round marks present in the figure are relatives to the data acquired for 3 textiles from 2 different ski suits used by the Norwegian national team and one from a new suit produced by Eschler

5. Conclusions

Experiments carried out on cylinders dressed with different textiles show that the introduction of surface roughness (dimples), cause the critical regime to occur at lower Reynolds numbers than for smooth cylinders. For increasing roughness, the experiments show that transition occurs at lower Reynolds numbers.

An explicit correlation between the roughness factor r and the typical Reynolds number Re_{trans} has been suggested. The results for drag reduction presented here

can be used for choosing the right textiles when designing suits for athletes, thereby reducing the athlete's aerodynamical resistance.

References

1. WHITE, F.M.: Viscous fluid flow second edition, Mc.Graw-Hill international editions, (1991), ISBN 0-07-100995-7.
2. ACHENBACH, E.: The effects of surface roughness and tunnel blockage on the flow past spheres. *Journal of fluid mechanics*, **65**(1), (1964), 113-125.
3. BEARMAN, P.W. AND HARVEY, J.K.: Control of circular cylinder flow by the use of dimples. *AIAA-Journal*, **31**(2), (1993), 1753-1756.
4. DUARTE RIBERIO, J.L.: Effects of surface roughness on the 2D flow past circular cylinders (mean forces and pressure). *Journal of wind engineering and industrial aerodynamics*, **37**, (1991), 299-309.
5. BEARMAN, P.W. AND HARVEY, J.K.: Golf ball aerodynamics. *Aeronautical Quarterly May*, **27**, (1976), 112-122.

AN UNSTEADY NUMERICAL SOLUTION OF VISCOUS COMPRESSIBLE FLOWS IN A CHANNEL FOR LOW MACH NUMBERS

PETRA PUNČOCHÁŘOVÁ *, KAREL KOZEL **, JAROMÍR HORÁČEK **,
JIŘÍ FÜRST *

* Czech Technical University in Prague

Karlovo náměstí 13, 121 35, Prague 2, Czech Republic

** Institute of Thermomechanics, Czech Academy of Sciences

Dolejškova 5, Prague 8, Czech Republic

puncocha@marian.fsik.cvut.cz

[Received: January 15, 2007]

Abstract. The work deals with numerical solution of unsteady flow with low Mach numbers in a two-dimensional channel. The flow is described by the unsteady Navier-Stokes equations (laminar) for the compressible fluid. The unsteady flow is caused by a prescribed time periodical motion of a part of the channel wall, which is changing the shape. The numerical solution is realized by finite volume method and the explicit predictor-corrector MacCormack scheme with Jameson artificial viscosity using a grid of quadrilateral cells. The moved grid of quadrilateral cells is considered in the form of conservation laws using Arbitrary Lagrangian-Eulerian method. Some numerical results of the unsteady flows in the symmetric channel are presented for inlet Mach number $M_\infty = 0.02$, Reynolds number $Re \approx 10^3$ and for frequency of the wall motion 20 Hz. The numerical results were obtained using special software developed by the authors.

Keywords: CFD, FVM, low Mach number, compressible unsteady flow, ALE method, MacCormack numerical scheme

1. Introduction

The work presents a numerical method solving two-dimensional unsteady compressible viscous flow with low Mach numbers in a symmetric channel. The unsteady flow is caused by a prescribed time periodic motion of a part of the channel wall. The flow in the channel can represent a very simple model of airflow coming from the trachea, through the glottis to the human vocal tract.

In reality, the airflow coming from the human lungs causes the vocal folds self-oscillations, and the glottis is completely closing in normal phonation regimes generating acoustic pressure fluctuations. In our case, we prescribe a narrow channel harmonic opening and nearly closing the cross-section. The frequency of periodic oscillations of the vocal folds is in most cases higher than 100 Hz. Here, we present

the results with frequency of oscillations 20 Hz. The voice source signal is travelling from the glottis to the mouth, exciting the acoustic supraglottal spaces and modified by acoustic resonance properties of the vocal tract [1]. Considering a normal speech the airflow velocity in trachea is approximately in the range 5 – 16 m/s. Here, we impose uniform inflow Mach number $M_\infty = 0.02$, i.e., the airflow velocity 6.68 m/s.

At present, the flow models in the glottis are mostly based on the Bernoulli equation [1] or 1D models for the incompressible inviscid fluid [2]. Acoustic wave propagation in the vocal tract is usually modelled separately using linear acoustic perturbation theory, the wave equation for the potential flow [3]. Problematic question is also how to model the flow separation point on moving surface in a small gap. This is usually approximated by some quasi-steady formulas which are deduced from steady flow solution in divergent channels [4], and the validity of this hypothesis for higher frequencies is questionable. The airflow in the glottis which is described by 2D Navier-Stokes equations for the incompressible laminar flow was studied in [5] using Finite Volume Method (FVM) and in [6] using Finite Element Method (FEM). Software FIDAP was used in [7] for 3D modelling of the flow in glottis by FEM using the Navier-Stokes equations for the incompressible fluid.

When the glottis is closing the airflow velocity is becoming much higher in the narrowest part of the airways, where also the viscous forces are important. For the inviscid incompressible flow the maximum flow velocity would tend to infinity just before glottis closure. Therefore for a correct modelling of a real flow in the glottis, the compressible, viscous, unsteady model should be considered. Even if no complete closure of the glottis is modelled, the mathematical model presented for the numerical simulation of the airflow field in the glottis is complex and relatively closer to reality.

The numerical results shown in Section 4 were obtained by numerical method shown in Section 3 and by developed software based on C/C++, on the basis of the FVM for compressible viscous flow in a narrow channel harmonically opening and nearly closing the cross-section in space and time domains.

2. Mathematical model

The 2D system of Navier-Stokes equations was used as a mathematical model to describe the unsteady laminar flow of compressible viscous fluid in a channel. The Navier-Stokes equations are transformed to non-dimensional variables. The transformation of dimensional variables (marked with the accent hat) to the non-dimensional variables is defined as follows:

$$\begin{aligned} \rho &\rightarrow \hat{\rho}/\hat{\rho}_\infty, & (u, v) &\rightarrow (\hat{u}, \hat{v})/\hat{c}_\infty, & (x, y) &\rightarrow (\hat{x}, \hat{y})/\hat{L}_s, & t &\rightarrow \hat{t} \cdot \hat{c}_\infty/\hat{L}_s, \\ p &\rightarrow \hat{p}/(\hat{\rho}_\infty \cdot \hat{c}_\infty^2), & e &\rightarrow \hat{e}/(\hat{\rho}_\infty \cdot \hat{c}_\infty^2), & \eta &\rightarrow \hat{\eta}/\hat{\eta}_\infty, & T &\rightarrow \hat{T}/\hat{T}_\infty, \end{aligned} \quad (2.1)$$

where ρ denotes the density, u and v are the components of velocity vector, p denotes static pressure and e is total energy per unit volume. The reference variables in this case are inflow variables (marked with the infinite subscript): the speed of sound $\hat{c}_\infty = 334$ m/s, the density $\hat{\rho}_\infty = 1.225$ kg/m³, the temperature $\hat{T}_\infty = 293.15$ K, the dynamic viscosity $\hat{\eta}_\infty = 15 \cdot 10^{-6}$ Pa · s and a selected length $\hat{L}_s = 0.02$ m. The

system of Navier-Stokes equations is expressed in the non-dimensional conservative form as:

$$\frac{\partial \mathbf{W}}{\partial t} + \frac{\partial \mathbf{F}}{\partial x} + \frac{\partial \mathbf{G}}{\partial y} = \frac{1}{Re} \left(\frac{\partial \mathbf{R}}{\partial x} + \frac{\partial \mathbf{S}}{\partial y} \right), \quad (2.2)$$

where

$$\mathbf{W} = [\rho, \rho u, \rho v, e]^T, \quad (2.3)$$

$$\mathbf{F} = [\rho u, \rho u^2 + p, \rho uv, (e + p)u]^T, \quad (2.4)$$

$$\mathbf{G} = [\rho v, \rho uv, \rho v^2 + p, (e + p)v]^T, \quad (2.5)$$

$$\mathbf{R} = \begin{pmatrix} 0 \\ \frac{2}{3}\eta \left(2\frac{\partial u}{\partial x} - \frac{\partial v}{\partial y} \right) \\ \eta \left(\frac{\partial u}{\partial y} + \frac{\partial v}{\partial x} \right) \\ \frac{2}{3}\eta \left(2\frac{\partial u}{\partial x} - \frac{\partial v}{\partial y} \right) u + \eta \left(\frac{\partial u}{\partial y} + \frac{\partial v}{\partial x} \right) v + k\frac{\partial T}{\partial x} \end{pmatrix}, \quad (2.6)$$

$$\mathbf{S} = \begin{pmatrix} 0 \\ \eta \left(\frac{\partial u}{\partial y} + \frac{\partial v}{\partial x} \right) \\ \frac{2}{3}\eta \left(-\frac{\partial u}{\partial x} + 2\frac{\partial v}{\partial y} \right) \\ \eta \left(\frac{\partial u}{\partial y} + \frac{\partial v}{\partial x} \right) u + \frac{2}{3}\eta \left(-\frac{\partial u}{\partial x} + 2\frac{\partial v}{\partial y} \right) v + k\frac{\partial T}{\partial y} \end{pmatrix}, \quad (2.7)$$

\mathbf{W} is the vector of conservative variables, \mathbf{F} and \mathbf{G} are the vectors of inviscid fluxes, \mathbf{R} and \mathbf{S} are the vectors of viscous fluxes. The static pressure p is expressed by the equation of state:

$$p = (\kappa - 1) \left[e - \frac{1}{2}\rho (u^2 + v^2) \right]. \quad (2.8)$$

Reynolds number $Re = \hat{\rho}_\infty \hat{u}_\infty \hat{H} / \hat{\eta}_\infty$ is computed from inflow variables, where $\hat{H} = 2h\hat{L}_s$ is the inflow width of the channel (see Fig. 1). The non-dimensional dynamic viscosity found in the dissipative terms of the equations is the function of temperature: $\eta = (T/T_\infty)^{3/4}$. The heat transfer coefficient is expressed as $k = \eta\kappa/[Pr(\kappa-1)]$, where $Pr = 0.7$ is Prandtl number and $\kappa = 1.4$ is Poisson parameter.

2.1. Mathematical formulation. For the numerical solution the domain D and boundary conditions have to be defined.

Figure 1 shows the domain D which represents the symmetric channel. The computational domain is only the lower half of the channel. The upper boundary represents the axis of symmetry. The lower boundary represents the wall and the part of the

channel wall between the points A , B is changing the shape as given function of time and axial coordinate:

$$\begin{aligned} w(x, t) &= \frac{1}{2} (a_1 + a_t) \cdot \left\{ \sin \left[\frac{\pi}{C-A} \left(x - \frac{A+C}{2} \right) \right] + 1 \right\} + d, & x \in \langle A, C \rangle, \\ w(x, t) &= \frac{1}{2} (a_1 + a_t + d) \cdot \left[\cos \left(\pi \frac{x-C}{B-C} \right) + 1 \right], & x \in \langle C, B \rangle, \\ a_t &= a_2 \cdot \sin(2\pi f \cdot t), & t \in \langle 0, 2\pi \rangle, \end{aligned} \quad (2.9)$$

where $A = [1.75; 0.4]$, $B = [2.65; 0]$, $C = [2.3; w(x = 2.3, t)]$ and the channel geometry has the following non-dimensional parameters: $L = 8$, $h = 0.4$, $d = 0.4$. The frequency of oscillations is computed as $f = 1/(\hat{t}_0 \cdot \frac{\hat{c}_\infty}{L_s})$, where $\hat{t}_0 = 0.05$ s is the period of oscillations. Then a gap, which is the glottal half-width, can be computed in the following way (see Fig. 1): $g(x = 2.3, t) = (d + h) - w(x = 2.3, t)$.

In the work the results for two sizes of the glottal half-widths are presented. The wide glottis has the amplitudes of oscillation (2.9) adjusted to $a_1 = 0.2$, $a_2 = 0.08$ and this case is called *Wide Gap*. The minimum and maximum of the gap for the *Wide Gap* is: $g_{min} = 0.12$, $g_{max} = 0.28$. In the second case, which is called *Narrow Gap*, the amplitudes of oscillation are adjusted to $a_1 = 0.3$, $a_2 = 0.08$ and $g_{min} = 0.02$, $g_{max} = 0.18$.

The boundary conditions for the viscous fluid flow has been considered in the following form:

- a) Upstream conditions: 3 values of \mathbf{W} are given (ρ , ρu , ρv) and the pressure is extrapolated from the domain to the inlet of the channel, it means $\partial p / \partial \mathbf{n} = 0$ where \mathbf{n} is the outer normal vector to the surface ∂D .
- b) Downstream conditions: the pressure p_2 is given and $\partial(\rho, \rho u, \rho v) / \partial \mathbf{n} = 0$.
- c) On the wall the normal derivative of the temperature $\partial T / \partial \mathbf{n} = 0$ and the velocity vector $(u, v)|_{wall} = (0, \bar{v}_{wall})$ are considered. Variable \bar{v}_{wall} is y -velocity component of the lower wall.
- d) At the axis of symmetry the condition $(u, v) \cdot \mathbf{n} = 0$ is required.

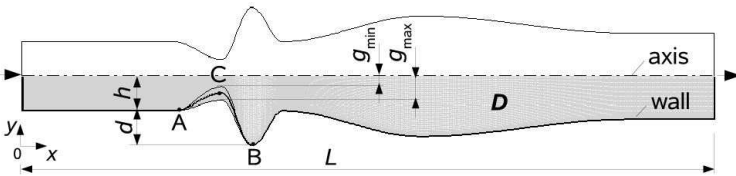


Figure 1. The computational domain D (The symmetric channel)

The shape of this scale model is inspired by the shape of the vocal tract [8]. For the numerical prediction of flow in the vocal tract we used simplifying assumption that during the normal phonation the vocal folds oscillations are symmetric [8] hence the symmetric geometry is used.

3. Numerical solution

The numerical solution of two-dimensional problems uses FVM in cell centred form on the grid of quadrilateral cells.

The bounded domain D is divided into mutually disjoint sub-domains $D_{i,j}$ (e.g. the quadrilateral cells). The equations (2.2) are integrated over the sub-domains $D_{i,j}$ and using Green formula the following relation is valid:

$$\int_{D_{i,j}} \frac{\partial \mathbf{W}}{\partial t} dx dy = - \left[\oint_{\partial D_{i,j}} (\mathbf{F} dy - \mathbf{G} dx) - \oint_{\partial D_{i,j}} (\mathbf{R} dy - \mathbf{S} dx) \right]. \quad (3.1)$$

When the domain is steady the equation (3.1) can be rewritten using Mean value theorem to the integral form of FVM:

$$\left. \frac{\partial W}{\partial t} \right|_{i,j} = \frac{-1}{\mu_{i,j}} \left[\oint_{\partial D_{i,j}} (\mathbf{F} dy - \mathbf{G} dx) - \oint_{\partial D_{i,j}} (\mathbf{R} dy - \mathbf{S} dx) \right], \quad (3.2)$$

where $\mu_{i,j} = \int \int_{D_{i,j}} dx dy$ is volume of cell $D_{i,j}$. The difference form of FVM is:

$$\frac{\mathbf{W}_{i,j}^{n+1} - \mathbf{W}_{i,j}^n}{\Delta t} = \frac{-1}{\mu_{i,j}} \sum_k \left[\left(\tilde{\mathbf{F}}_k - \tilde{\mathbf{R}}_k \right) \Delta y_k - \left(\tilde{\mathbf{G}}_k - \tilde{\mathbf{S}}_k \right) \Delta x_k \right], \quad (3.3)$$

where $\Delta t = t^{n+1} - t^n$ is time step. The physical fluxes $\mathbf{F}, \mathbf{G}, \mathbf{R}, \mathbf{S}$ on an edge k of cell $D_{i,j}$ are replaced by the numerical fluxes (marked with tilde) $\tilde{\mathbf{F}}, \tilde{\mathbf{G}}, \tilde{\mathbf{R}}, \tilde{\mathbf{S}}$ which are approximations of the physical fluxes. The approximations of the numerical fluxes and the time derivative depend on the chosen numerical scheme.

If the domain is unsteady, the integral form of FVM is derived using the Arbitrary Lagrangian-Eulerian (ALE) formulation which defines homeomorphic mapping of reference domain D_0 at initial time to a domain D_t at time t [9]. Then the equation (3.1) can be written as:

$$\int_{D_{i,j}|_{t=0}} \left. \frac{\partial(|J|\mathbf{W})}{\partial t} \right|_{\mathbf{X}_0} d\mathbf{X}_0 = - \left\{ \oint_{D_{i,j}|_t} (\mathbf{F} - \mathbf{W} \cdot s_1) dy - \right. \\ \left. - (\mathbf{G} - \mathbf{W} \cdot s_2) dx \right\} - \oint_{D_{i,j}|_t} [\mathbf{R} dy - \mathbf{S} dx]. \quad (3.4)$$

$|J|$ denotes determinant of the Jacobi matrix of the ALE mapping and $\mathbf{X}_0 \in D_0$ is point of reference configuration. In the first integral on the right side fluxes $(-\mathbf{W} \cdot s_i)$ induced by the movement of the boundary of the control volume appear when ALE method is used. Vector (s_1, s_2) stands for the domain velocity. Hence, the differential form of FVM for unsteady domain is:

$$\frac{\mathbf{w}_{i,j}^{n+1} \cdot \mu_{i,j}^{n+1} - \mathbf{w}_{i,j}^n \cdot \mu_{i,j}^n}{\Delta t} = - \sum \left[\left(\tilde{\mathbf{F}}_k - s_{1k} \mathbf{W}_k - \tilde{\mathbf{R}}_k \right) \Delta y_k - \right. \\ \left. - \left(\tilde{\mathbf{G}}_k - s_{2k} \mathbf{W}_k - \tilde{\mathbf{S}}_k \right) \Delta x_k \right]. \quad (3.5)$$

3.1. Numerical scheme. For the numerical solution of the system (2.2) the explicit MacCormack (MC) scheme in the predictor-corrector form is used. The scheme is of the 2^{nd} order of accuracy in time and space:

$$\begin{aligned}
 \mathbf{W}_{i,j}^{n+1/2} &= \frac{\mu_{i,j}^n}{\mu_{i,j}^{n+1}} \mathbf{W}_{i,j}^n - \frac{\Delta t}{\mu_{i,j}^{n+1}} \sum_{k=1}^4 \left[\left(\tilde{\mathbf{F}}_k^n - s_{1k} \mathbf{W}_k^n - \tilde{\mathbf{R}}_k^n \right) \Delta y_k - \right. \\
 &\quad \left. \left(\tilde{\mathbf{G}}_k^n - s_{2k} \mathbf{W}_k^n - \tilde{\mathbf{S}}_k^n \right) \Delta x_k \right], \\
 \overline{\mathbf{W}}_{i,j}^{n+1} &= \frac{\mu_{i,j}^n}{\mu_{i,j}^{n+1}} \frac{1}{2} \left(\mathbf{W}_{i,j}^n + \mathbf{W}_{i,j}^{n+1/2} \right) - \\
 &\quad - \frac{\Delta t}{2\mu_{i,j}^{n+1}} \sum_{k=1}^4 \left[\left(\tilde{\mathbf{F}}_k^{n+1/2} - s_{1k} \mathbf{W}_k^{n+1/2} - \tilde{\mathbf{R}}_k^{n+1/2} \right) \Delta y_k - \right. \\
 &\quad \left. \left(\tilde{\mathbf{G}}_k^{n+1/2} - s_{2k} \mathbf{W}_k^{n+1/2} - \tilde{\mathbf{S}}_k^{n+1/2} \right) \Delta x_k \right].
 \end{aligned} \tag{3.6}$$

Equation (3.6) represents the MC scheme for the viscous flow in the domain with moving grid of quadrilateral cells. The approximations of the convective terms and the dissipative terms are central and the vector $(s_1, s_2)_k$ represents the speed of edge k (see Fig. 2). The partial derivatives of the velocity and the temperature are approximated using dual volumes V'_k (see [10]) as shown in Figure 2. The partial derivatives of a variable ϕ on the edge k are computed using following relations:

$$\left. \frac{\partial \phi}{\partial x} \right|_k = \frac{1}{V'_k} \sum_{l=1}^4 \phi_l \Delta y_l, \quad \left. \frac{\partial \phi}{\partial y} \right|_k = -\frac{1}{V'_k} \sum_{l=1}^4 \phi_l \Delta x_l. \tag{3.7}$$

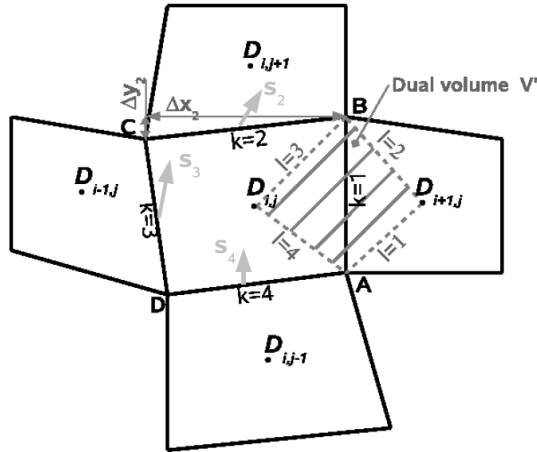


Figure 2. The finite volume $D_{i,j}$, the dual volume V'_k

The inviscid numerical fluxes are approximated by the physical inviscid fluxes as follows:

$$\begin{aligned}
\tilde{\mathbf{F}}_1^n &= \mathbf{F}_{i,j}^n, \quad \tilde{\mathbf{F}}_2^n = \mathbf{F}_{i,j}^n, \quad \tilde{\mathbf{F}}_3^n = \mathbf{F}_{i-1,j}^n, \quad \tilde{\mathbf{F}}_4^n = \mathbf{F}_{i,j-1}^n, \\
\tilde{\mathbf{G}}_1^n &= \mathbf{G}_{i,j}^n, \quad \tilde{\mathbf{G}}_2^n = \mathbf{G}_{i,j}^n, \quad \tilde{\mathbf{G}}_3^n = \mathbf{G}_{i-1,j}^n, \quad \tilde{\mathbf{G}}_4^n = \mathbf{G}_{i,j-1}^n, \\
\text{the corrector step:} \\
\tilde{\mathbf{F}}_1^{n+1/2} &= \mathbf{F}_{i+1,j}^{n+1/2}, \quad \tilde{\mathbf{F}}_2^{n+1/2} = \mathbf{F}_{i,j+1}^{n+1/2}, \\
\tilde{\mathbf{F}}_3^{n+1/2} &= \mathbf{F}_{i,j}^{n+1/2}, \quad \tilde{\mathbf{F}}_4^{n+1/2} = \mathbf{F}_{i,j}^{n+1/2}, \\
\tilde{\mathbf{G}}_1^{n+1/2} &= \mathbf{G}_{i+1,j}^{n+1/2}, \quad \tilde{\mathbf{G}}_2^{n+1/2} = \mathbf{G}_{i,j+1}^{n+1/2}, \\
\tilde{\mathbf{G}}_3^{n+1/2} &= \mathbf{G}_{i,j}^{n+1/2}, \quad \tilde{\mathbf{G}}_4^{n+1/2} = \mathbf{G}_{i,j}^{n+1/2}.
\end{aligned} \tag{3.8}$$

The last term used in MC scheme is the Jameson's artificial dissipation $AD(W_{i,j})^n$ [11]:

$$\begin{aligned}
AD(W_{i,j})^n &= C_1 \gamma_1 (\mathbf{W}_{i+1,j}^n - 2\mathbf{W}_{i,j}^n + \mathbf{W}_{i-1,j}^n) + \\
&+ C_2 \gamma_2 (\mathbf{W}_{i,j+1}^n - 2\mathbf{W}_{i,j}^n + \mathbf{W}_{i,j-1}^n),
\end{aligned} \tag{3.9}$$

$C_1, C_2 \in R$ are constants, in our case $C_1 = 1.7$, $C_2 = 1.5$. Normed pressure gradients γ_1, γ_2 have the form:

$$\gamma_1 = \frac{|p_{i+1,j}^n - 2p_{i,j}^n + p_{i-1,j}^n|}{|p_{i+1,j}^n| + 2|p_{i,j}^n| + |p_{i-1,j}^n|}, \quad \gamma_2 = \frac{|p_{i,j+1}^n - 2p_{i,j}^n + p_{i,j-1}^n|}{|p_{i,j+1}^n| + 2|p_{i,j}^n| + |p_{i,j-1}^n|}. \tag{3.10}$$

The use of artificial dissipation is common way to stabilise the numerical scheme with the higher order of accuracy. The term of artificial dissipation has of the third order of accuracy then the second order of accuracy of the original scheme is valid. Then the vector of conservative variables \mathbf{W} can be computed at a new time level t^{n+1} :

$$\mathbf{W}_{i,j}^{n+1} = \overline{\mathbf{W}}_{i,j}^{n+1} + AD(W_{i,j})^n. \tag{3.11}$$

The stability condition of the scheme (on the regular orthogonal grid) limits the time step:

$$\Delta t \leq CFL \left[\frac{|u_{max}| + c}{\Delta x_{min}} + \frac{|v_{max}| + c}{\Delta y_{min}} + \frac{2}{Re} \left(\frac{1}{\Delta x_{min}^2} + \frac{1}{\Delta y_{min}^2} \right) \right]^{-1}, \tag{3.12}$$

c denotes the local speed of sound, u_{max} and v_{max} are the maximum velocity in the domain, $CFL < 1$ for the non-linear equations. The minimum cell size in y -direction is $\Delta y_{min} \approx 1/\sqrt{Re}$ to resolve capture boundary layer effects (see Fig. 3). The time step in our case mainly depends on $\Delta y_{min} \in (10^{-3}, 2.5 \cdot 10^{-3})$ and the time step during the unsteady problem computation is about $\Delta t \doteq 3 \cdot 10^{-4}$.

4. Numerical results

The numerical methods have been suggested and developed at CTU in Prague, Department of Technical Mathematics since 1978. For the Euler and Navier-Stokes

equations (compressible and incompressible) methods based on classical schemes as well as modern finite volume schemes (TVD, WENO, AUSM, Residual Distribution Scheme etc.) have been developed. We tested these methods for laminar and turbulent flows using different type of schemes and grids (structured and unstructured). Also, comparison with experimental results and with other numerical results has been published. The method presented here is also one of long time developed and tested method including ALE method (see [12]–[19]).

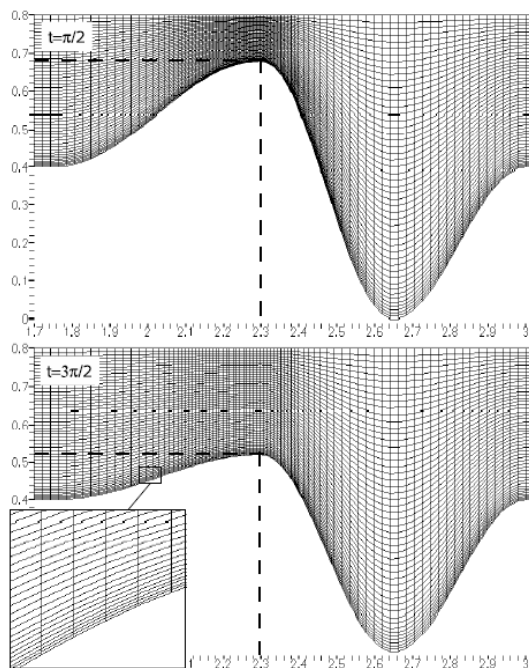


Figure 3. Computational grid in two different time levels (at minimum and maximum of the gap (*Wide Gap*)) and the detail of the grid refinement near the wall

The method has been tested using structured grid, refinement of the grid (coarse, fine, very fine) and also very fine grid near walls. The flow has been investigated in three types of the channel: in the channel with the upper straight wall and the lower sinus bump time depend wall using the Euler and Navier-Stokes equations [20], in the divergent axis symmetry channel using the Navier-Stokes equations and in the present type of the channel [21], [22].

For the numerical solution, the domain D (see Fig. 1) is covered by the structured grid of quadrilateral cells. Figure 3 shows the grid in part of the channel at two time levels (at minimum and maximum of the gap (*Wide Gap*)). In the detail, the

refinement cells near the wall is shown. The computational domain contains 400×50 cells.

The computation of the unsteady solution was carried out in two stages. First, the computation of the steady solution was realized (see Fig. 4(a)). This steady solution was then used as an initial condition for computation of the unsteady problem, when the unsteady boundary conditions (2.9) are imposed.

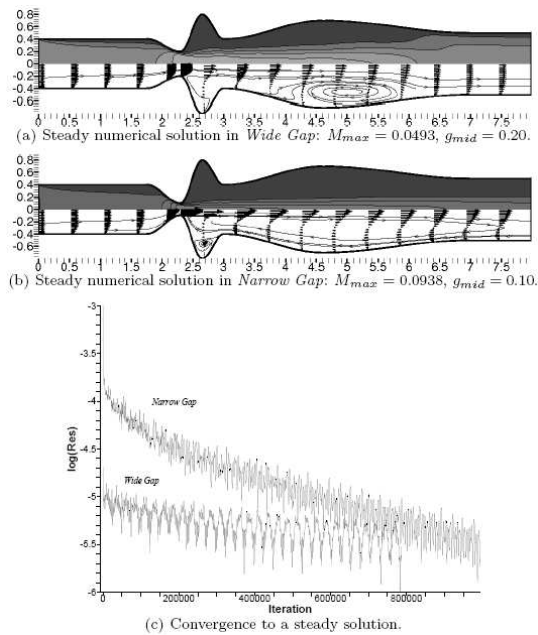


Figure 4. The steady numerical solutions of the viscous compressible (laminar) flow in the symmetric channel. $M_\infty = 0.02$, $p_2 = 1/\kappa$, $Re = 8700$, mesh of 400×50 cells

4.1. Steady problem. Figure 4 shows the steady numerical solutions for the viscous laminar flow in the domain D (see Fig. 1) with a rigid wall. The gaps are fixed in middle position, for the *Wide Gap* $g_{mid} = 0.20$ and for the *Narrow Gap* $g_{mid} = 0.10$. In both cases the inlet Mach number $M_\infty = 0.02$, the pressure at the outlet $p_2 = 1/\kappa$ and Reynolds number $Re = 8700$. The results are mapped by Mach number iso-lines (upper part of the symmetric channel) and by stream-traces and velocity vectors (lower part of the symmetric channel).

Figure 4(a) shows the steady numerical solution for the *Wide Gap*. The maximum computed value of Mach number in the domain is $M_{max} = 0.0493$ at the point $x = 2.343$ at the channel axis ($y = 0.8$). Figure 4(b) shows the steady numerical solution for the *Narrow Gap*. The maximum Mach number in the domain is $M_{max} = 0.0938$

at the point $x = 2.324$ at the channel axis. Figure 4(c) shows convergence to the steady state solution computed using the L_2 norm of momentum residuals (ρu). The convergence seems to be satisfactory for this very sensitive and complicated cases.

4.2. Unsteady problem. Figures 5 and 6 show the unsteady numerical solutions of the flow field development of the viscous compressible (laminar) flows in the symmetric channel. The results are mapped by Mach number iso-lines (upper part) and by stream-traces and velocity vectors (lower part). In both cases, the inlet Mach number

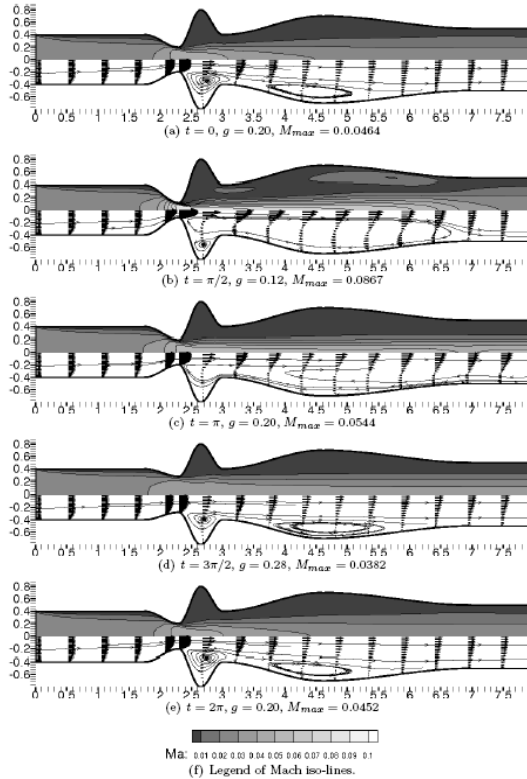


Figure 5. The unsteady numerical solution for the *Wide Gap*. $g_{max} = 0.28$, $g_{min} = 0.12$, $M_\infty = 0.02$, $p_2 = 1/\kappa$, $Re = 8700$, $\hat{f} = 20 Hz$, mesh of 400×50 cells

$M_\infty = 0.02$, the frequency of oscillations of the wall between the points A, B (see Fig. 1) $\hat{f} = 20 Hz$, the pressure $p_2 = 1/\kappa$ and $Re = 8700$ are set. The numerical results are shown in the third period of oscillations for the *Wide Gap* and in the second period of oscillations for the *Narrow Gap* at several time layers. Figure 5 shows the numerical solution for the *Wide Gap*. The maximum computed value of Mach number is $M_{max} = 0.0867$ at the point $x = 2.341$ at the channel axis in time

$t = \pi/2$ (see Figs. 5(b) and 9(b)). Figure 6 shows the numerical solution for the *Narrow Gap*. In this case, the highest Mach number was not achieved when the minimum gap was reached as in previous case, but after the glottal-width began to open. The maximum computed value of Mach number is $M_{max} = 0.5174$ at the point $x = 2.325$ at the channel axis in time $t = 27/50 \pi$ (see Fig. 10(b)).

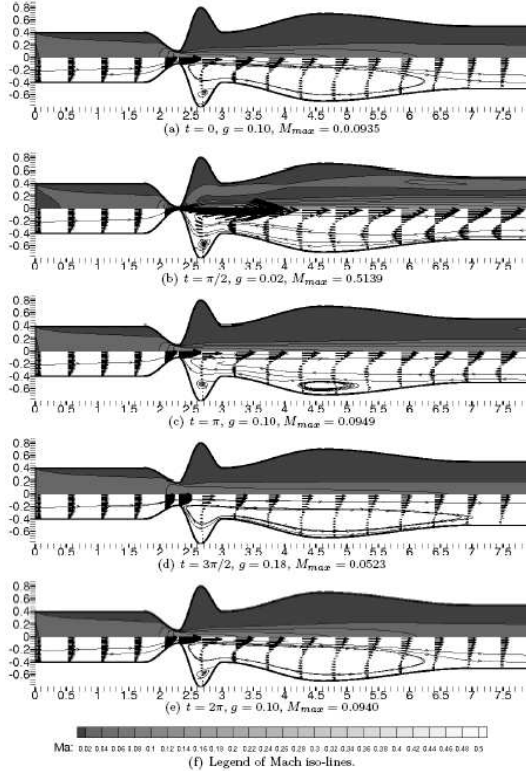


Figure 6. The unsteady numerical solution for the *Narrow Gap*. $g_{max} = 0.18, g_{min} = 0.02, M_{\infty} = 0.02, p_2 = 1/\kappa, Re = 8700, \hat{f} = 20 Hz$, mesh of 400×50 cells

In the Figures 7 and 8 the movement of the lower wall $w(x = 2.3, t)$, the pressure and Mach number computed in the narrowest cross-section of the channel at the point $x = 2.3$ at the axis of symmetry in real time domain are shown. Figure 7 shows results of numerical solution for the *Wide Gap*. It can be seen that after a transition time of about $0.06 s$ (in the second period of oscillations) the flow becomes almost periodic. Due to a relatively low frequency of oscillations and wide minimal gap the phase shift between the motion of the wall and the pressure fluctuations is small. Figure 8 shows results of numerical solution for the *Narrow Gap*. The phase shift between the motion of the wall and the pressure fluctuations is about $0.002 s$.

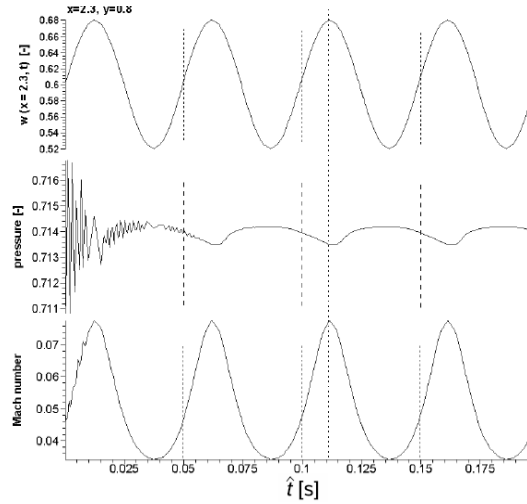


Figure 7. *Wide Gap*. The function of the channel lower wall $w(x = 2.3, t)$, the pressure and Mach number computed at the axis of symmetry ($y = 0.8$), at $x = 2.3$, in real time

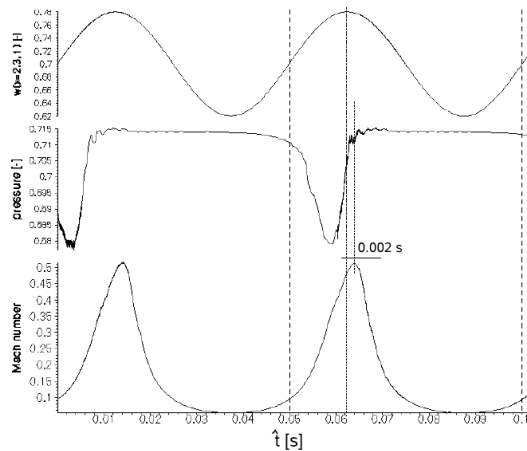
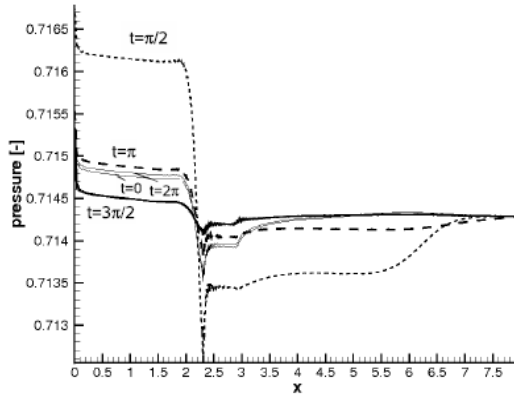


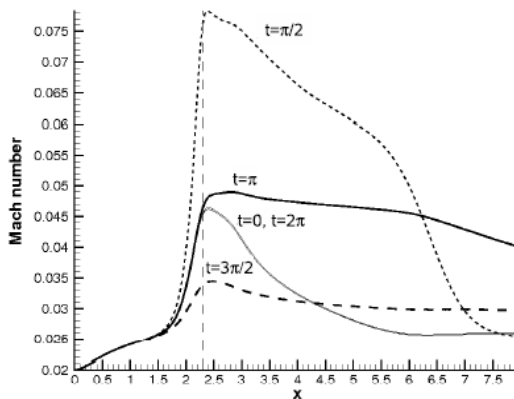
Figure 8. *Narrow Gap*. The function of the channel lower wall $w(x = 2.3, t)$, the pressure and Mach number computed at the axis of symmetry ($y = 0.8$), at $x = 2.3$, in real time

Figures 9 and 10 show the pressure on the wall and the Mach number at the axis of symmetry along the channel at several time levels during one oscillation period. Figure 9 shows results of numerical solution for the *Wide Gap*. The minimum of pressure and the maximum of Mach number is behind the narrowest cross-section of

the channel ($x = 2.3$). The highest Mach number appears in the time $t = \pi/2$ when the gap is minimal (i.e. $w(x, t)$ is maximal, see the third period in Fig. 7). Figure 10 shows results of numerical solution for the *Narrow Gap*. In this case the highest Mach number appears after the narrowest cross-section exceeds the minimum of gap (g_{min}), during opening of the glottis, in the time $t = 27/50\pi$.



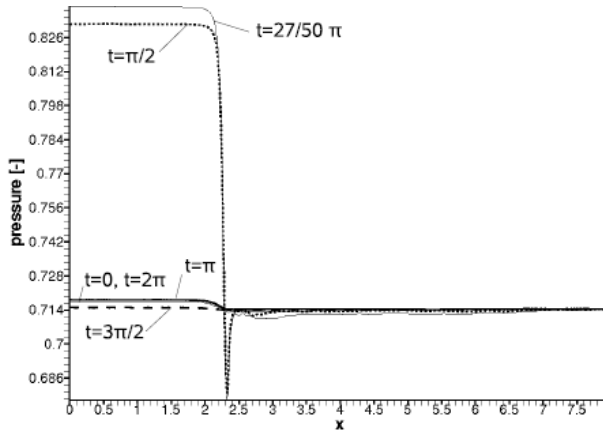
(a) The pressure on the lower wall.



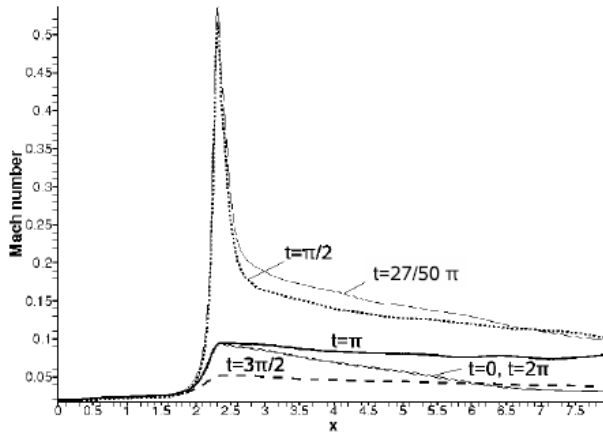
(b) The Mach number at the axis of symmetry.

Figure 9. *Wide Gap*. The pressure on the wall and the Mach number at the axis of symmetry along x at several time levels during one oscillation period

Figure 11 shows the detail of numerical solution for the *Wide Gap* at the point of the flow separation in the time $t = \pi/2$. The point of the flow separation is behind the narrowest cross-section ($x = 2.3$) at about $x_s = 2.33$. The flow separation in very narrow channel is predicted to occur at the point where the glottal-width ($2g$) exceeds



(a) The pressure on the lower wall.



(b) The Mach number at the axis of symmetry.

Figure 10. *Narrow Gap*. The pressure on the wall and the Mach number at the axis of symmetry along x at several time levels during one oscillation period

the minimum glottal-width ($2g_{min}$) by 10 – 20 % [23]. In this case, the distance of the point separation from the narrowest cross-section is 0.03 and it is 12.5 % of the minimum glottal-width ($2g_{min} = 0.24$). Figure 12 shows the detail of numerical solution for the *Narrow Gap* at the point of the flow separation in the time $t = \pi/2$. The distance of the point separation from the narrowest cross-section is 0.016 and it is 40.0 % of the minimum glottal-width ($2g_{min} = 0.04$) and thus the quasi-steady rule used in [23] is not generally valid. To locate the point separation in this case, the fine grid around point separation is necessary ($\Delta x < 0.001$).

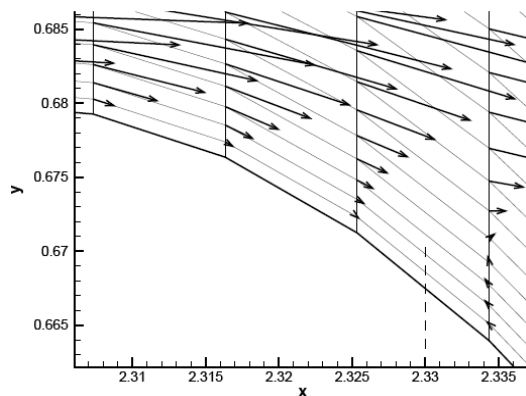


Figure 11. *Wide Gap*. The detail of the velocity vectors at the point of the flow separation in time $t = \pi/2$ ($g = g_{min} = 0.12$)

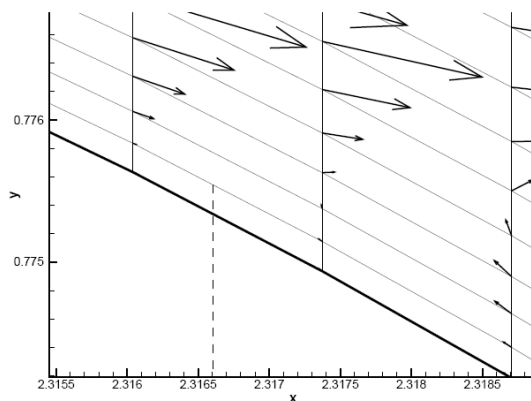


Figure 12. *Narrow Gap*. The detail of the velocity vectors at the point of the flow separation in time $t = \pi/2$ ($g = g_{min} = 0.02$)

5. Summary

The numerical method and the special programme code solving the two-dimensional unsteady Navier-Stokes equations for the viscous compressible fluid has been developed. The method is successively working for higher Mach numbers (transonic flow) as well as for very low Mach numbers. In the article this method has been used for the numerical solution of the airflow in a simplified model of the human vocal tract geometry. The method has been used for two different cases with the similar geometry, with the same inlet Mach number M_∞ and frequency of oscillations but with different widths of narrow part of the channel (*Wide Gap*, *Narrow Gap*). The method can successfully be used in other engineering applications for the steady as

well as for the unsteady numerical solution of flows with low Mach numbers, e.g. in studies of other leakage flow-induced vibration problems.

Future tests of the method for applications in modelling of the flow in the human vocal tract will be focused on the higher frequency of oscillations ($\hat{f} \approx 100 \text{ Hz}$), the lower inflow Mach number ($M_\infty \leq 0.015$) and on narrower glottal-width ($2g_{min} \leq 0.04$). Also the geometry of the channel will be closer to the real geometry of the glottis and vocal tract.

Acknowledgement. This contribution was partially supported by Research Plan MSM 6840770010 and the projects of GA CR No. 208/08/0012 and GA AS CR No. IAA 200760613.

References

1. TITZE, I.R.: *Principles of Voice Production*. National Centre for Voice and Speech, Iowa City, 2000, ISBN 0-87414-122-2.
2. HORÁČEK, J., ŠIDLÓF, P., AND ŠVEC, J.G.: Numerical simulation of self-oscillations of human vocal folds with Hertz model of impact forces. *Journal of Fluid and Structures*, **20**, (2005), 853-869.
3. TITZE, I.R.: *The Myoelastic Aerodynamic Theory of Phonation*. National Centre for Voice and Speech, Iowa City, 2006, ISBN 0-87414-122-2.
4. PELORSON, X., HIRSCHBERG, A., VAN HASSEL, R.R., WIJANDS, A.P.J. AND AUREGAN, Y.: Theoretical and experimental study of quasisteady-flow separation within the glottis during phonation. *Journal of the Acoustical Society of America*, **96**, (1994), 3416-3431.
5. ALIPOUR, F. AND TITZE, I.R.: *Combined simulation of two-dimensional airflow and vocal fold vibration*. P.J. Davis, N.H. Fletcher (Eds.), Vocal Fold Physiology, Controlling Complexity and Chaos. Singular, San Diego, 1996.
6. DE VRIES, M.P., SCHUTTE, H.K., VELDMAN, A.E.P. AND VERKERKE, G.J.: Glottal flow through a two-mass model: Comparison of Navier-Stokes solutions with simplified models. *Journal of the Acoustical Society of America*, **111**(4), (2002), 1847-1853.
7. ROSA, M.O. AND PEREIRA, J.C.: A contribution to simulating a three-dimensional larynx model using the finite element method. *Journal of the Acoustical Society of America*, **114**(5), (2003), 2893-2905.
8. DEDOUCH, K., HORÁČEK, P. AND ŠVEC, J.G.: *Frequency modal analysis of supraglottal vocal tract*. N. S. Ferguson, H. F. Wolfe, M. A. Ferman, S. A. Rizzi (Eds.), Structural Dynamics: Recent Advances University of Southampton, England, 2000, pp. 863-874, ISBN 0854327215.
9. HONZÁTKO, R., KOZEL, K., AND HORÁČEK, J.: Flow over a profile in a channel with dynamical effects. *Proceedings in Applied Mathematics*, **4**(1), (2004), 322-323. ISSN 1617-7061.
10. FÜRST, J., JANDA, M. AND KOZEL, K.: Finite volume solution of 2D and 3D Euler and Navier-Stokes equations. J. Neustupa, P. Penel (Eds.), Mathematical Fluid Mechanics. Berlin, (2001). ISBN 3-7643-6593-5.
11. JAMESON, A., SCHMIDT, W., AND TURKEL, E.: Numerical Solution of the Euler Equations by Finite Volume Methods Using Runge-Kutta Time-Stepping Schemes, AIAA, Paper 81-1250, (1981).

12. FOŘT, J. AND KOZEL, K.: Numerical solution of several models of internal transonic flow. *Applications of Mathematics*, 8(6), (2003), 515-524. ISSN 0862-7490.
13. KOZEL, K., LOUDA, P. AND SVÁČEK, P.: Numerical Solution of Flow in Backward Facing Step, Numerical Mathematics and Advanced Applications, ENUMATH 2003, (2004), Berlin, pp. 596-604.
14. DOBEŠ, J., FOŘT, J., FÜRST, J., HALAMA, J. AND KOZEL, K.: Numerical Solution of Transonic Flows in Turbine Cascades, 1st International Conference FSCCE. Athens, 2004.
15. PROKOP, V. AND KOZEL, K.: Numerical Modelling of Bypass Flow, Numerical Mathematics and Advanced Application. Berlin, (2004), pp. 708-715. ISBN 3-540-21460-7.
16. KOZEL, K., LOUDA, P. AND PŘÍHODA, J.: Numerical Modelling of Complex Turbulent Flows, Proceedings of "16th International Symposium on Transport Phenomena", CD-ROM, CTU in Prague, (2005).
17. KOZEL, K., HONZÁTKO, R. AND HORÁČEK, J.: Numerical Solution of 2D Incompressible Flow over a Vibrating Airfoil, Proceedings of Conf. On Modelling Fluid Flow, Budapest, (2006), pp. 233-240, ed. T. Lajos, J. Vad. ISBN 963 06 0361 6.
18. ŠIMONEK, J., KOZEL, K. AND TREFILÍK, J.: Numerical Solution of Inviscid and Viscous Flows with Application, Topical Problem of Fluid Mechanics (2007). Prague, IT CAS CZ, 2007, pp. 169-172. ISBN 978-80-87012-04-8.
19. PUNČOCHÁŘOVÁ, P., KOZEL, K. AND FÜRST, J.: An unsteady numerical solution of viscous compressible flows in a channel, Programs and Algorithms of Numerical Mathematics 13. Prague, Math. Institute ASCR, (2006), pp. 220-228. ISBN 80-85823-54-3.
20. PUNČOCHÁŘOVÁ, P., KOZEL, K. AND FÜRST, J.: Unsteady, Subsonic Inviscid and Viscous Flows in a Channel, Fluid Dynamics 2005. Prague, IT CAS CZ, (2005), pp. 125-128. ISBN 80-85918-94-3.
21. PUNČOCHÁŘOVÁ, P., KOZEL, K., AND FÜRST, J.: Numerical Solution Viscous Flows in a 2D Channel with Unsteady Wall Boundary, Application of Experimental and Numerical Methods in Fluid Mechanics. University of Žilina, Mechanical Engineering Faculty, 2006, 177-182. ISBN 80-8070-533-X.
22. PUNČOCHÁŘOVÁ, P., KOZEL, K., FÜRST, J., AND HORÁČEK, J.: Numerical Solution of Unsteady Viscous Compressible Flows in a Channel, Topical Problem of Fluid Mechanics 2006. Prague, IT CAS CZ, 2006, pp. 133-136. ISBN 80-85918-98-6.
23. LOUS, N.J.C., HOFMANS, G.C.J., VELDHUIS, N.J. AND HIRSCHBERG, A.: A symmetrical two-mass model vocal-fold model coupled to vocal tract and trachea, with application to prosthesis design. *Acta Acoustica*, **84**, (1998), 1135-1150.

COMPUTATIONS OF THE ACOUSTIC FIELD IN AN ANNULAR GAS TURBINE COMBUSTION CHAMBER

RÓBERT ZOLTÁN SZÁSZ, CHRISTOPHE DUWIG, LÁSZLÓ FUCHS

Department of Energy Sciences, LTH, Lund University

PO.Box. 118, SE-22100 Lund, Sweden

`robert-zoltan.szasz@vok.lth.se`

[Received: January 8, 2007]

Abstract. The acoustic field in an annular gas turbine combustion chamber is determined using a hybrid approach. The flow solver is based on Large Eddy Simulations to account for turbulence and on a flamelet-based method to model combustion. The acoustic part solves an inhomogeneous wave equation, the acoustic sources being given by the flow solver. The flow computations focus on a single nozzle. To model the entire combustion chamber, the acoustic sources are manifold and imposed in thirty instances. Several perturbing parameters were studied. The computations revealed that time shift in the acoustic sources of consecutive nozzles has a major influence on the resulting acoustic field, space shift of the sources or counter rotation has reduced effect.

Keywords: acoustics, CFD, gas turbine, hybrid approach, LES

1. Introduction

To achieve low pollutant emission levels, a common approach is to use lean premixed or partially premixed flames in gas turbine combustors. Such lean premix conditions, however, are prone to develop thermo-acoustic instabilities which appear when the heat-release fluctuations are in phase with the pressure fluctuations. The amplification of pressure oscillations may lead to the malfunctioning of the device, or, in the worst case, to its failure [1]. Even in cases when the average flow parameters are not affected by the acoustic fluctuations, their presence may lead to increased NO_x emission levels [2]. Thus, it is needed that combustion instabilities are predicted as early as possible, in the best case already in the design phase.

There is an intensive research focused on the passive and active control of combustion instabilities. Passive control usually consists in modifications of the combustor geometry (see e.g. [3]). Passive control has the advantage of simplicity (and by this reliability). However, it is limited to a certain working regime of the gas turbine. Furthermore, combustion control is not necessarily ensured when the combustor design is changed. Thus, there is an intensive research focusing on active combustion control technologies [4, 5, 6, 7], most of them being based on the modulation of the

fuel stream. For such active control technologies there is a need for fast numerical models. Commonly, one divides the gas turbine in a network of acoustic elements, their behaviour being described by transfer functions. For simple geometries such transfer functions can be determined analytically. For the complex geometry of gas turbine combustors, however, experimental or numerical tools are needed to evaluate their answer for acoustic excitations. The presence of flames renders the problem even more complex. Schuermans et al. [4] used numerical tools to model the gas turbine combustion chamber and experiments to model the response of combustion. Caraeni et al. [8] developed a fast method, based on the Arnoldi algorithm to determine the resonance frequencies of a combustion chamber. More recently, Bethke et al. [9] determined the resonant frequencies using finite-element based methods. Nevertheless, further research is needed to predict the interaction of turbulence, acoustics and combustion. Recently, Schmitt et al [2] carried out such studies on a scaled gas turbine combustor with a single burner. Real gas turbines, however, have annular combustion chambers with multiple burners. In this paper, we focus on such an annular gas turbine combustion chamber.

The acoustic field can be determined by solving the compressible Navier-Stokes equations using Direct Numerical Simulations (DNS) or Large Eddy Simulations (LES) [10, 2]. This method, however, is highly inefficient for low-Mach number flows.

An alternative approach is to use hybrid methods. For low Mach numbers one can assume that the acoustic fluctuations are small, compared to the fluid dynamic fluctuations, and the variables can be split in an incompressible part and a correction, which accounts for the compressibility effects. In this way, the compressible Navier Stokes equations are split in a set of incompressible Navier Stokes equations and a set of acoustic equations. Olbricht et al. [11] used a hybrid approach based on LES and acoustic perturbation equations for studying the noise generated by the isothermal flow in a model gas turbine combustor. A similar approach has been used by Bui et al. [12] for the evaluation of noise emitted by a non-premixed jet flame. Using first order approximations, the acoustic equations may be reorganised into an inhomogeneous wave equation. This hybrid approach has higher computational efficiency compared to direct methods, since the time step in the flow solver is not limited by the sound speed, but by the flow velocity. Furthermore, the solution methods for incompressible flows are more robust. Another advantage is that different grids (allowing different grid resolutions) may be used in the flow and acoustic computations. The major disadvantages of the hybrid methods is the increased complexity of maintaining two separate solvers and that they are limited to low Mach number flows.

Here, such a hybrid approach is used. The method was implemented by Mihaescu et al. [13] and successfully applied for the computation of jet noise. Recently, the method was further developed by Duwig et al. [14] to predict thermo-acoustic instabilities in a model gas turbine combustion chamber. Szász et al. [15] applied the hybrid approach to determine the acoustic field generated by turbulence in a model annular gas turbine combustion chamber.

In this paper, the acoustic field in an annular gas turbine combustion chamber having thirty Lean Premixed Prevaporized (LPP) burners is determined. Since flow computations in the whole combustion chamber would be computationally too demanding, the flow field is determined in a region of the combustion chamber corresponding to a single burner. The flow computations are based on LES to account for turbulence and on a flamelet-based approach to model combustion [16]. Second, the acoustic field is determined for the whole combustion chamber by solving an inhomogeneous wave equation, similar to Lighthill's analogy. The source terms needed for the acoustic computations are provided by the flow solver and interpolated onto the acoustic grid in thirty instances to account for each burner. In the base case the acoustic sources are copied identically to the nozzles. This case is compared to cases where the sources are imposed in a counter-rotating manner, or where phase shifts (in space or time) are imposed for successive nozzles. The resulting acoustic field is evaluated in terms of rms acoustic density fluctuations and its frequency spectra.

2. Numerical methods

The computations have been carried out in two steps. First, the unsteady flow field was computed for a model combustion chamber having a single nozzle. The flow solver provided the acoustic source terms needed by the acoustic solver. In the second step the acoustic sources were loaded into the acoustic solver and copied in thirty instances to simulate the presence of all nozzles.

2.1. Flow solver. The semi-compressible Navier-Stokes equations are discretized on a Cartesian staggered grid. By semi-compressibility is meant that the density is depending only on the temperature, but not on the pressure. Flame propagation is described using a progress variable, c , equation [17]:

$$\begin{aligned} \frac{\partial \bar{\rho} \tilde{c}}{\partial t} + \nabla \cdot (\bar{\rho} \tilde{u} \tilde{c}) &= \frac{\rho_u S_L(\tilde{Z}) \Xi \Delta}{a} \nabla^2 \tilde{c} + \rho_u S_L(\tilde{Z}) \Xi \frac{1}{\Delta} \Pi_c(\tilde{c}, a) + \\ &+ \frac{2}{\tilde{Z}} \frac{\rho_u S_L(\tilde{Z}) \Xi \Delta}{a} \nabla \tilde{c} \cdot \nabla \tilde{Z}, \end{aligned} \quad (2.1)$$

where the production term Π_c is read from a precomputed library [16]. The mixing is obtained via the filtered mixture fraction equation:

$$\frac{\partial \bar{\rho} \tilde{Z}}{\partial t} + \nabla \cdot (\bar{\rho} \tilde{u} \tilde{Z}) = \nabla \bar{\rho} D \nabla \tilde{Z}. \quad (2.2)$$

The filtered density is computed from the temperature using the ideal gas law. The temperature is computed using the progress variable. That is,

$$\bar{\rho} = \frac{p_0}{R \tilde{T}}, \quad (2.3)$$

with

$$\tilde{T} = T_u(\tilde{Z}) + (T_b(\tilde{Z}) - T_u(\tilde{Z})) \cdot \tilde{c}. \quad (2.4)$$

The governing equations are discretized using finite differences. Third order discretization is used for the convective part and fourth order for the diffusive part. The

high-order accuracy is achieved using a defect correction approach. It was proved several times in the literature (see e.g. [18]) that RANS based approaches fail to describe the flame movements properly. Here, LES is used to account for turbulent fluctuations. No explicit sub-grid scale (SGS) model is used. It is assumed that the third order upwind scheme accounts for the dissipative effect of the SGS terms. This approach has been successfully used in a wide range of applications [19, 20, 21]. The grid can be locally refined to reduce the computational requirement. 1.8 million cells were used in the flow computations, having 60 cells per premixing tube diameter.

2.2. Acoustic solver. In the acoustic solver an inhomogeneous wave equation is solved:

$$\frac{\partial^2 \rho'}{\partial t^2} - \frac{1}{M^2} \frac{\partial^2 \rho'}{\partial x_i \partial x_i} = \frac{\partial^2 T_{ij}}{\partial x_i \partial x_j} + \alpha \frac{\partial \omega}{\partial t}, \quad (2.5)$$

where the first term on the right hand side stands for the acoustic sources due to velocity variations and entropy effects:

$$T_{ij} = \rho u_i u_j + \delta_{ij} \left(p - \frac{1}{M^2} \rho \right). \quad (2.6)$$

The second term on the right hand side of Eq. 2.5 represents the sound sources generated by the unsteady heat release and is given by [14]:

$$\omega = C_p (T_b(\tilde{Z}) - T_u(\tilde{Z})) \rho_u S_L(\tilde{Z}) \Xi \frac{1}{\Delta} \Pi_c(\tilde{c}, a). \quad (2.7)$$

Eq. 2.5 is discretized on a uniform cartesian grid (without local refinements) using finite differences. Second order central differences are used for the space derivatives. In time an explicit Lax-Wendroff type discretization is applied. The acoustic sources (Eqs. 2.6 and 2.7) are computed by the flow solver and stored in files. The sources are read in by the acoustic solver and filtered onto the acoustic grid by a Gaussian filter having the filter width of two cell sizes. Since the time step needed by the acoustic solver is shorter than the period with which the acoustic sources have been saved, the acoustic sources are obtained by linear interpolation between two successive source data sets. The acoustic computations cover a longer time than the time span covered by the acoustic sources, thus the acoustic source files are repeated periodically in time (i.e. it is assumed that the first acoustic source file is following after the last acoustic source file). The acoustic sources being pre-computed, the sources imposed at different nozzles may differ, or may be differently arranged. In this way phase shifts between consecutive nozzles may be easily imposed both in space and time. A low-pass digital filter is used to avoid spurious oscillations [14]. The shape of the combustion chamber is imposed by blocking the inactive cells.

3. Problem set-up

The geometry used in the flow computations is sketched in Figure 1. In the flow computations only a section of the annular combustion chamber corresponding to a single nozzle was considered. The geometry is composed of a premixing tube, a combustion chamber and a contraction region. The chamber is contracted in only one direction. The premixing tube has a conical and a cylindrical part. Since experimental measurements are available only in the cylindrical part, the cone is neglected in the flow computations (but it is accounted for in the acoustic solver). In the followings, all dimensions are normalised with the diameter of the premixing tube and x is the stream-wise direction. The premixing pipe has a length of 2.7. The combustion chamber has a rectangular cross-section of 3.8×3.8 and a total length (including the converging outlet) of 6. The length of the combustion chamber was shortened with two equivalent diameters in the flow computations to match conditions for which experimental data is available. As it is shown in [16], where the flow is computed in the same geometry, the resulting velocity field is in good agreement with the experimental data. It is believed, that the combustion chamber is sufficiently long so that the discrepancy in the combustion chamber length has minor effects on the flow field in the inlet region, where the dominant acoustic sources are located. For acoustic computations the size and shape of the combustion chamber influences its eigenfrequencies, and by this, the resulting acoustic field. Since in the present paper the flow and acoustic computations are decoupled we have the possibility to predict the acoustic field for different geometric configurations in an efficient way, with one (computationally demanding) flow computation, provided that the geometric changes do not significantly alter the flow field.

A preheated (700 K) methane-air mixture is burned. The overall equivalence ratio is 0.42 but a non-constant equivalence ratio profile is enforced at the inlet. The Reynolds number is 100000 and the inlet swirl number 0.52. The inlet Mach number is 0.1. The CFL number for the flow computations was 0.2. For the flow solver zero gradient outlet conditions are imposed with flux correction. The walls are non-slip and adiabatic, no wall functions are used. There were two main reasons to opt wall conditions in favor of setting periodicity boundary conditions on two of the side-walls. First, this set-up matches the experimental conditions available for comparison [16]. Second, even periodicity conditions could not capture the physics of a multiple-burner set-up. As it is shown in [22], the interaction of neighboring burners is complex and requires the explicit modeling of individual nozzles. At the inlet a constant velocity profile is set above which fluctuations due to the acoustic velocity fluctuations are imposed.

A 3D view of the acoustic domain is shown in Figure 2, the thick line denotes approximately the limits of the geometry used in the flow computations. Thirty nozzles are placed equidistantly in azimuthal direction on a circle with a radius of 12.1. The height of the combustion chamber is 3.8 while its length is 10.7. Figure 3 shows a sketch of the transversal cross section of the acoustic domain. $L1...L6$ denote the locations of the axial lines along which data is saved for post-processing. In the

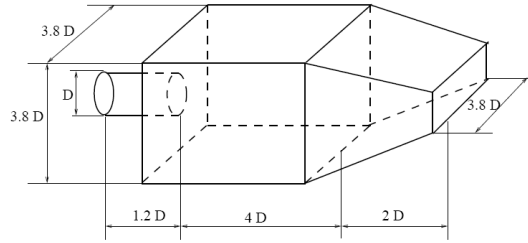


Figure 1. The geometry of a single combustor

followings, by "first burner" we denote the one which has the symmetry axis marked $L1$. In the acoustic solver reflecting boundary conditions are used everywhere, except the outlet, where non-reflecting conditions were imposed.

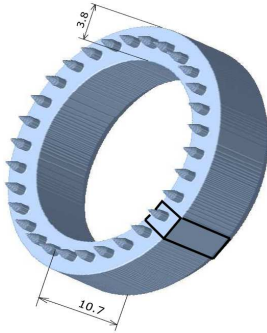
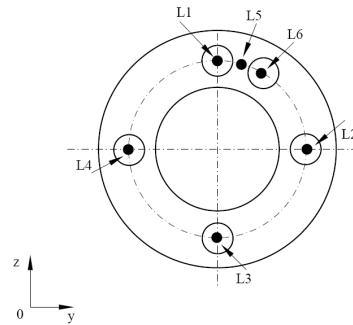


Figure 2. 3D view of the acoustic domain

Figure 3. Sketch of the cross section of the acoustic domain. $L1...L6$ mark the axial lines along which data is saved for post processing

4. Results

The computations have been carried out in two steps. First the acoustic sources have been determined using the flow solver described in section 2.1. A qualitative picture of the acoustic source terms can be seen in the instantaneous snapshot shown in Figure 4. The source terms have been normalised with the maximum value. One can observe that the dominant acoustic sources are found in the flame region. The spectrum of the acoustic sources revealed that the lowest dominant frequency is at $St \approx 0.6$. The Strouhal number is defined as:

$$St = \frac{f}{UL}, \quad (4.1)$$

where f is the frequency, U the velocity scale and L the length scale. Here, U is the inlet velocity magnitude and L is the diameter of the premixing tube. The sources have been saved for a period covering four periods of this frequency. It is believed that this time span should be long enough. Nevertheless, future computations are planned to evaluate the influence of the time interval covered by the acoustic source data set. This data set is imposed periodically in the acoustic solver. For further details about the flow field the user is referred to Duwig et al [14].

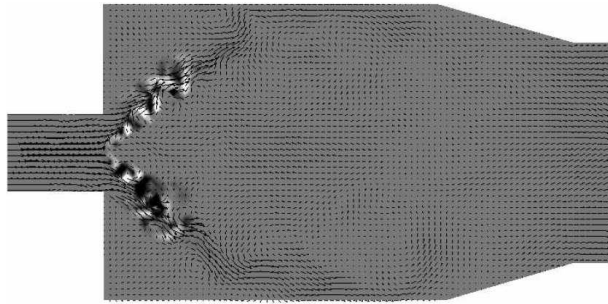


Figure 4. Instantaneous snapshot of the acoustic source terms and velocity vectors

In the second step, the acoustic sources have been read into the acoustic solver. Altogether eight cases have been run with the acoustic solver, a summary of the cases being presented in Table 1. The grid sensitivity was evaluated by solving the acoustic

Table 1. Summary of cases

Nr.	Nr. cells [<i>mill.</i>]	Counter rot.	Time shift [/ <i>noz.</i>]	Phase shift [<i>deg/noz.</i>]
1	4.6	No	0	0
2	15.3	No	0	0
3	36.0	No	0	0
4	15.3	Yes	0	0
5	15.3	No	0.025	0
6	15.3	No	0.05	0
7	15.3	No	0	6
8	15.3	No	0	90

field using three different grid resolutions, totally having 4.6, 15.3 and 36 million cells, respectively. To simulate counter rotating nozzles, in the fourth case, the sources have been imposed mirrored for every second nozzle. In real annular combustion chambers the flow field is not identical for each nozzle. To simulate the non-uniformity of the flow field, perturbations have been imposed. In cases 5 and 6 the sources of consecutive nozzles were imposed with a time shift of 0.025 and 0.05, respectively. Since the solver

is nondimensional the time shift is also non-dimensional, the unit time is the time required to travel a distance of one premixing tube diameter with the average axial speed in the premixing tube. In cases 7 and 8, the sources had an azimuthal phase shift between consecutive nozzles of 6 and 90 *degrees*, respectively. The averages in the acoustic solver were computed for 100000 timesteps, corresponding to 50 time units. During this period the acoustic waves can propagate over a distance of 500 times the combustor length.

In the followings the grid sensitivity study will be presented shortly, followed by a detailed description of the acoustic field for the base case (case 2). Next, the influence of the above-mentioned perturbations will be presented and discussed.

4.1. Grid sensitivity. Three different cases have been evaluated, having totally 4.6, 15.3 and 36 million cells. The size of the cells was 0.125, 0.0917 and 0.0625 corresponding to 8, 12 and 16 cells per premixing tube diameter, respectively. Figure 5 shows the spectrum of the acoustic density fluctuation for the three considered cases at a point located on the symmetry axis of the first nozzle, immediately downstream of the premixing tube. One can observe that the low frequency fluctuations ($St = 0.15, 0.45, 0.6$) are captured in all three cases, thus the lowest resolution would be enough to capture the dominant frequencies in the combustion chamber. However, high grid resolutions are desired to capture accurately the frequencies in the premixing tube. As it regards the computational cost, cases 2 and 3 require a computational time increased with 63 % and 173 %, respectively. Since case 3 needed almost 2 Gb memory to run, while for case 2 it was enough one Gb, case 2 was chosen as base case for further computations.

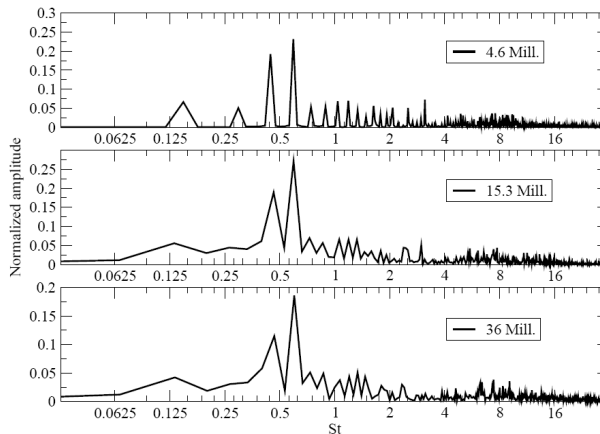


Figure 5. Acoustic pressure fluctuation spectra for three grid resolutions, at a point on line $L1$, $x = 3$

4.2. **Base case.** Figure 6 presents the rms of the acoustic density fluctuation in a longitudinal cross section. The maximum acoustic sources are located in the flame region. This is where the largest acoustic fluctuations are generated. The waves are propagating downstream and reflected from the combustion chamber walls. One can observe as well that acoustic fluctuations are propagated also upstream into the premixing tube. These fluctuations are important since they may influence the mixing process and by this may induce thermo-acoustic instabilities. The slight asymmetry of the contour plot could be probably improved with longer averaging time.

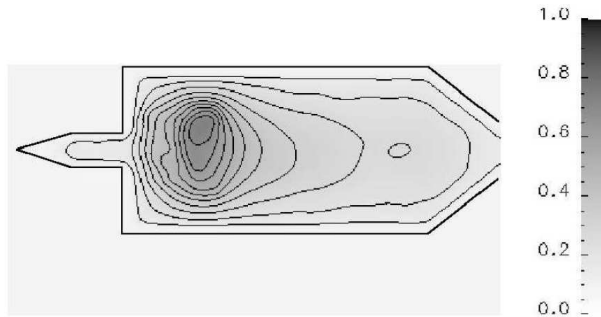


Figure 6. Normalised rms of the acoustic density fluctuation in a longitudinal cross section. The thick line denotes the contour of the combustion chamber

Figure 7 shows the evolution of the rms of the acoustic source terms (continuous line) and acoustic density fluctuation (dashed line) along the symmetry axis of the first nozzle (line $L1$ in Figure 3). The contour of the combustion chamber is also marked with a dotted line. The amplitudes of the fluctuations were normalised with the maximum values. One can observe that the highest acoustic density fluctuations are not located exactly at the place of the largest fluctuations of the acoustic sources, but shifted approximately one length unit downstream. This shift is probably due to the proximity of the premixing tube and the back-wall.

The frequency spectra of the acoustic source term and acoustic density fluctuation at a point located on line $L1$ at an axial position of three diameters is displayed in Figure 8.

One can observe a peak in both the acoustic source and acoustic density fluctuation spectra at $St = 0.15$ which corresponds to the period where the acoustic sources have been saved. Further peaks can be seen in both spectra at $St = 0.46, 0.6,$ and 1.2 . A major difference is that while in the acoustic source spectra $St = 1.2$ is dominant, in the acoustic density fluctuation spectra $St = 0.6$ has the largest amplitude. To identify this mode Proper Orthogonal Decomposition (POD) has been used. For the POD analysis the time and space evolution of the acoustic density fluctuation has been saved in a longitudinal and three transversal cross-sections. Figure 9 shows the first most energetic mode (corresponding to the eigenvalue with the largest magnitude).

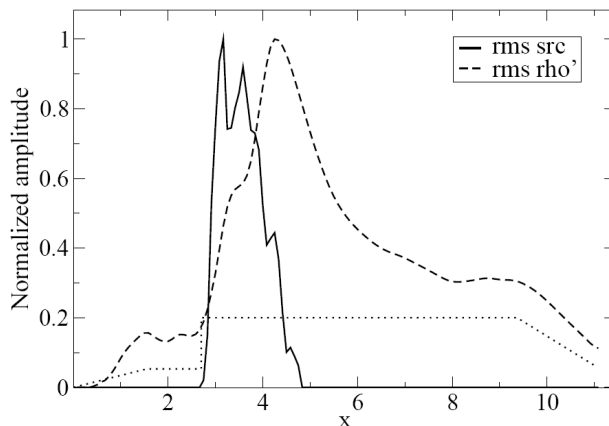


Figure 7. RMS of the acoustic source term (continuous line) and acoustic density fluctuation (dashed line) along line $L1$. The dotted line marks the contour of the combustion chamber

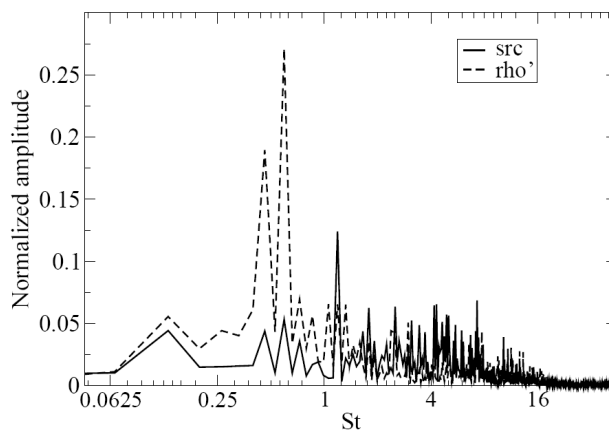


Figure 8. Frequency spectra of the acoustic source term (continuous line) and acoustic density fluctuation (dashed line) at a point on line $L1$, $x = 3D$

As one can see, this most energetic mode is an axial one, there are no variations in azimuthal direction. By projecting the individual snapshots onto a mode, one can reconstruct the time evolution of that specific mode. Reconstruction of the axial mode shown in Figure 9 revealed that it has indeed $St = 0.6$.

A comparison of the acoustic density fluctuation spectra at three different axial positions is shown in Figure 10. The first point (upper graph) is located in the premixing tube; the second (middle graph) in the source region while the third one towards the



Figure 9. Iso-contours of the first most energetic mode computed with POD of the acoustic density fluctuation in a transversal cross-section at $x = 3.7$

outlet of the combustion chamber. In the premixing tube high-frequency ($St \approx 9$) oscillations dominate. This is due to the fact that the lower frequency waves cannot enter in resonance with the premixing tube due to its reduced diameter compared to the height of the combustion chamber. Towards the outlet of the combustion chamber (lower graph) the dominant frequencies are higher than in the source region because of the interference of the reflected waves.

Figure 11 shows the iso-contours of the acoustic density fluctuation in a transversal cut, located at nine diameters downstream. The normalization has been carried out with the same reference value as in Figure 6 so that the two figures are comparable. The field is uniform in azimuthal direction indicating the lack of low-frequency azimuthal modes. This conclusion is confirmed by Figure 12 which presents the variation of the rms acoustic density fluctuation along the lines marked $L1 - L6$ in Figure 3. One can observe that the plots along the symmetry axes of the nozzles are practically identical, while the line located between two nozzles ($L5$) exhibits lower rms values in the flame region.

4.3. Influence of counter-rotation. Counter rotating nozzles were simulated by imposing the acoustic sources in a mirrored way for every second nozzle. Of course, in the real case the flow field generated by counter rotating jets differs from the one

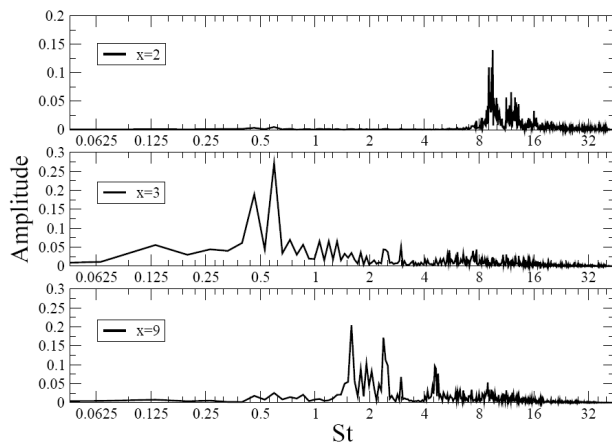


Figure 10. Frequency spectra of the acoustic density fluctuation at points on line $L1$, $x = 2$ (up), $x = 3$ (centre), $x = 9$ (down)

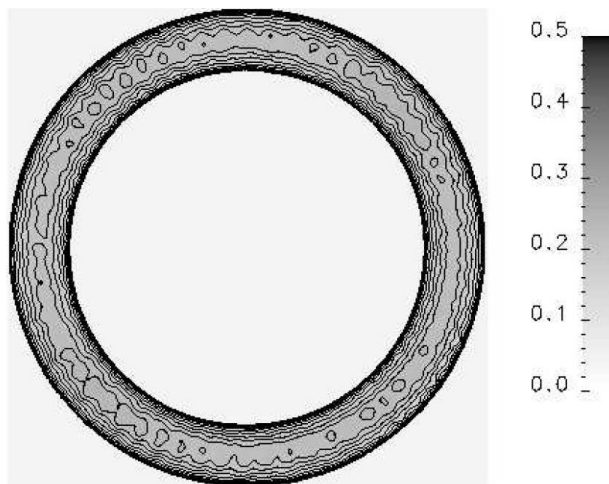


Figure 11. Normalised rms of the acoustic density fluctuation in a transversal cross section ($x = 9$)

produced by co-rotating jets (see e.g. [22]). Nevertheless, the approach presented here is a "low-cost" approximation.

The variation of the rms acoustic density fluctuation along two axial lines is presented in Figure 13, for the co- and counter-rotating cases. No difference can be observed along the symmetry axis of the first burner (line $L1$). Conversely, significant influence can be seen along the axial line located between two nozzles ($L5$). In the counter-rotating case higher rms values are observed than in the co-rotating

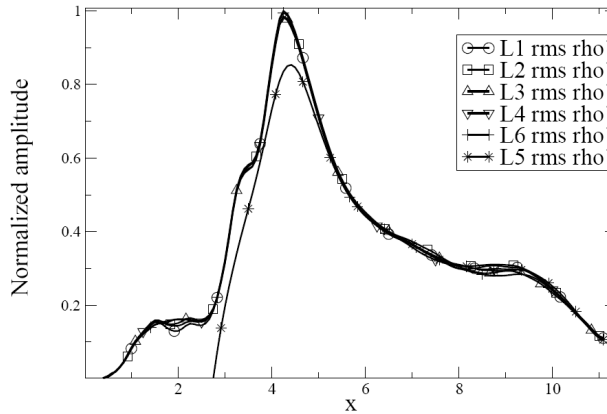


Figure 12. RMS of the acoustic density fluctuation along lines $L1 - L6$

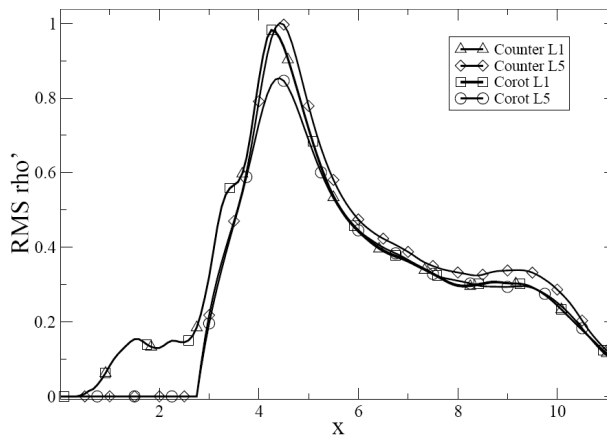


Figure 13. RMS of the acoustic density fluctuation along lines $L1$ and $L5$ for the counter- and co-rotating cases

case. This observation is in agreement with [15] where isothermal computations in a model annular gas turbine combustion chamber are presented. In [15] counter-rotation was accounted for already in the flow computations, thus the elevated levels of acoustic density fluctuation are not necessarily due to differences in the flow fields of the counter- and co-rotating cases. The frequency spectra of the acoustic density fluctuation (Figure 14) at a point located three diameters downstream reveal minor influences due to the counter-rotating configuration. The frequency with $St = 0.46$ is slightly damped. At monitoring points located further downstream (not shown) no significant differences could be observed (compared to the co-rotating case).

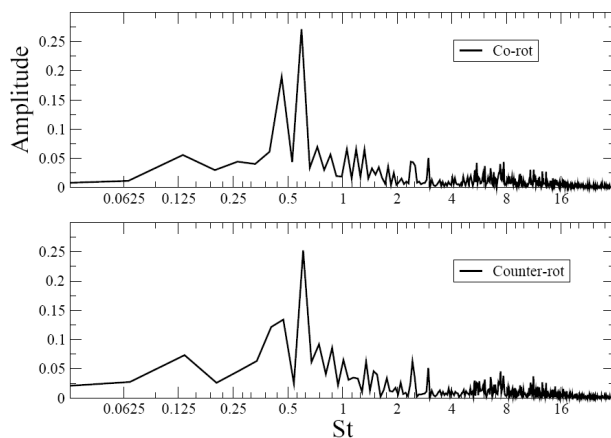


Figure 14. Acoustic density fluctuation spectra for co- (upper graph) and counter-rotating (lower graph) configurations. Monitoring point located on line $L1$, $x = 3$

4.4. Influence of time shift. To simulate phase shifts between nozzles two cases have been run. The acoustic sources have been shifted in time for successive nozzles with 0.025 and 0.05, respectively. Figure 15 displays the iso-contours of the rms acoustic density fluctuation in a transversal cut at $x = 9$, for the case with a time shift of 0.025. The field was normalised again the same way as the field shown in

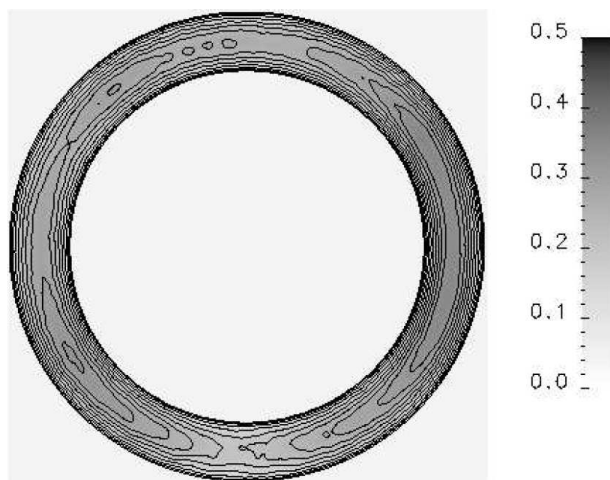


Figure 15. Normalised rms of the acoustic density fluctuation, transversal cross section, $x = 9$

Figure 6. It can be clearly seen that the shift causes non-uniformity in azimuthal

direction. The same conclusion can be drawn looking at the axial variation of the acoustic pressure fluctuation rms, shown in Figure 16.

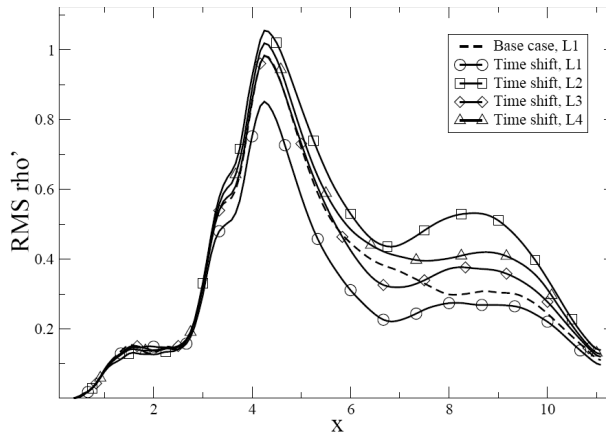


Figure 16. RMS of the acoustic density fluctuation along axial lines for the case with a time shift of $0.025/\text{nozzle}$ (continuous lines) and the base case (dashed line)

Figure 17 shows a comparison of the spectra of the acoustic density fluctuation at a point located on line $L1$ at $x = 9$ for the base case (upper graph), the case with a time shift of 0.025 (centre graph) and the one with 0.05 (lower graph). One can observe that as long as the base case is dominated by frequencies of $St \approx 1.6$ and $St \approx 2.4$, the cases with time shift have the highest amplitude at $St \approx 1.9$. Furthermore, in these cases the $St \approx 4.6$ component is damped as well. Closer to the inlet (not shown) the time shift has no significant influence on the frequency spectra.

4.5. Influence of phase shift. During cases 7 and 8 the acoustic sources of successive nozzles were rotated around the symmetry axes of the burners with 6 and 90 degrees, respectively. These cases were meant to model spatial non-uniformities.

Iso-contours of the acoustic density fluctuations as well as axial plots of the acoustic density fluctuation (not shown) revealed negligible influence of the imposed phase perturbations on the resulting acoustic fields. Neither in the frequency spectra in the source region could be seen differences. Further downstream (see Figure 18) it was found, that the perturbations did not change the low frequency part ($St < 4$) of the spectra, but the mode with $St \approx 4.6$ is damped. Furthermore, in case 8, a new dominant frequency at $St \approx 4$ is generated.

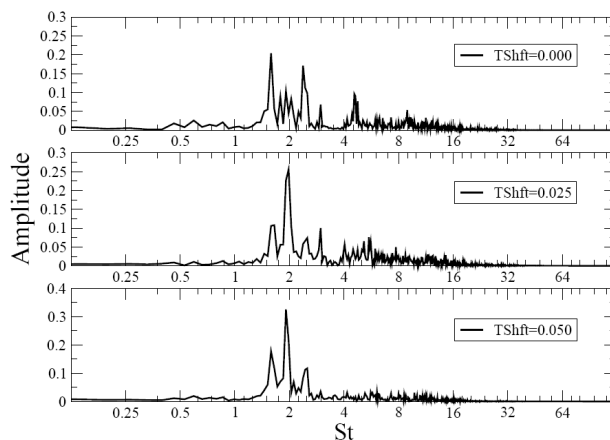


Figure 17. Frequency spectra of the acoustic density fluctuation for three cases at points situated on line $L1$, $x = 9$

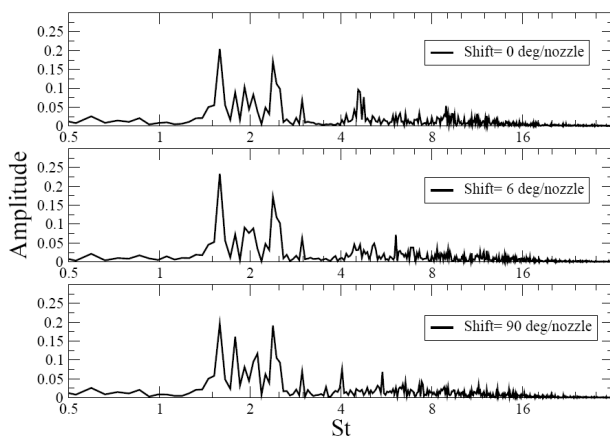


Figure 18. Frequency spectra of the acoustic density fluctuation for three cases at points situated on line $L1$, $x = 9$

5. Conclusions

The acoustic field in an annular gas turbine combustion chamber has been computed using a hybrid approach. The acoustic field was determined by solving an inhomogeneous wave equation. The acoustic sources have been computed separately in a region of the combustion chamber corresponding to a single nozzle.

The computations revealed that there are low-frequency oscillations present in the combustion chamber. Imposing the acoustic sources in a counter-rotating manner and prescribing a phase shift of successive nozzles was found to have minor effect on the

resulting acoustic field. In contrast, when the acoustic sources of consecutive nozzles were shifted in time the acoustic field has been strongly influenced.

Further work is needed to identify the observed low frequency oscillations. Furthermore, the method has to be extended to allow for back-coupling of the acoustic oscillations to the flow field.

Acknowledgement. The authors would like to acknowledge the financial support of the Swedish research Council (VR). The computational time offered at the Center for Scientific and Technical Computing at Lund University (LUNARC) and within the allocation program SNAC is highly appreciated.

References

1. LIEUWEN, T. AND YANG, V.: Combustion Instabilities in Gas Turbine Engines: Operational Experience, Fundamental Mechanisms and Modeling, No. 210 in Progress in Astronautics and Aeronautics, AIAA,(2006), ISBN 156347669X.
2. SCHMITT, P., POINSOT, T., SCHUERMANS, B. AND GEIGLE, K.P.: Large-eddy simulation and experimental study of heat transfer, nitric oxide emissions and combustion instability in a swirled turbulent high-pressure burner. *J. Fluid Mech.*, **570**, (2007), 17-46.
3. STEELE, R., COWELL, L., CANNON, S., AND SMITH, C.: Passive control of combustion instability in lean premixed combustors. In proc. of International Gas Turbine and Aeroengine Congress and Exhibition, (1999), pp. 1-8.
4. SCHUERMANS, B., BELLUCCI, V. AND PASCHEREIT, C.O.: Thermoacoustic modeling and control of multi burner combustion systems. ASME paper, (2003), 2003-GT-38688.
5. DOWLING, A. AND MORGANS, A.: Feedback control of combustion oscillations. *Annu. Rev. Fluid Mech.*, **37**, (2005), 151-182.
6. YI, T. AND GUTMARK, E.J.: Adaptive control of combustion instability based on dominant acoustic modes reconstruction, AIAA paper, (2006), AIAA 2006-751.
7. BELLOWS, B.D., HREIZ, A. AND LIEUWEN, T.: Nonlinear interactions between driven and self-excited acoustic oscillations in a premixed combustor, AIAA paper, (2006), AIAA 2006-755.
8. CARAENI, M.L. AND CARAENI, D.A. AND FUCHS, L.: Fast algorithm to compute resonance frequencies of a combustion chamber, AIAA paper, (2003), AIAA 2003-3235.
9. BETHKE, S., WEVER, U. AND KREBS, W.: Stability analysis of gas-turbine combustion chamber, AIAA paper, (2005), AIAA 2005-2831.
10. MENON, S., STONE, C., SANKARAN, V. AND SEKAR, B.: Large-eddy simulation of combustion in gas turbine combustors, AIAA paper, (2000), AIAA 2000-0960.
11. OLBRICHT, C., FLEMMING, F., SADIKI, A., JANICKA, J., BAKE, F., MICHEL, U. AND RÖHLE, I.: A study of noise generation by turbulent flow instabilities in a gas turbine model combustor, ASME paper, (2005), GT2005-69029.
12. BUI, T.P., MEINKE, M. AND SCHRÖDER, W.: A hybrid method for combustion noise based on LES and APE, AIAA paper, (2005), AIAA 2005-3014.
13. MIHAESCU, M., SZÁSZ, R.Z., FUCHS, L. AND GUTMARK, E.: Numerical investigations of the acoustics of a coaxial nozzle, AIAA paper, (2005), AIAA 2005-0420.

14. DUWIG, C., GHERMAN, B., MIHAESCU, M., SALEWSKI, M. AND FUCHS, L.: Numerical study of thermo-acoustic waves generation by a swirling flame using a new approach based on Large Eddy Simulation, ASME paper, (2005), GT2005-68136.
15. SZÁSZ, R.Z., MIHAESCU, M. AND FUCHS, L.: Computation of the acoustic field in an annular gas turbine combustion chamber using a hybrid approach, ASME paper, (2006), GT2006-90024.
16. DUWIG, C. AND FUCHS, L.: Study of flame stabilization in a swirling combustor using a new flamelet formulation. *Combust. Sci. Technol.*, **177**(8), (2005), 1485-1510.
17. DUWIG, C. AND FUCHS, L.: Study of a gas turbine combustion chamber: influence of the mixing on the flame dynamics, ASME paper, (2004), GT2004-53276.
18. GÜTHE, F., LACHNER, R., SCHUERMANS, B., BIAGIOLI, F., GENG, W., INAUEN, A., SCHENKER, S., BOMBACH, R. AND HUBSCHMIDT, W.: Flame imaging on the alstom ev-borner: Thermo-acoustic pulsations and cfd validation, AIAA paper, (2006), AIAA 2006-437.
19. FUREBY, C. AND GRINSTEIN, F.: Large Eddy Simulation of High-Reynolds-Number Free and Wall-Bounded Flows. *J. Comput. Phys.*, **181**, (2002), 68-97.
20. GARNIER, E., MOSSI, P., SAGAUT, P., COMTE, P. AND DEVILLE, M.: On the use of shock-capturing schemes for Large-Eddy Simulation. *J. Comput. Phys.*, **153**, (1999), 273-311.
21. MARY, I.: Large Eddy Simulation of vortex breakdown behind a delta wing. *Int. J. Heat and Fluid Flow*, **24**, (2003), 596-605.
22. SZÁSZ, R.Z., AND FUCHS, L.: Numerical modeling of flow and mixing of single and interacting swirling co-annular jets, In N. Kasagi, J. Eaton, R. Friedrich, J. Humphrey, M. Leschziner and T. Miyauchi (eds.), Proc. of Third International Symposium on Turbulence and Shear Flow Phenomena, vol. 2, (2003), pp. 663-668.

3D UNSTEADY FLOW IN A CENTRIFUGAL FAN: IMPELLER - VOLUTE INTERACTION

MOHAND YOUNSI, FARID BAKIR, SMAINE KOUIDRI AND ROBERT REY
Laboratoire d’Énergétique et de Mécanique des Fluides Interne LEMFI - ENSAM
151 Boulevard de l’Hôpital 75013 Paris, France
mohand.younsi@paris.ensam.fr

[Received: January 15, 2007]

Abstract. The purpose of this study is to show, using Computational Fluid Dynamics (CFD) tools, the complex phenomena related to the internal flow in a squirrel-cage fan and their influence on the aeroacoustic behaviour. These phenomena are the interactions and unsteadiness induced by the relative motion of the rotating blades compared to the volute. Thus, 3D unsteady calculation using Unsteady Reynolds Averaged Navier-Stokes (URANS) approach has been applied on the computational domains which have been divided into two zones, a rotating zone including the impeller and a stationary zone including the volute. The sliding mesh technique has been applied to the interfaces in order to allow the unsteady interactions between the two zones. The overall behaviour of the fan has been validated experimentally at different flow rates. The unsteady part is illustrated by the pressure and aerodynamic force fluctuations applied on the blade surfaces, and on different points from the lateral surface of the volute. Finally, using the pressure and the velocity fluctuations data acquired upon the surfaces of rotating blades, acoustic pressures have been computed using the Ffowcs Williams-Hawking (FW-H) analogy.

Keywords: aeroacoustics, centrifugal fan, CFD, turbomachinery

Nomenclature

a_0	[m/s]	Sound speed in quiescent medium
$f = 0$	[–]	Function that describes the source surface
F	[Hz]	Frequency
G	[–]	$= \tau - t + r/c$
$H(f)$	[–]	Heaviside function
M	[–]	Local Mach number vector of source with respect to a frame fixed to the undisturbed medium, with components M_i
n_j	[–]	Unit normal vector
p'	[Pa]	Acoustic pressure
P_{ij}	[Pa]	Compressive stress tensor
p_{ref}	[Pa]	Reference pressure
Psd	[Pa^2]	Power spectral density
R	[m]	Distance between observer and source

t	[s]	Observer time
T_{ij}	[Pa]	Lightill stress tensor
u_i	[m/s]	Fluid velocity in the xi direction
u_n	[m/s]	Fluid velocity in the normal direction
v_i	[m/s]	Surface velocity in the x_i direction
v_n	[m/s]	Surface velocity in the normal direction
x	[m]	Observer position
$\delta(f)$	[-]	Dirac delta function
Δt	[s]	Time step
ρ	[kg/m ³]	Density
τ	[s]	Source time

Subscripts

L	Loading noise component
T	Thickness noise component
0	Denotes fluid variable in quiescent medium

1. Introduction

Squirrel-cage centrifugal fans are widely used in industry. They are used as circulating fans in central heating and air-conditioning systems in buildings, as blowers in automotive heating/cooling units, and in numerous other applications for their large capacity of mass flow, size compactness and low noise.

Many authors have worked in the study of unsteady phenomena in turbomachines. These phenomena are the interactions and unsteadiness induced by the motion of the rotor relatively to the stator.

Concerning centrifugal fans, M. Gabi and T. Klemm [1] used numerical method based on a CFD analysis, and experimental method using Particle Image Velocimetry (PIV) in order to predict the performance characteristics and flow data of cross-flow fans. Sandra Velarde-Suarez [2] studied the aeroacoustic behaviour based on the theory of vortex sound coupled with experimental data. Siddharth Thakur [3] used three dimensional (3D) CFD approach to analyze fluid flow in a centrifugal fan. Yong Cho and Young J.Moon [4] used the unsteady viscous flow fields of a cross-flow fan computed by solving the two dimensional (2D) incompressible Navier-stokes equations in order to feed the FW-H equation. They studied the acoustic benefit of an impeller with uneven blade spacing. Kwang-Yong Kim [5] applied the response surface method using RANS approach to the aerodynamic design of a forward-curved-blade centrifugal fan to optimize the shapes of scroll and blades in order to maximize the flow efficiency.

In this paper, interactions and unsteadiness induced by the motion of rotating blades relatively to the volute have been studied using CFD calculations. The overall behaviour of the fan has been validated experimentally at different flow rates. The unsteady part of this study is illustrated by the pressure and aerodynamic force fluctuations applied on blade surfaces, and on different points from the lateral surface

of the volute. The analysis of the wake generated by the rotation of the blower shows that the volute tongue is the main zone of unsteadiness and flow perturbations.

Finally, based on pressure fluctuations data acquired upon the surfaces of rotating blades, acoustic pressures have been computed at the far field using the FW-H formalism.

2. Fan presentation

The main fan parameters are presented in Table1. These parameters have been transformed into complete Computer Aided Design (CAD) model and saved into STL format in order to build prototype using rapid prototyping method which requires that parts are complete and have continuity.

Table 2. Geometrical characteristics values

<i>Impeller</i>	
<i>Description</i>	<i>Value</i>
Blade number	39
Impeller width	70 mm
Blade chord length	26.2 mm
Blade thickness	1 mm
Inlet blade angle	5°
Outlet blade angle	70°
Shape blade	<i>circular arc</i>
Rotational speed	3000 rpm
Impeller inlet diameter	120 mm
Impeller outlet diameter	160 mm
<i>Volute casing</i>	
<i>Description</i>	<i>Value</i>
Inlet diameter	120 mm
Outlet size	100 x 76 mm
Volute tongue radius	5 mm
Volute tongue position	<i>Radius 90 mm</i>
Volute shape	<i>Logarithmic law</i>

3. Numerical simulation

The numerical simulations have been carried out using the commercial code FLUENT 6.2. The used flow solver in this code employs for unsteady turbulent flow the three dimensional time-averaged Navier-Stokes equations.

The geometrical parameters given in Table1 have been used in order to generate the computational domain which has been divided into two zones, a rotational zone including the impeller and stationary zones elsewhere. This configuration takes into

account the clearance between the impeller and the volute. Therefore, the inlet and the outlet surfaces of the fan have been extended in order to ensure numerical stability and to minimize boundary conditions effects. The obtained computational domain is shown in Figure 1.

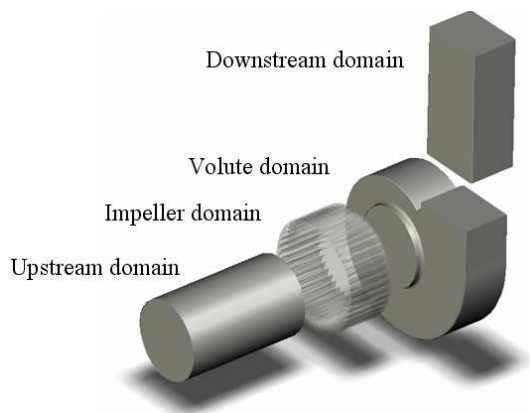


Figure 1. Computational domains

The resulting geometry has been used to build a unstructured grid mesh whose the refinement has been studied and adapted to the flow morphology, minimizing element distortion and having required resolution in high gradient regions. These regions concern essentially the volute tongue zone and the axial gap between the impeller and the volute casing where the flow could present recirculation and perturbations. Using this generation mesh technique, the difference of static pressure between the inlet and the outlet of the fan has been computed with steady state calculations applied on each generated grid. The result of this analysis is shown in Figure 2. According to this figure, the 1.7×10^6 cell grid presents a good compromise between mesh independence and Computing Processing Unit (CPU) time. Figure 3 shows the resulting mesh and the details of the retained grid are given by the Table 2.

Table 3. Retained grid characteristics

Fluid domain	Surface mesh	Solid mesh	Mean size	Number of cells
Impeller	Tri.	hybrid	2 (surf), 3 (solid)	999744
Volute casing	Tri.	hybrid	2 (surf), 5 (solid)	503120
Upstream extent	-	hex	5	60600
Downstream extent	Tri.	hybrid	5	160240
Total				1723704

Concerning the numerical simulation parameters, the CFD simulation process began with a steady flow calculation with a multiple frame of reference based on the

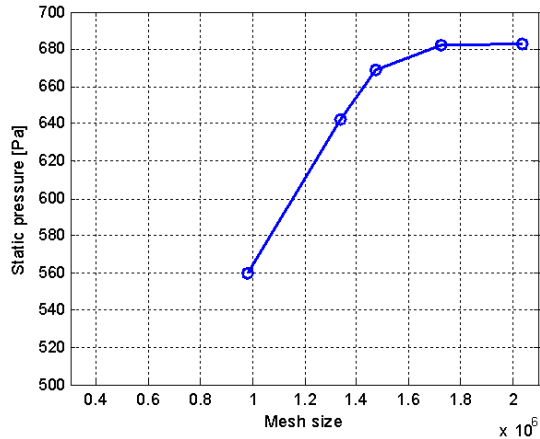


Figure 2. Influence of the grid size on the solution

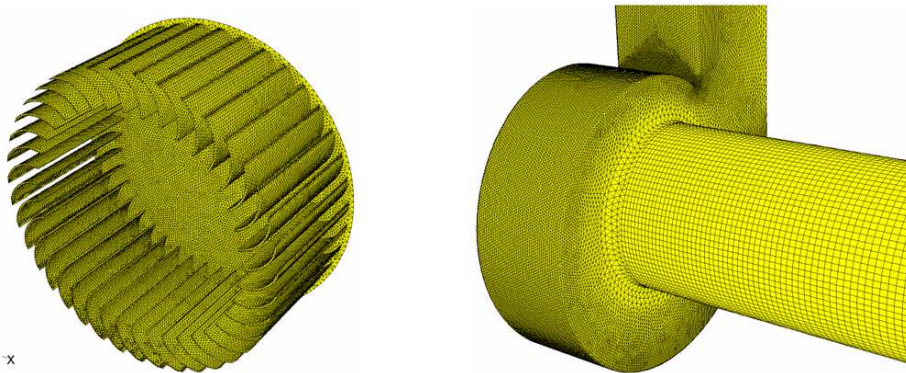


Figure 3. Grids of the computational domain

frozen-rotor approach. In this case, the relative position of the impeller and casing does not change during the calculations. For unsteady calculations, the sliding mesh technique has been applied on the interfaces in order to allow the unsteady interactions between the impeller and the volute. For each time step, the grids change their relative position during the calculations according to the angular velocity of the impeller. Velocity Inlet and Pressure Outlet boundary conditions have been applied at the inlet and the outlet respectively. Turbulence has been modeled with the $k - \omega - Shear Stress$ (SST) model. The $k - \omega - Shear Stress$ model combines the standard $k - \omega$ model with the Standard $k - \varepsilon$ and also takes the transport effects of the principal turbulent shear stress into account through a modified turbulent viscosity formulation. The stopping criterion for the scaled norm of the residuals is set to 10^{-4} . The governing equations have been solved using the segregated solver and a

centred SIMPLE algorithm has been used for the pressure velocity coupling. A gauge pressure of 101325 *Pascal* has been applied at the outlet and a suitable value has been determined for the inlet.

The time step of the unsteady calculations has been set to $5 \cdot 10^{-5}$ seconds; this time step is related to the rotational speed of the impeller and it is small enough to capture the phenomena due to the blades passage and their interactions with the volute casing wall. It corresponds to 1/400 of blade passing period.

4. Overall performances validation

Overall measurements have been carried out on the test bench shown in Figure 4, designed and built at LEMFI-ENSAM according to the ISO 5801 standard [6]. It's composed of an airtight box (1.3x1.3x1.8 m), which is placed upstream the centrifugal fan, making possible to vary the flow rate by changing the diameter of an orifice plate (diaphragm). The rotational speed is set by a frequency variator and measured using an optical tachometer of 0.1 % accuracy. For each diaphragm of given diameter, the static pressure provided by the centrifugal fan is measured using a micro manometer (precision 1 %).

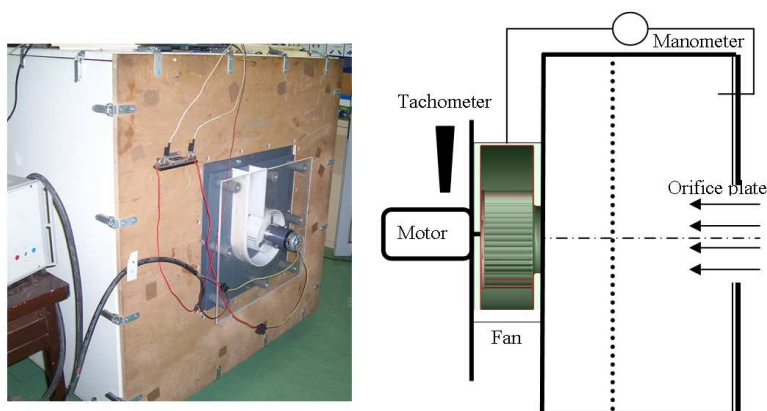


Figure 4. Test bench ISO 5801

Numerical simulations have been carried out at different flow rates. Figure 5 shows the fan static pressure against flow rate and its comparison with the experimental data. It can be seen that the measured static pressure difference between the inlet and the outlet fan is in good agreement with CFD calculations. At partial flow rate, the 3D computation and experimental results don't match; this phenomenon is due to the presence of strong flow recirculation which has not been adequately predicted by the numerical modeling.

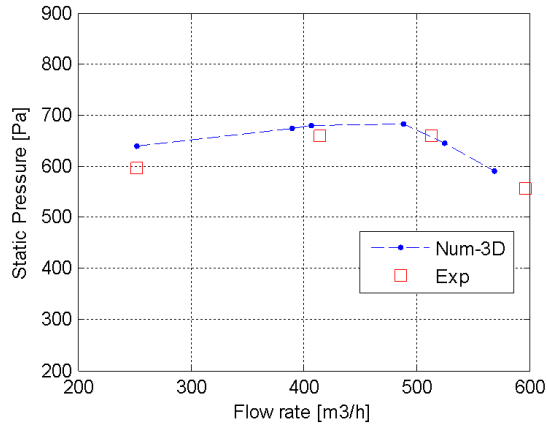


Figure 5. Aerodynamic performances of the centrifugal fan

5. Pressure and velocity fields

Figure 6 shows the instantaneous static pressure field at the median surface of the fan at the nominal flow rate ($500 \text{ m}^3/\text{h}$). The conversion of dynamic pressure produced by the impeller rotation into static pressure by the volute casing can be seen, thus the maximum of pressure is obtained in the outlet duct. A non homogenous pressure distribution is observed at the zone around the gap between volute tongue and impeller periphery, characterized by a high gradient of pressure. The volute tongue whose role is to drive the flow towards the fan outlet also presents a singularity for the flow. The shape of the volute casing creates a geometrical asymmetry, this phenomenon influences the pressure distribution and fluctuating efforts on the blades impeller. The absolute velocity vectors in the fan are plotted in Figure 7 at the median surface of the fan. The volute tongue zone presents a strong recirculation of the fluid particles in the gap between the volute tongue and the impeller periphery.

In the meridian surface, it can be seen that the impeller blades are partially fed by the flow. This non homogenous distribution of the mass flow coupled with the rectangular shape of the volute casing creates strong vortex and recirculation of the fluid at the axial gap, this phenomenon generates aerodynamic losses.

6. Unsteady calculations and results

The different position around the volute in the middle span (Span 2), where fluctuating static pressure have been calculated (Points 1 to 9) are shown in Figure 6. The same distribution of points has been used in two other parallel spans, Span1 near the inlet of the fan, and Span 3 in the bottom of the volute. For each time step, the data have been saved. After windowing the temporal signals using Hamming's window function, each recorded sample has been Fast Fourier Transform (FFT) processed (reference pressure is set to $2 \times 10^{-5} \text{ Pa}$). The aerodynamic pressure spectra

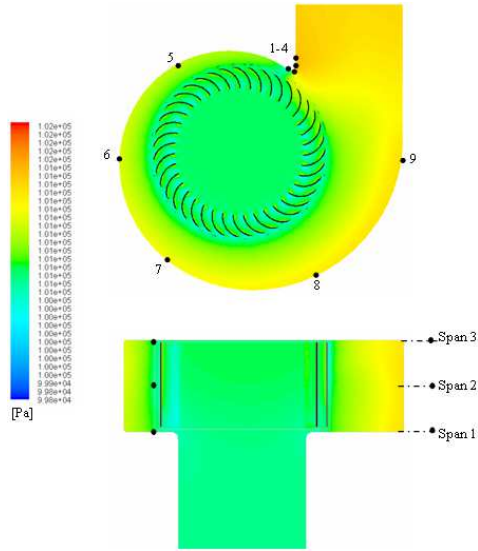


Figure 6. Static pressure field: middle surface and meridian surface of the fan

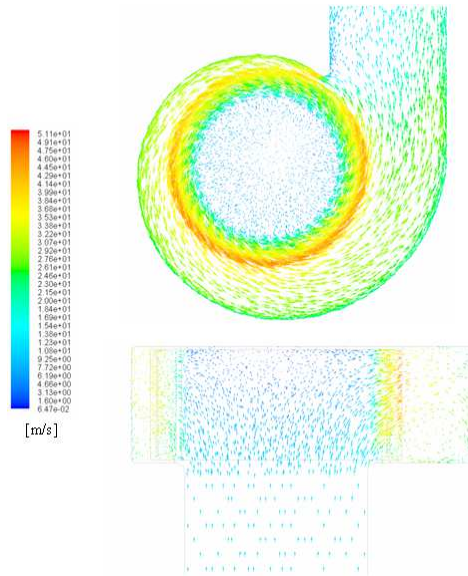


Figure 7. Absolute velocity field: middle surface and meridian surface of the fan

have been finally obtained. These spectra provide a direct measure of the amplitude of the aerodynamic pressure fluctuations at each frequency.

Figure 8 shows the spectrum of the aerodynamic pressure calculated at the volute tongue in Span 2. The graph suggests that the dominant mode occurs at 1950 Hz, which corresponds to the blade passing frequency (BPF). A non presence of other peaks in the spectrum at the harmonics frequency is observed. This is due to the nature of the interaction between the impeller and the volute, which does not generate interferences.

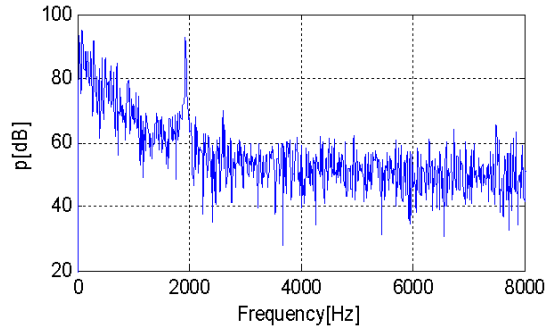


Figure 8. Aerodynamic pressure spectrum at the volute tongue

The Fourier coefficient values at the BPF point, at each computation point, and at the three defined spans are have been calculated and reported in the graph shown in Figure 9. The graph represents the magnitude of the wake generated by the blades motion around the volute. The shape of the three curves globally matches. The

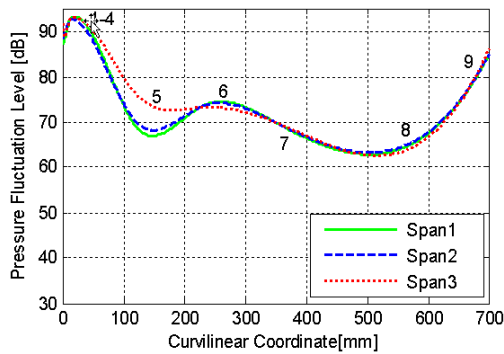


Figure 9. Pressure fluctuation level around the volute at the BPF (1950 Hz)

dominant value is observed at the volute tongue point; this result indicates that the volute tongue is the main zone of unsteadiness and interaction with the rotating

impeller. Away from the volute tongue the three curves decrease, thus the minimum value is observed at the zone around the point 7, this is due to the morphology of the flow which becomes stable. The curves increase progressively from the point 7 on. It can be seen that the point 6 is remarkable because of the curve increases, this is due to the flow which becomes disorganized and it can be related to the volute tongue effect.

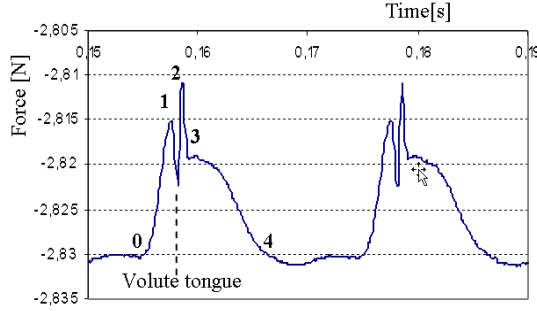


Figure 10. Force fluctuations applied on the blade (2 revolutions)

Figure 10 shows two periods of the force fluctuations applied on one blade. The total force component on the blade has been computed from the node value by summing the pressure and viscous forces of each cell. According to this diagram, the influence of the volute tongue on the force variation can be seen between Point 1 and Point 3. A quick fluctuation at Point 2 (two milliseconds between Points 1 and 3) is observed. This fast variation has a significant impact on the loading noise generation defined in section 8.

7. Aeroacoustic modeling and results

The FW-H [7] equation is essentially an inhomogeneous wave equation that can be derived manipulating the continuity equation and the Navier-Stokes equations. The FW-H equation can be written as:

$$\frac{1}{a_0^2} \frac{\partial^2 p'}{\partial t^2} - \nabla^2 p' = \frac{\partial \{[\rho_0 v_n + \rho(u_n - v_n)]\delta(f)\}}{\partial t} - \frac{\partial \{[P_{ij} n_j + \rho u_i (u_n - v_n)]\delta(f)\}}{\partial x_i} + \frac{\partial^2}{\partial x_i \partial x_j} [T_{ij} H(f)], \quad (7.1)$$

where:

$$T_{ij} = \rho u_i u_j + P_{ij} - a_0^2 (\rho - \rho_0) \delta_{ij} \quad (7.2)$$

$$P_{ij} = p \delta_{ij} - \mu \left[\frac{\partial u_i}{\partial x_j} + \frac{\partial u_j}{\partial x_i} + \frac{2\partial u_k}{3\partial x_k} \delta_{ij} \right] \quad (7.3)$$

The first two source terms in equation (7.1) are monopole (thickness) and dipole (loading) sources, respectively, based on their mathematical structure. The monopole

source term models the noise generated by the displacement of fluid as the body passes. The dipole or loading source term models the noise that results from the unsteady motion of the force distribution on the body surface. Both of these sources are surface sources: i.e., they act only on the surface $f = 0$ as indicated by the Dirac delta function $\delta(f)$. The third source term is a quadrupole source term that acts throughout the volume that is exterior to the data surface as indicated by the Heaviside $H(f)$.

Using the free-space Green function $(\delta(G)/4\pi r)$, the solution to equation (7.1) is obtained. Thus the complete solution consists of surface integrals and volume integrals. The surface integrals represent the contribution from monopole and dipole acoustic sources and partially from quadrupole sources if the integration surface is impermeable. The contribution of the volume integrals which represent quadrupole (volume) sources in the region outside the source surface becomes small when flow is subsonic. Thus the volume integrals are neglected.

Finally:

$$p'(\mathbf{x}, t) = p'_T(\mathbf{x}, t) + p'_L(\mathbf{x}, t) \tag{7.4}$$

The two terms on the right in equation (7.4), and , thickness and loading terms respectively are developed in [8].

The fluctuating variables, pressure and velocity upon the impeller surfaces, have been obtained for 2000 time steps. Then, sound pressure signals have been computed at the receiver location using the source data collected during the aerodynamic calculation. For the time step selected here ($5 \times 10^{-5} s$), the highest frequency that the acoustic analysis can produce is:

$$F = \frac{1}{2\Delta t} 10 \text{ kHz}.$$

Figure 11 shows the sound pressure level spectrum of the impeller computed one meter away from the axis of the fan at the exit duct. This position is selected in order to compute the sound pressure level according to the free field radiation condition.

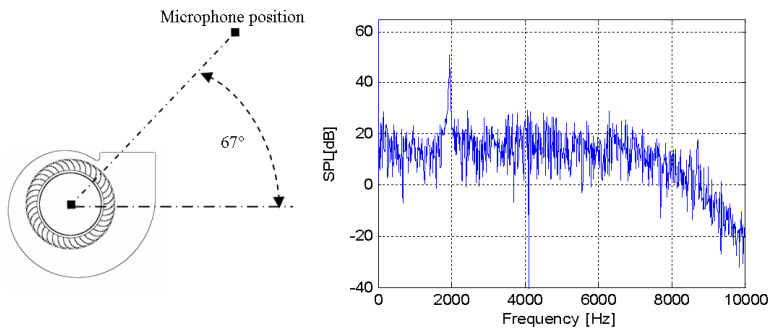


Figure 11. Microphone position and corresponding spectrum radiated by the impeller

It can be seen that there is one dominant peak, this peak occurs at 1950 Hz , which corresponds to the blade passing frequency. Amplitude of 51 dB at this frequency is noticed. The non presence of other harmonics is due to the geometry shape of the volute casing interacting with the rotating blades. Thus, the significant unsteadiness detected by the used calculation models is due only to the presence of the volute tongue in the flow. According to [8], URANS calculations cannot adequately provide the surface pressure fluctuations needed for broadband noise prediction. Thus, the spectrum component, other than the fundamental harmonic peak could be numerical.

8. Conclusion

3D unsteady flow in a centrifugal fan has been studied in this paper using URANS equations. The overall behaviour of the fan has been validated experimentally at different flow rate.

The analysis of the flow morphology showed the influence of the geometry design on the aerodynamic performances of the fan.

The analysis of the pressure fluctuations around the lateral surface of the volute, and the force fluctuations indicated that the main source of perturbation and unsteadiness in squirrel cage fan is the volute tongue zone.

The spectral analysis of the sound pressure level computed by the FW-H equation showed that the main source of tonal noise in the investigated fan is the aerodynamic interactions between the impeller and the volute tongue.

It should be interesting to extend this work by:

- Validating the fluctuating pressures computed on the lateral surface of the volute casing.
- Validating the acoustic spectra using measurements in anechoic room.
- Using Large Eddy Simulation (LES) approach to feed acoustic models.

References

1. GABI, M. AND KLEMM, T.: Numerical and experimental investigations of cross-flow fans, *Journal of Computational and Applied Mechanics*, **5**, (2004), 251-261.
2. SANDRA, V.S. AND SANTOLARYA, C.: Experimental study on the aeroacoustic behaviour of a forward-curved blades centrifugal fan. *ASME Journal of Fluid Engineering*, **277**, (1999), 276-281.
3. THAKUR, S., LIN, W. AND WRIGHT, J.: Prediction of flow in centrifugal blower using quasi-steady rotor-stator models. *Journal of Engineering Mechanics*, (2002), 1039-1049.
4. CHO, Y. AND MOON, Y.J.: Discrete Noise Prediction of variable pitch cross-flow fans by unsteady Navier-Stokes computations. *ASME Journal of Fluids Engineering*, **125**, (2003), 543-550.
5. KIM, K.Y. AND SEO, S.J.: Shape Optimization of forward-curved-blade centrifugal fan with Navier-Stokes analysis. *ASME Journal of Fluids Engineering*, **126**, (2004), 735-742.
6. ISO 5801.: Industrial fans - Performance testing using standardized airways, (1997).

7. WILLIAMS, F. AND HAWKINGS, J.E.: Sound generation by turbulence and surfaces in arbitrary motion. *Phi. Trans. Roy. Soc.*, A264, (1969).
8. BRENTNER, K.S., AND FARASSAT, F.: An analytical comparison of the acoustic analogy and Kirchhoff formulation for moving surfaces. *AIAA Journal*, **36**(8), (1998).

Notes for Contributors

to the Journal of Computational and Applied Mechanics

Aims and scope. The aim of the journal is to publish research papers on theoretical and applied mechanics. Special emphasis is given to articles on computational mechanics, continuum mechanics (mechanics of solid bodies, fluid mechanics, heat and mass transfer) and dynamics. Review papers on a research field and materials effective for teaching can also be accepted and are published as review papers or classroom notes. Papers devoted to mathematical problems relevant to mechanics will also be considered.

Frequency of the journal. Two issues a year (approximately 80 pages per issue).

Submission of Manuscripts. Submission of a manuscript implies that the paper has not been published, nor is being considered for publication elsewhere. Papers should be written in standard grammatical English. Two copies of the manuscript should be submitted on pages of A4 size. The text is to be 130 mm wide and 190 mm long and the main text should be typeset in 10pt CMR fonts. Though the length of a paper is not prescribed, authors are encouraged to write concisely. However, short communications or discussions on papers published in the journal must not be longer than 2 pages. Each manuscript should be provided with an English Abstract of about 50–70 words, reporting concisely on the objective and results of the paper. The Abstract is followed by the Mathematical Subject Classification – in case the author (or authors) give the classification codes – then the keywords (no more than five). References should be grouped at the end of the paper in numerical order of appearance. Author's name(s) and initials, paper titles, journal name, volume, issue, year and page numbers should be given for all journals referenced.

The journal prefers the submission of manuscripts in \LaTeX . Authors should prefer the $\mathcal{AMS}\text{-}\text{\LaTeX}$ article class and are not recommended to define their own \LaTeX commands. Visit our home page for further details concerning the issue how to edit your paper.

For the purpose of refereeing, two copies of the manuscripts should initially be submitted in hardcopy to an editor of the journal. The eventual supply of an accepted-for-publication paper in its final camera-ready form (together with the corresponding files on an MS-DOS diskette) will ensure more rapid publication. Format requirements are provided by the home page of the journal from which sample \LaTeX files can be downloaded:

<http://www.uni-miskolc.hu/home/web/pumns/mechanics>

These sample files can also be obtained directly (via e-mail) from a member of the Editorial Board, Gy. Szeidl (Gyorgy.SZEIDL@uni-miskolc.hu), upon request.

Twenty offprints of each paper will be provided free of charge and mailed to the correspondent author.

The Journal of Computational and Applied Mechanics is abstracted in Zentralblatt für Mathematik and in the Russian Referativnij Zhurnal.

Responsible for publication: Rector of the Miskolc University

Published by the Miskolc University Press under the leadership of Dr. József PÉTER

Responsible for duplication: works manager Mária KOVÁCS

Number of copies printed: 200

Put to the Press on April 12, 2008

Number of permission: TU 2008-???-ME

HU ISSN 1586–2070

A Short History of the Publications of the University of Miskolc

The University of Miskolc (Hungary) is an important center of research in Central Europe. Its parent university was founded by the Empress Maria Teresia in Selmecebánya (today Banská Štiavnica, Slovakia) in 1735. After the first World War the legal predecessor of the University of Miskolc moved to Sopron (Hungary) where, in 1929, it started the series of university publications with the title *Publications of the Mining and Metallurgical Division of the Hungarian Academy of Mining and Forestry Engineering* (Volumes I.-VI.). From 1934 to 1947 the Institution had the name Faculty of Mining, Metallurgical and Forestry Engineering of the József Nádor University of Technology and Economic Sciences at Sopron. Accordingly, the publications were given the title *Publications of the Mining and Metallurgical Engineering Division* (Volumes VII.-XVI.). For the last volume before 1950 – due to a further change in the name of the Institution – *Technical University, Faculties of Mining, Metallurgical and Forestry Engineering, Publications of the Mining and Metallurgical Divisions* was the title.

For some years after 1950 the Publications were temporarily suspended.

After the foundation of the Mechanical Engineering Faculty in Miskolc in 1949 and the movement of the Sopron Mining and Metallurgical Faculties to Miskolc, the Publications restarted with the general title *Publications of the Technical University of Heavy Industry* in 1955. Four new series - Series A (Mining), Series B (Metallurgy), Series C (Machinery) and Series D (Natural Sciences) - were founded in 1976. These came out both in foreign languages (English, German and Russian) and in Hungarian.

In 1990, right after the foundation of some new faculties, the university was renamed to University of Miskolc. At the same time the structure of the Publications was reorganized so that it could follow the faculty structure. Accordingly three new series were established: Series E (Legal Sciences), Series F (Economic Sciences) and Series G (Humanities and Social Sciences). The latest series, i.e., the series H (European Integration Studies) was founded in 2001. The eight series are formed by some periodicals and such publications which come out with various frequencies.

Papers on computational and applied mechanics were published in the

Publications of the University of Miskolc, Series D, Natural Sciences.

This series was given the name Natural Sciences, Mathematics in 1995. The name change reflects the fact that most of the papers published in the journal are of mathematical nature though papers on mechanics also come out.

The series

Publications of the University of Miskolc, Series C, Fundamental Engineering Sciences

founded in 1995 also published papers on mechanical issues. The present journal, which is published with the support of the Faculty of Mechanical Engineering as a member of the Series C (Machinery), is the legal successor of the above journal.



Contents
Contributed Papers

- Toni KLEMM, Martin GABI, Jean-Nicolas HERAUD: Application of a cross flow fan as wind turbine 123–133
- Mizuyasu KOIDE, Naoto KATO, Shuichi YAMADA, Yusuke KAWABATA, Tsutomu TAKAHASHI, Masataka SHIRAKASHI: Influence of a cruciform arrangement downstream strip-plate on crossflow vibration of a square cylinder 135–148
- R. Ivan LEWIS: Vortex cloud flow modeling of cylinders in orbital motion at low Reynolds numbers and comparisons with some published grid-based CFD predictions 149–161
- Luca OGGIANO, Lars SAETRAN, Sveinung LOSET and Ronny WINTHER: Reducing the athlete's aerodynamical resistance 163–173
- Petra PUNČOCHÁŘOVÁ, Karel KOZEL, Jaromír HORÁČEK, Jiří FÜRST: An unsteady numerical solution of viscous compressible flows in a channel for low Mach numbers 175–191
- Robert Zoltán SZÁSZ, Christophe DUWIG and László FUCHS: Computations of the acoustic field in an annular gas turbine combustion chamber 193–210
- Mohand YOUNSI, Farid BAKIR, Smaine KOUIDRI and Robert REY: 3D unsteady flow in a centrifugal fan: impeller - volute interaction 211–223